University of South Carolina

Scholar Commons

2016

Mathematical Modeling Of Transport And Corrosion Phenomenon Inside High Temperature Molten Salt Systems

Bahareh Alsadat Tavakoli Mehrabadi
University of South Carolina

Follow this and additional works at: https://scholarcommons.sc.edu/etd

Part of the Chemical Engineering Commons

Recommended Citation

MATHEMATICAL MODELING OF TRANSPORT AND CORROSION PHENOMENON
INSIDE HIGH TEMPERATURE MOLTEN SALT SYSTEMS

by

Bahareh Alsadat Tavakoli Mehrabadi

Bachelor of Engineering
Sharif University of Technology, 2007

Master of Engineering
Sharif University of Technology, 2010

_____

Submitted in Partial Fulfillment of the Requirements

For the Degree of Doctor of Philosophy in

Chemical Engineering

College of Engineering and Computing

University of South Carolina

2016

Accepted by:

John W. Weidner, Major Professor

John Regalbuto, Committee Member

Sirivatch Shimpalee, Committee Member

John Monnier, Committee Member

Brenda Garcia-Diaz, Committee Member

Xinyu Huang, Committee Member

Cheryl L. Addy, Vice Provost and Dean of the Graduate School

DEDICATION

I dedicate this thesis to my beloved parents for their supports, guidance and love.

ACKNOWLEDGEMENTS

Firstly, I would like to express my sincere gratitude to my advisor Dr. John W. Weidner for the continuous support of my Ph.D. study and related research, for his patience, motivation, and immense knowledge. His guidance helped me in all the time of research and writing of this dissertation. I cannot imagine having a better advisor and mentor for my Ph.D. study. I especially enjoyed his style of mentoring students from which I have benefited tremendously in my personal and professional growth. My sincere thanks also goes to Dr. Sirivatch Shimpalee, who provided me an opportunity to learn simulation, and modeling. Without his precious support it would not be possible to conduct this research. I also want to thank the members of the Savannah River National Laboratory (SRNL), Particularly Dr. Luke Olson, Dr. Michael Martinez-Rodriguez and Dr. Brenda Garcia-Diaz, who is also a member of my dissertation committee, for their helpful advice and for providing the experimental results for this work. I am very grateful to the other members of my dissertation committee: Dr. John Monnier, Dr. John Regalbuto, and Dr. Xinyu Huang, for their insightful comments and encouragement to widen my research from various perspectives. I would also like to thank my friends and my colleagues, particularly, Taylor Garrick and Cody Wilkins at the University of South Carolina for their help and moral support that made my stay and studies at USC more enjoyable.

Finally, my deepest gratitude goes to my family: my parents, my sister and my brother for supporting me spiritually throughout writing this thesis and my life in general.

ABSTRACT

In today's world, alternative clean methods of energy are needed to meet growing energy demands. Concentrating solar thermal power, more commonly referred to as CSP, is unique among renewable energy generators because even though it is variable, like solar photovoltaic and wind, it can easily be coupled with thermal energy storage as well as conventional fuels, making it highly dispatchable. One challenge with concentrated solar power (CSP) systems is the potential corrosion of the alloys in the receivers and heat exchangers at high-temperature (700-1000 °C), which leads to a reduction of heat transfer efficiency and influences the systems durability. The objective of this dissertation is to create a comprehensive mathematical model including thermal gradients and fluid flow to predict corrosion rates and mechanisms observed in state of the art molten salt heat transfer systems.

The corrosion model was designed and benchmarked against a thermosiphon reactor. This thermosiphon reactor exposed the alloy coupons to non-isothermal conditions expected in CSP plants. Cathodic protection was also added to the model as a mitigation strategy for corrosion of metal surfaces. The model compared the corrosion rates for the cases with and without cathodic protection under different operational conditions for different high-temperature alloys (e.g., Haynes 230, Haynes NS-163, and Incoloy 800H). The model is capable of considering the effects of kinetic and mass transfer on the corrosion rate under high temperature fluid flow systems.

The results reveal that temperature has an important effect on the corrosion rate of high-temperature alloys in molten salt systems. For the case with the higher temperature range 800-950 ℃, the corrosion rate is almost twice that of the case with the low temperature range 650-800 ℃. Another important factor is dissolved metal ions (e.g., Cr^{3+}) that diffuse to the surface of the alloy as a result of disproportionation reaction at the more electropositive metals and cause the oxidation\reduction reactions on the surface of the alloy.

TABLE OF CONTENTS

LIST OF TABLES

LIST OF FIGURES

xiii

LIST OF SYMBOLS

a : Active surface area of catalyst per volume (cm^{-1})

a_0: Active surface area of catalyst per volume before contamination (cm^{-1})

C_{O_2}: Concentration of oxygenin the catalyst layer (mol cm^{-3})

C_{H^+}: Concentration of proton in the catalyst layer (mol cm^{-3})

$C_{H^+,0}$: Initial concentration of proton for baseline (mol cm^{-3})

C_i : Concentration of species i in the bulk, (mol m^{-3})

C_i^* : Concentration of species i at the surface, (mol m^{-3})

C_i^{ref} : Reference concentration of species i, 1.0 mol m^{-3}.

D^{eff}: Effective diffusion coefficients of reactant salts in grain boundary pores

(m^2 s^{-1}

D_i : Diffusion coefficients of reactant i, in the bulk salts (m^2 s^{-1})

E : Temperature and concentration corrected standard potentials (V)

E^0 : Temperature corrected standard potential (V)

E_{eq}: Open circuit potential (V)

E_m: IR$_m$ corrected voltage (V)

F : Faraday constant, (96,485 C mol^{-1})

i : Current density, (A m^{-2})

i_0 : Exchange current density, (A m^{-2})

i_{corr} : Corrosion current density, (A m^{-2})

i_{avg} : Average corrosion current density at the surface of the coupon, (A m^{-2})

I : Current density (A cm^{-2})

N_i : Flux of a solute species i, (mol m^{-2} s^{-1})

n : Number of electrons transferred in electrode reaction

R_0: Ionomer resistance before contamination (ohm)

R_i : Ionomer specific resistance (ohm cm^2)

R_m: Membrane specific resistance (ohm cm^2)

R : Gas constant, (8.314 J mol^{-1} K^{-1})

t: Time (h)

T: Temperature, (K)

x : x-position, (m)

Y : Mass fraction

Greek

$\alpha_{a,c}$ = transfer coeffcients

$\frac{1}{\beta}$: Tafel slpoe

γ_{cc}: Rate of catalyst poisoning (h^{-1})

γ_{cr}: Rate of catalyst recovery (h^{-1})

γ_{ic}: Rate of ionomer poisoning (h^{-1})

γ_{ir}: Rate of ionomer recovery (h^{-1})

δ : Porous layer thickness, (m)

η : Metal surface overpotential, (V)

η_a : Activation overpotentials of anode (V)

η_c : Activation overpotentials of cathode (V)

κ : Thermal conductivity, (W K^{-1}m^{-1})

μ : Dynamic viscosity, (kg m^{-1}s^{-1})

ρ : Density, (g m^{-3})

θ: Number of active platinum sites loss

θ_1: Fractional loss of catalyst sites after steady state contamination (i. e. , t → ∞)

θ_2: Fractional loss of catalyst sites after steady state recovery (i. e. , t → ∞)

σ: Effective inomer conductivity (ohm^{-1}cm^{-1})

σ_0: Inomer conductivity before contamination (ohm^{-1}cm^{-1})

σ_m: Membrane conductivity (ohm^{-1}cm^{-1}),

φ : TOC per amount of Pt at the catalyst layer (ppm mg$_{Pt}^{-1}$)

τ : Porous layer tortuosity

ε : Porous layer porosity

LIST OF ABBREVIATIONS

ANL .... Argonne National Laboratory

BOP .... Balance of Plant

BzOH .... Benzyl Alcohol

CAE .... Computer-Aided Engineering

CP .... Cathodic Protection

Cr .... Chromium

CSP .... Concentration Solar Power

DGMEA .... Diethylene Glycol Monoethyl Ether

DGMEE .... Diethylene Glycol Monoethyl Ether Acetate

DOE .... Department of Energy

2,6-DAT .... 2,6 Diaminotoluene

EDS .... Energy Dispersive Spectroscopy

FV .... Finite Volume

H_2 .... Hydrogen

HTF .... Heat Transfer Fluid

CHAPTER 1. INTRODUCTION

1.1 Clean Energy Technologies

The increasing the demand for energy, energy security and the need to minimize the impact on the environment related to energy production are all major incentives for the research and development of alternative energy technologies. There are several clean energy sources that can alleviate fossil fuel shortages and environmental pollutant. Examples of clean energy technologies that, one can refer to are concentrating solar power (CSP) plants, and polymer electrolyte membrane fuel cells (PEMFCs).

For electricity generation on a large commercial scale, CSP has the potential to be a highly economical conversion process. The conversion of sunlight to electricity, is one of the leading candidates among clean energy technologies. Solar energy has enormous advantages over other sources of energy because it is free, abundant, inexhaustible and clean. Another important alternative source of clean energy is the use of hydrogen in PEMFC fuel cells for both transportation and stationary applications. The extraordinary environmental quality and high efficiency of PEMFCs make them a potential alternative energy source.

Despite fundamental innovations that have advanced commercialization of these two technologies, , many technical hurdles still need to be overcome to lower cost and achieve wide commercial adoption.

Many clean energy programs have integrated a strong focus on electrochemistry due to the high efficiencies that can be achieved by electrochemical reactions. The high efficiencies of electrochemical processes are due to the direct relationship between electrochemical energy and Gibbs energy from fundamental thermodynamics. Mechanical systems used in energy applications such as turbines are limited by Carnot efficiency, where electrochemical systems are only limited by the kinetics of the electrochemical reaction and ohmic losses in the electrolyte. Corrosion mechanisms are also an electrochemical phenomena that are important to understand and mitigate to prolong the lifetime for clean energy systems. All of these aspects make electrochemical engineering vital to further development of clean energy technologies [1].

In this work electrochemistry is used to improve the lifetime of these two clean energy technologies. In the first part of this dissertation the corrosion problem in the CSP plant are discussed, followed by a mathematical model development that include thermal gradients and fluid flow to predict corrosion rates and mechanisms observed in the state of the art molten salt heat transfer systems of CSP plants. The second part of the study is devoted to identify the performance loss and recovery of a PEM fuel cell due to Balance of Plant (BOP) materials contaminations via a combination of experimental data and mathematical models.

1.2 Concentrated Solar Power (CSP) Systems

Diminishing fossil fuel reserves and increasing effects of anthropogenic climate change due to greenhouse gas emissions have led to an unprecedented global interest in renewable sources of energy [2]. Among different types of renewable power generation, the CSP

system has become one of the emerging technologies in the world. The defining aspect of CSP is that it captures and concentrates solar radiation to provide the heat required to generate electricity, rather than using fossil fuels or nuclear reactions. Another attribute of CSP plants is that they can be equipped with a thermal energy storage system in order to generate electricity even when the sky is cloudy or after sunset.

In general, CSP systems convert solar radiation into thermal energy by focusing the sun's rays onto a central area called a receiver. The heat transfer fluid (HTF) inside the receiver is heated by absorption of the radiation and is pumped through the receiver pipes to deliver the thermal energy to a heat exchanger integrated with a steam turbine to generate power. The processes occurring in CSP systems is illustrated in Figure 1.1. CSP systems are early in their adoption, but have already begun commercialization. Today, there are 80 operational CSP plants around the world, mainly in the United States and Spain, with 1.9 GW of total capacity. Another 23 are under construction in India, China, Australia, and South Africa, among other places [3]. As experience is gained with CSP systems and as R&D advances, plants will get bigger, mass production of components will occur and costs will come down with increased competition between CSP integrators.[4]. The U.S. Department of Energy (DOE) target is to make unsubsidized solar energy cost competitive with other forms of energy on the grid by the end of the decade. Figure 1.2 shows the breakdown of CSP systems cost. It is projected that CSP systems need to be able to produce energy with a cost of $0.06/kWh when they are scaled up and implemented on a large scale. To reach these targets, it is generally believed that temperatures of the HTFs will need to be high enough to drive an advanced Brayton cycle or Rankine cycle with superheated steam. Higher operating temperatures will allow an increase in the electrical efficiency of

3

CSP plants, reduce the cost of the thermal storage system (as a smaller storage volume is needed for a given amount of energy storage) and achieve higher thermal-to-electric efficiencies.

It is projected that average operating temperatures near 750°C with local hot spots up to 850 °C would be needed to make these systems viable and achieve energy price goals. To make this system feasible, HTFs that can operate at these temperatures for long periods of time without significant degradation reaction of either the HFT or the materials of construction for the system are required.
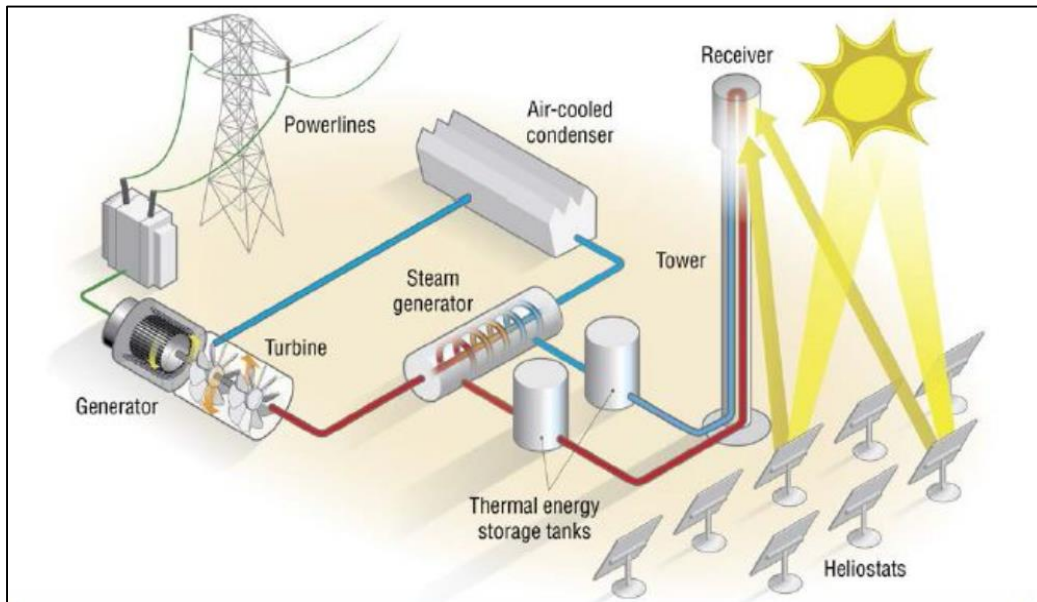
Figure 1.1. Schematic of a CSP plant [5].

A variety of HTFs which may be used in CSP systems have been considered and researched, including six groups: gases (air, helium and super critical CO_2), water/steam, thermal oils, organic fluids, molten salts and liquid metals. Table 1.1 summarizes the respective advantages and drawbacks of the different groups of HTFs that can be employed in CSP systems [6].

4

Table 1.1. Advantages and disadvantages of the different groups of HTFs for CSP systems [6].

	Air, helium and super critical	Water/steam	Thermal oils	Organic fluids	Molten salts	Liquid metals
Thermophysical properties	Low dynamic viscosity and high efficiencies. High operating temperatures (above 700 °C). Impossibility of thermal storage, high pumping power and low thermal conductivity.	Low dynamic viscosity (similar to air), non-expensive Rankine direct cycle. Limited operating temperatures (600 °C), impossibility of thermal storage and high pressure required.	Constant thermal conductivity over a wide range of temperatures and high efficiencies at small scales. Thermal stability only up to 400 °C, low heat capacity, high pumping power	Low viscosity and high heat capacity. Low thermal conductivity and limited temperature range (up to 393 °C).	Good thermal stability up to 600 °C, low viscosity and vapour pressure. Possibility of direct thermal storage. With new mixtures temperatures of 800 e900 °C could be achieved, but with the drawback of a too high melting point (400 °C).	Large temperature range (above 1000 °C for most of the candidates) and thermal stability at high temperatures, high thermal conductivities, heat fluxes and efficiencies. Possibility of thermal storage with some candidates.
Corrosion rate	High oxidation rates at high temperatures, better compatibility with less noble metals.	Corrosion starts at 300 °C and increases at high temperatures.	No information regarding compatibility with materials is available in the literature.	No information regarding compatibility with materials is available in the literature.	Big corrosion issues at temperatures higher than 600 °C. Better compatibility with LiNaK mixtures.	Big corrosion issues at high temperatures for the heavy metals and fusible metals group
Cost and availability	High availability and zero costs.	Low availability in regions characterized by high solar radiation rates.	Relatively high costs (between 3 and 5 USD/Kg).	High costs (100 USD/Kg).	Low costs but problems for meeting the demand of nitrate/nitrite based salts	High costs varying for the different candidates.

Air and water are no longer considered as viable options. Air increases in volume when heated and requires larger heat exchanger sizes for efficient heat transfer, which also greatly increases the capital cost of the heat exchanger [7]. Water also can prove unstable and difficult to manage at high temperature/high pressure situations. Thermal oils have been a preferred heat transfer fluid for CSP developers designing low to intermediate temperature CSP systems to get around the high pressure issue. The problem with thermal oils is that the hydrocarbons break down when heated to 400 °C. and limit the maximum operating temperature for parabolic troughs [8]. Liquid metals have been used as heat transfer fluids in nuclear reactors since the 1940s and are currently being studied for use in solar thermal systems as HTFs and thermal energy storage media. Although liquid metals have not been used in commercial CSP applications until now, they have several promising properties including extensive operating temperature range, low viscosity and efficient heat transfer characteristics. The issue with liquid metal is that the cost is higher than that of molten-salt or water/steam HTFs. Also, heat capacities of liquid metals are low relative to commercial nitrate/nitrite based salts and hence they are less favorable to be used as thermal energy storage media [9].

Molten salts proposed for use with high temperature Brayton and superheated Rankine cycles are usually molten halides due to their good heat transfer properties. They can make excellent heat transfer fluids in high temperature applications (260°C - 1400°C) because of their high melting points, stability at high temperatures, and low viscosities. The size of pipes and other equipment used for molten salts together with the pumping power required is much smaller than if gases were employed in the same high temperature applications.

The wall thicknesses required in using molten salts are also much smaller than those required in high-pressure steam systems operating near the same temperatures [10].
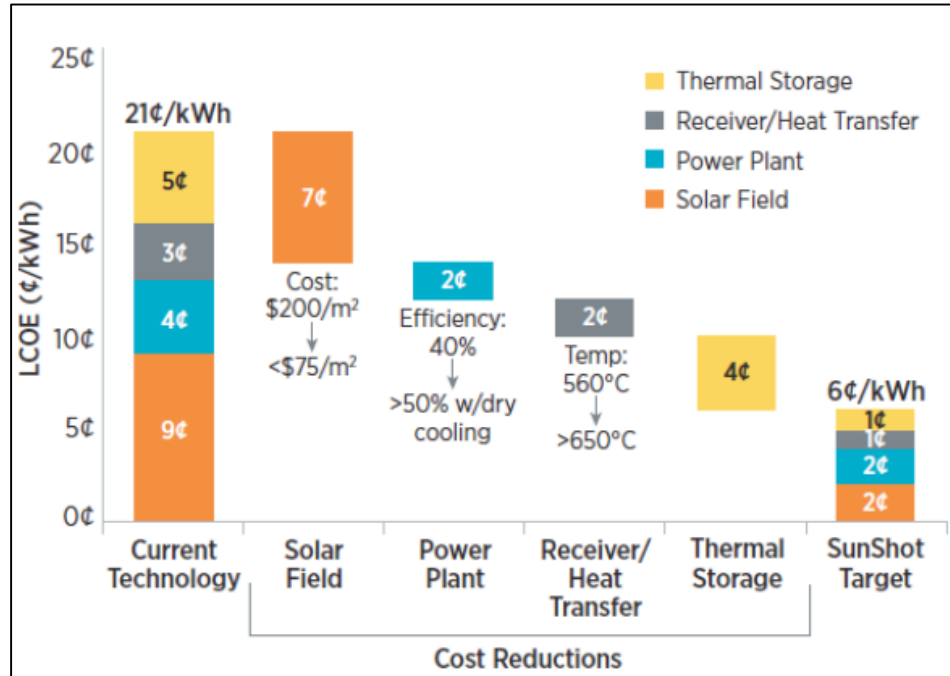
Figure 1.2. The breakdown of CSP systems cost [11].

Certain molten salts can serve as energy storage mediums. Their high melting temperatures and high thermal capacitances make it so they retain heat for periods longer than 24 hours. They also have high energy densities which reduces the amount of molten salt needed in applications normally carried out by traditional working fluids. Their ability to store this heat energy allows electric energy at any time of the day [12].

The main disadvantage to using molten salts is that they can be highly corrosive, especially at high temperatures. Therefore, piping, heat exchangers, pump heads, and other components in CSP systems that come in contact with the molten salt are expected to face more severe degradation [13].

1.3 Polymer Electrolyte Membrane Fuel Cell (PEMFC)

Proton exchange membrane fuel cells (PEMFCs) are considered to be a promising technology for clean and efficient power generation in the twenty-first century. Their high efficiency and zero emission have made them a prime candidate for powering the next generation of electric vehicles [14]. Typical fuel cells operate at a voltage ranging from 0.6 – 0.8 V, and produce a current per active area (current density) of 0.2 to 1.0 A/cm^2. A PEMFC consists of a negatively charged electrode (anode), a positively charged electrode (cathode), and an electrolyte membrane. Hydrogen is oxidized on the anode and oxygen is reduced on the cathode. Protons are transported from the anode to the cathode through the electrolyte membrane, and the electrons are carried to the cathode over the external circuit. The electrons are transported through conductive materials to travel to the load when needed. On the cathode-side, oxygen reacts with protons and electrons forming water and producing heat. Both, the anode and cathode, contain a catalyst to create electricity from the electrochemical process as shown in Figure 1.3.
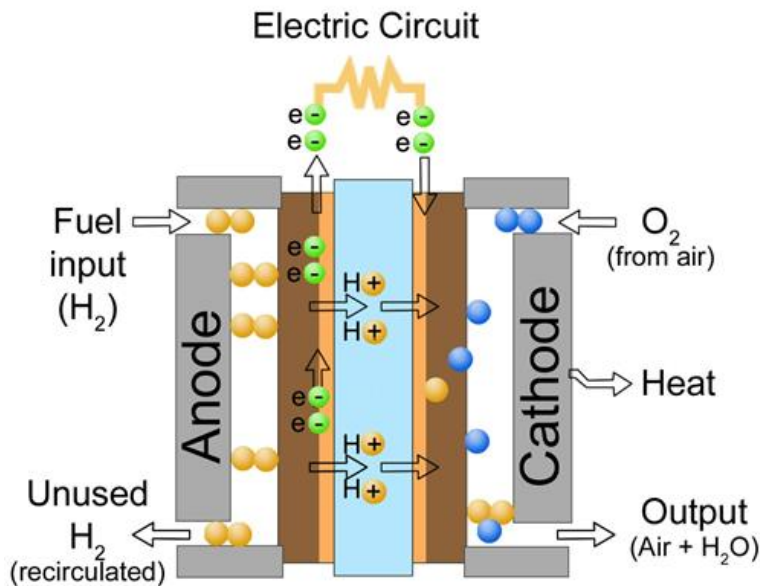
Figure 1.3 Schematic of a single PEM fuel cell [15].

8

The conversion of the chemical energy of the reactants to electrical energy, heat and liquid water occurs in the catalyst layers, which have a thickness in the range of 5 to 30 microns (μm). A typical PEM fuel cell has the following reactions:

Anode: $H_2 \rightarrow 2H^+ + 2e^-$ 1-1

Cathode : $\frac{1}{2}O_2 + 2H^+ + 2e^- \rightarrow H_2O$ 1-2

Overall: $H_2 + \frac{1}{2}O_2 \rightarrow H_2O$ 1-3

Within the fuel cell, in addition to this chemical reaction, several coupled processes take place at the same time, including the diffusion of reactants across the electrodes, diffusion of protons across the membrane, heat generation and removal, water production at the cathode, and water transport through and out of the fuel cell. The rates of the reaction and these transport processes determine the dynamics of the fuel cell. These processes are dependent on the quality of the membrane-electrode assembly (MEA), flow field designs, and operating conditions (reactant flow rates, temperature, pressure etc.), all of which affect the overall performance of the fuel cell and thus are important aspects to consider in fuel cell design and operation.

In order to make fuel cell systems as commercially competitive as possible, as much cost as possible needs to be removed from system components without sacrificing performance and durability. Fuel cell durability requirements limit the performance loss to a few tens of mVs over required lifetimes (1000s of hours). As fuel cell systems suffer from performance loss due to factors such as potential cycling, start/stop and idling conditions, there is very little tolerance for additional losses such as those due to contaminants. Intelligently selecting low cost materials for specific application in PEMFC

systems requires a level of understanding of potential contaminants from system components that does not currently exist.

1.4 Dissertation Outline

As mentioned earlier, this dissertation is focused on two projects. The first six chapters are focused on the first project and the last chapter addresses the second project. The objective of first project is to create a comprehensive mathematical model including thermal gradients and fluid flow to predict corrosion rates and mechanisms observed in state of the art molten salt heat transfer systems. Chapter 1 introduces the importance of the dissertation. It is generally believed that temperatures of heat transfer fluids (HTFs) will need to be higher than 750 °C to drive an advanced Bryton cycle or Rankine cycle with superheated steam to reach this target. To make this system technically feasible, HTFs need to be developed that can operate at these temperatures for long periods of time without significant degradation of either the HTFs or materials of construction for the system. Decreasing materials' corrosion will lower system maintenance costs due to less frequent component failure and replacement. Improvements in materials' durability will be achieved by creating a comprehensive model that will allow identification of critical parameters of corrosion mechanisms. While material durability studies have been conducted for lower temperature HTFs that are common in industry, detailed characterizations of molten salt systems capable of high temperature operation at temperatures routinely exceeding 750°C have either not been performed or not been extensive. The corrosion management strategies employed with higher temperature salts is often drastically different when compared to those for the lower temperature nitrate salts that can utilize well known oxide passivation layers for corrosion prevention. Whereas at

higher temperatures, activity gradient driven mass transfer and thermal gradient driven mass transfer are often dominant, especially in many chloride and fluoride salt systems that are among the most promising HOT HTFs. This research will characterize corrosion and material degradation at these conditions and compare corrosion rates and mechanisms with state-of-the-art systems.

Chapter 2 presents a literature review of the corrosion, specifically current research in corrosion at high temperature molten salt systems and cathodic protection. Chapter 3 develops a corrosion model that allows reliable simulation of the processes under realistic conditions that can help to identify the critical parameters of corrosion and improve the material durability. Finally in Chapter 4, the previously reported corrosion model is developed under magnesium (Mg) cathodic protection.

For the second project of the dissertation, the purpose is to identify the performance loss and recovery of a fuel cell due to contaminants arising from Balance of Plant (BOP) components via a combination of experimental data and mathematical models. An analysis procedure was developed to quantify the various potential losses caused by contaminants during both fuel cell contamination and recovery operations. These important impacts of contamination are considered, which are the adsorption onto the Pt surface (kinetic losses) and ion exchange with the membrane and ionomer in the catalyst layer. Chapter 5 presents a literature review in addition to the experimental procedure and model development for the second project.

CHAPTER 2. LITERATURE REVIEW

2.1 Concentrated Solar Power Plant (CSP)

The first CSP plant (1982-1988) in California, US used water/steam systems as a heat transfer fluid. Its six-year test and power production program proved that the technology operates reliably and has both very low environmental impact and high public acceptance. There were, however, two key disadvantages to the water/steam system at this plant. First, the receiver was directly coupled with the turbine, causing the turbine to drop offline each time a cloud came by, and second, the oil/rock thermal storage system was not efficient because of thermodynamic losses. In parallel with testing of this plant, a series of studies funded by the U.S. Department of Energy and industry examined advanced power tower concepts using single-phase receiver fluids [16]. Molten salts have been studied for their possibility of high working temperatures, low melting points, moderate density, high heat capacity, and high thermal conductivity, in addition to long term thermal stability (or chemical stability with less corrosion to containers) and low cost [17].

2.2 Molten Salt Applications in CSP Plant

The primary molten salt candidate was a binary mixture of 60% sodium nitrate and 40% potassium nitrate (Solar Salt). The primary advantages of molten nitrate salt as the heat transfer fluid for a solar power tower plant include a lower operating pressure and better heat transfer (and thus higher allowable incident flux) than a water/steam receiver.

This translates into a smaller, more efficient, and lower cost receiver and support tower [16]. Solar Salt has a thermal stability (below 600 °C) and a relatively high melting point (220 °C). A new heat transfer fluid called Hitec, which is a ternary salt mixture of 53% KNO_3, 7 % $NaNO_3$ and 40% $NaNO_2$, has been considered to replace the Solar Salt because of its low freezing point of 142 °C [18]. Hitec is thermally stable at temperatures up to 454 °C, and may be used at temperature up to 538 °C for a short period [19]. A modified version, Hitec XL, is a mixture of 48 % Ca $(NO_3)_2$, 7% $NaNO_3$ and 45% KNO_3 which melts at about 133 °C and may be used at a temperature up to 500 °C [18]. Different compositions of $Ca(NO_3)_2$/ $NaNO_3$/ KNO_3 have been identified in the open literature as eutectic salts [18, 20]. The ternary eutectic salt with composition of 44% $Ca(NO_3)_2$/ 12% $NaNO_3$, 44% KNO_3 melts at 127.6 °C and its thermal stability is good at up to 622 °C [20].

It is proposed to replace molten-nitrate-salt coolant systems with molten-fluoride-salt coolant systems and thus make it possible to increase peak salt coolant temperatures from 565 °C to between 700 °C and 850 °C. Increasing the peak coolant temperatures and using a higher temperature closed-Brayton-power cycle have the potential to increase heat-to-electricity efficiency by 20–30% with an equivalent reduction in capital costs [21].

Molten fluoride salts have been used on a large industrial scale for a century. Since the 1890s, essentially all aluminum has been produced by the Hall process which used sodium-aluminum-fluoride-salt at 1000°C in a graphite-lined bath. In the 1950s, the United States launched a large program to develop a nuclear-powered aircraft by using molten salt reactors (MSRs) were to provide the very high- temperature heat source, with the heat transferred to a jet engine via an intermediate heat-transport loop. In the 1960s and 1970s, the MSR was investigated as a thermal-neutron breeder reactor. Fluoride salts were chosen

for these applications because of their high-temperature heat transfer and nuclear characteristics [21]. Several types of molten fluoride and chloride salts, including $LiF-BeF_2$ (also known as FLiBe [67-33 mol%]), LiF-NaF-KF (also known as FLiNaK [46.5-11.5-42 mol%]), and $KCl-MgCl_2$ (67-33 mol%), have been investigated recently by several Japanese and U. S. groups ($LiF-BeF_2$ and LiF-NaF-KF) and by the University of Wisconsin (LiF-NaF-KF and $KCl-MgCl_2$) in support of fusion reactor and VHTR reactor concepts, respectively. At operating temperatures, these salts have heat transfer properties similar to those of water. However, the boiling points are above 1000 °C, which allows low-pressure operations [22]. Table 2.1 presents a summary of the properties of molten halide salts for using in CSP plants. Certain factors in this table, such as melting point and vapor pressure, can be viewed as stand-alone parameters for screening candidates [23]. In the area of nuclear energy systems, molten choloride salts are also being considered as heat transport fluids to transfer high temperature process that from nuclear reactors to power chemical plants. Electrochemical reprocessing of used metallic fuel is performed routinely in molten LiCl-KCl electrolyte. Molten $NaCl-KCl-MgCl_2$ salt was used in reprocessing of the liquid metal fuel at Brookhaven National Laboratory in the 1950s as part of the Liquid Metal Reactor Experiment. Free energy of formation vs temperature diagrams constructed for chlorides show that alkali chlorides and alkaline earth chlorides are more thermodynamically favored than the transition metal chlorides [24]. Williams discussed the influence of the price of the components with different salt mixtures [23]. His conclusions determined that magnesium chlorides are the least expensive of all, while fluorides, fluoroborates and Li-containing mixtures increase the price of the coolant. Table 2.2 shows the estimated raw material costs for various salt mixtures [23]. From the

14

standpoint of the CSP plant, it is important to select a salt that possesses good heat transfer characteristics, is relatively easy to handle, and not prohibitively expensive. Based on the above issues it was decided that most of the experiments be performed for this project using 68%KCl-32%MgCl$_2$ (mol%), with a couple tests utilizing FLiNaK salt for comparison purposes. KCl-MgCl$_2$ has less heat transfer properties, in comparison to the FLiNaK molten salt, but it is one of the most inexpensive molten halide salts.

2.3 Super-alloys for CSP Plants

The development of the CSP plant much depends on the progress in creating such structural materials that should meet a number of special requirements:

- A high corrosion resistance of molten salt melts;

- Adequate high-temperature strength;

- Good manufacturability (ability to be deformed, machined, welded, etc.).

The corrosive impact on these factors is significant in most situations, and may be critical in some. In general, for structural materials, corrosion resistance is not the primary criterion for selection. In most cases, for the applications described above, the mechanical properties are the major needs. Obviously, this usually means strength (rupture strength, creep strength, toughness) at the required service temperature. Since in all cases the systems have to be fabricated at ambient temperature, and in normal operation will need to be cooled to ambient temperature several times during their service lives, there will also be some mechanical property requirements for low temperatures: the usual minimum requirement is adequate fracture toughness.

Table 2.1 Thermophysical properties of some molten salts compositions [23].

Salt	Formula Weight (g/mol)	Melting point (ºC)	900ºC vapor pressure (mm Hg)	Heat-transfer properties at 700 ºC			
				ρ, density (g/cm^3)	$\rho\, C_p$, volumetric heat capacity (cal/cm^3 ºC)	μ, viscosity (cP)	k, thermal conductivity (W/m K)
LiF-NaF-KF	41.3	454	~ 0.7	2.02	0.91	2.9	0.92
NaF-ZrF$_4$	92.7	500	5	3.14	0.88	5.1	0.49
KF-ZrF$_4$	103.9	390	1.2	2.80	0.70	< 5.1	0.45
LiF-NaF-ZrF$_4$	84.2	436	~ 5	2.92	0.86	6.9	0.53
LiCl-KCl	55.5	355	5.8	1.52	0.435	1.15	0.42
LiCl-RbCl	75.4	313	--	1.88	0.40	1.30	0.36
NaCl-MgCl$_2$	73.7	445	< 2.5	1.68	0.44	1.36	0.50
KCl-MgCl$_2$	81.4	426	< 2.0	1.66	0.46	1.4	0.4
NaF-NaBF$_4$	104.4	385	9500	1.75	0.63	0.9	0.4
KF-KBF$_4$	109.0	460	100	1.70	0.53	0.9	0.38
RbF-RbF$_4$	151.3	442	< 100	2.21	0.48	0.9	0.28

Table 2.2 Estimated raw material costs for various salt mixtures [23].

Salt	Composition (mol %)	Composition (wt %)	Raw material cost ($/kg–salt mixture)	Cost/volume ($/L at 700ºC)
KCl-MgCl$_2$	68-32	62-38	0.21	0.35
NaCl-MgCl$_2$	58-42	46-54	0.25	0.42
NaCl-KCl-MgCl$_2$	20-20-60	14-18-68	0.28	0.50
LiCl-KCl-MgCl$_2$	9-63-28	5-61-34	0.74	1.13
KF-KBF$_4$	25-75	13-87	3.68	6.26
LiCl-KCl-MgCl$_2$	55-40-5	40.5-51.5-8	4.52	7.01
LiCl-KCl	59.5-40.5	45.5-54.5	5.07	7.71
NaF-NaBF$_4$	8-92	3-97	4.88	8.55
NaF-ZrF$_4$	59.5-40.5	27-73	4.02	12.63
KF-ZrF$_4$	58-42	32.5-67.5	4.85	13.58
LiF-NaF-KF	46.5-11.5-42	29-12-59	7.82	15.79

The selected materials must be fabricable to the extent required to manufacture the system; but there is often a further requirement in the fabricability of the materials since it is likely that during service repairs and replacements may be necessary.

For higher temperature applications, it is necessary to produce alloys with higher intrinsic oxidation resistance. Developments along these lines had begun for quite different reasons in the late 1920s, when a series of alloys were developed, primarily for electric resistance heater applications, which relied on the growth of a protective Cr_2O_3 'chromia' scale. These alloys were nickel or cobalt based, and when the first gas turbines were developed for aviation purposes these were selected for the hot components [25].

A National Aeronautic and Space Administration (NASA) study determined that the tendency for common alloying constituents to corrode in molten fluoride salts increased in the following order: Ni, Co, Fe, Cr, Al. This is supported by Gibb's free energy of formation of various fluorides [26].

The present-day corrosion-resistant nickel alloys, which can be well deformed and welded, belong to three main alloying systems: Ni-Mo, Ni-Cr, Ni-Cr-Mo. Simultaneous alloying of nickel with chromium and molybdenum makes it possible to create ultrahigh-resistance alloys in a wide range of corrosive active media of oxidation/reduction character. Along with a high corrosion resistance, the alloys show an exceptional resistance to local types of corrosion. Besides, these alloys are heat-resistant at high temperatures. They combine high strength and plasticity from temperatures below zero to 1200°C. The effect of mutual effect of chromium and molybdenum on the corrosion resistance of the alloy is determined by the properties of aggressive medium [27].

Haynes Alloy N was developed in the 1950s for molten salt service in the Aircraft Nuclear Propulsion program. Conventional high temperature alloys containing about 20% chromium proved susceptible to corrosion by the proposed molten salt heat transfer medium. It was successfully used in the ORNL Molten Salt Reactor Experiment in the 1960s. Some variations of Alloy N, for example, adding titanium, (McCoy, et al., 1970) were developed for easier weldability and better performance in the high radiation environments of reactors [28].

The primary materials used while investigating corrosion in high temperature CSP applications are: Haynes-230, Incoloy 800H, and Haynes NS 163. These alloys were chosen over continued testing of different alloys because their mechanical properties are much more suitable to sustained high temperature operation. Table 2.3 shows the compositions of these different alloys.

Table 2.3. Compositions of super-alloys.

Alloy (wt%)	Cr	Mo	W	Al	Ti	Fe	C	Co	Ni	Mn	V	Si
Incoloy 800H	20.82	-	-	0.54	0.52	46.3	0.07	0.04	30.69	0.49	-	0.33
Haynes 230	22.08	1.23	14.17	0.37	0.01	1.02	0.10	0.21	59.98	0.52	-	0.31
Haynes NS 163	27.71	0.27	-	0.17	1.33	21.24	0.092	40.66	8.06	0.22	0.05	0.20

As it is shown in Table 2.3 these super-alloys have a large Al and Cr component to aid in the prevention of high temperature oxidation. As discussed earlier both Al and Cr are soluble in molten halide salts.

2.4 Corrosion of Super-alloys in Molten Salt

Compatibility of molten salts with structural alloys centers on the potential for oxidation of the structural metal from the elemental state to the corresponding fluorides or chlorides with corresponding reduction of the oxidizing agent. Electrochemically, the molten salt/metal surface interface is very similar to the aqueous solution/metal surface interface. Many of the principles that apply to aqueous corrosion also apply to molten salt corrosion such as anodic reactions leading to metal dissolution and cathodic reduction of an oxidant [22]. The laws of electrochemistry and mechanisms of corrosion are comparable for aqueous solutions and molten salts. According to Joseph R. Davis [29] the most common mechanism is the oxidation of the metal to ions, similar to aqueous corrosion. For this reason, molten salt corrosion has been identified as an intermediate from of corrosion between molten metals and aqueous corrosion.

The corrosion of metals in molten salt can be well explained by a combination of anodic dissolution of metal (i_a) and cathodic reduction of oxidants (i_c) under a mixed potential as well as in aqueous solution. The polarization curve is schematically illustrated in Figure 2.1. The partial anodic current i_a and cathodic current i_c correspond to the metal dissolution and the reduction of oxidants respectively in corrosion processes. They are represented by broken curves in Figure 2.1. The rates of anodic reaction and cathodic reaction must become equal at a corrosion potential E_{corr}. That is to say, the partial anodic current and the partial cathodic current become equal in magnitude and opposite in direction. And the value is designated the corrosion current, i_{corr}:

$$i_a = i_c = i_{corr} \qquad\qquad 2\text{-}1$$

Generally, the anodic reaction of corrosion in a molten salt corresponds to the dissolution of metals followed by the formation of metal oxides or salt films in the same way in aqueous solution. On the contrary, the cathodic reaction of corrosion differs with each molten salt and is much more complicated than the aqueous solution system [30]. The oxidation-reduction (corrosion) can occur by several processes in molten salt, including: Uniform surface corrosion, differential solubility due to thermal gradients, and galvanic corrosion.

Intrinsic corrosion (uniform surface corrosion) with molten salt as the reactant; this mechanism pertains primarily to nitrates and nitrites, not to fluorides or chlorides [29]. According Ozeryanaya [31] the oxidation of metals by molten chlorides is an electrochemical process of ion exchange between the metal and the salt:

$$M \rightarrow M^{n+} + ne^- \qquad\qquad 2\text{-}2$$

$$ox + ne^- \rightarrow red \qquad\qquad 2\text{-}3$$

These reactions take under conditions close to equilibrium with respect to the salt adjacent to the electrode. Even in the absence of oxidizing contaminants (oxygen, water, etc.) the salt cations which can be reduced to the elemental state, or to a lower state, can act as metal-depolarizers.

Corrosion by oxidizing contaminants in the molten salts (such as HF, HCl, H_2O), residual oxides of metals, or easily reducible ions, especially some polyvalent metal ions. Impurities in the melt or in the gas phase control the corrosion/oxidation potential of the melt, increase the anodic reaction rate, or change the acidic or basic nature of the melt.
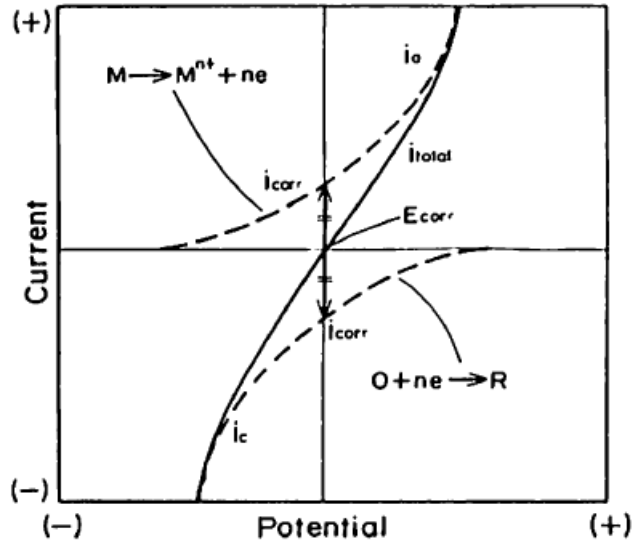
Figure 2.1 Schematic polarization curves for the metallic corrosion system. i_a and i_c indicate the partial anodic and cathodic currents respectively [30].

Differential solubility due to thermal gradients (between hot and cold zones) in the molten salt system with formation of a metal ion concentration cell that drives corrosion. Thermal gradient in the melt can cause dissolution of metal at hot spots and metal deposition at cooler spots. The result is very similar to aqueous galvanic corrosion [29].

Galvanic corrosion, wherein alloys with differing electromotive potentials are maintained in electrical contact by the molten salt, is driving the oxidation of the anodic material. According to Ozeryanaya [31] at high temperatures, not only the salt components but also the container material can act as metal oxidizers. He showed the formation of metal alloys through molten salts goes in a strictly defined direction: the more chemically active metal M_1 (electronegative) corrodes in the molten bath:

$$M_1 \rightarrow M_1^{m+} + me \qquad\qquad 2\text{-}4$$

The low-oxidizing-level ions M_1^{m+} of that metal transfer by convection towards the more electropositive metal M_2. On the surface of that metal they disproportionate:

22

$$nM_1^{m+} \leftrightarrow (n-m)M_1 + m\, M_1^{n+} \qquad \text{at } n > m \qquad \text{2-5}$$
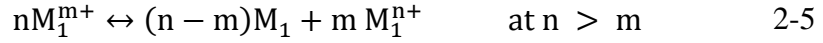
The atoms of the active metal M_1 formed in this way produce an alloy M_1-M_2 while the M_1^{n+} ions, reaching the surface of M_1, accelerate its corrosion:

$$(n-m)M_1 + m\, M_1^{n+} \leftrightarrow n\, M_1^{m+} \qquad \text{2-6}$$
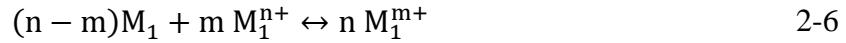
For instance, the corrosion rate of a Cr specimen in molten NaCl at 900°C increases 30 times if an alundum crucible (inert with respect to the salt) is replaced by an iron crucible. In the latter case Cr corrodes as:

$$Cr \rightarrow Cr^{2+} + 2e^- \qquad \text{2-7}$$

while on the crucible surface the following reaction takes place:

$$3Cr^{2+} \leftrightarrow 2\, Cr^{3+} + Cr_{alloy} \qquad \text{2-8}$$

High temperature corrosion in molten salts often exhibits selective attack and internal oxidation. As an example chromium depletion in iron-chromium-nickel alloy systems can occur by the formation of a chromium compound at the surface and by the subsequent removal of chromium from the matrix, leaving a depleted zone. Thus, the selectivity removed species moved out, while vacancies moved inward and eventually form voids. The voids tend to form at grain boundaries in most chromium- containing metals [29]. Figure 2.2 compares alloys high in nickel and chromium with and without exposure to FLiNaK salt, held at 850°C for 500 hours. The images demonstrate coupons exposed to the salt have significant weight loss along grain boundaries.

Corrosion of metals in fluoride salts was investigated for MSRs development as early as 1950. Various alloys were tested in mixtures of LiF, BeF$_2$, NaF, ZrF$_4$, ThF$_4$, NaBF$_4$, etc., up to about 1088 K using static experiments, convection loops and in-pile surveillance specimens; nickel alloys appeared to be more suitable than iron steels [32].
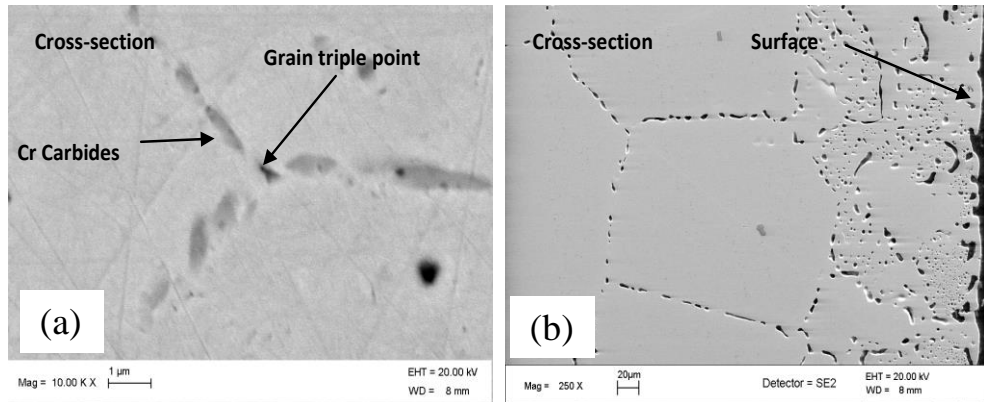
Figure 2.2 a) 10,000 magnification SEM image of Incoloy 800H held at 850˚C for 500 hours, no salt exposure, b) 250 magnification of Incoloy 800H held at 850˚C for 500 hours, FLiNaK exposure.

In most high temperature environments corrosion can be controlled by one of the following mechanisms, (i) by the formation of a protective film, or [33] by the establishment of a thermodynamic equilibrium between the material and the environment [4]. Elements such as Cr, Al, and Si are added to alloys to promote the formation of self-healing protective oxide films that act as diffusion barriers and prevent further rapid oxidation in oxidizing environments such as air. Prevention of hot corrosion (sulfidation and oxidation from molten salt deposits left from fuel impurities) in fossil fueled boilers and turbines also rely on passive films of Cr and Al oxides present at the alloy surface [32]. Additionally, chemical additions to the fuel aid in removal corrosive salt slags [32]. Gas turbines and boilers that burn fossil fuels use these corrosion prevention methods extensively. Molten fluoride salt corrosion of most high temperature alloys however, is fundamentally different from air oxidation and hot corrosion [6]. Unlike conventional air/aqueous oxidation, the protective oxide films are soluble in molten fluoride salts or otherwise unprotective [15]. The corrosion rate therefore depends on the thermodynamic driving force and the kinetics of the various corrosion reactions [15]. In general, there are

24

three driving forces for corrosion in molten fluorides: impurities, temperature gradients, and activity gradients [34].

Several high temperature Fe-Ni-Cr and Ni-Cr alloys: Hastelloy-N, Hastelloy-X, Haynes-230, Inconel-617, and Incoloy 800H, and a C/SiSiC ceramic were exposed to molten FLiNaK with the goal of understanding the corrosion mechanisms and ranking these materials for their suitability for molten fluoride salt heat exchanger and thermal storage applications. The tests were performed at 850°C for 500 h in sealed graphite crucibles under an argon cover gas. Corrosion was noted to occur predominantly from dealloying of Cr from the alloys, an effect that was particularly pronounced at the grain boundaries [34].

Inconel alloy 600 and certain stainless steels become magnetic after exposure to molten fluoride salt. This magnetism is caused by the selective removal of the chromium and the formation of a magnetic iron-nickel alloy covering the surface.

Molten salts consisting of chlorides are important but they have been studied less than fluoride system. In general chloride salts attack steels very rapidly, with preferential attack of the carbides. In chloride salts no protective oxide scale is formed on the nickel base alloys. The attack of metal surfaces in pure sodium chloride has been observed at temperatures above 600 °C.

In most cases with iron-nickel-chromium alloys, the corrosion takes the form of intergranular attack. An increase of chromium in the alloy from 10% to 30% increases the corrosion rate by a factor of seven. Thus, the intergranular attack is probably selective with respect to chromium. The chromium removal begins at the grain boundary and continues

with diffusion of chromium from within the grain to the boundary layer, gradually enlarging the cavity in the metal. The gross corrosive attack is probably caused by the free chlorine, which is highly oxidizing material, attacking the highly active structure-sensitive sites, such as dislocations and grain boundaries. Figure 2.3 shows an example of intergranular corrosion of Ni-Cr-Fe alloy by molten chloride salt after 6 months at 870°C [29].
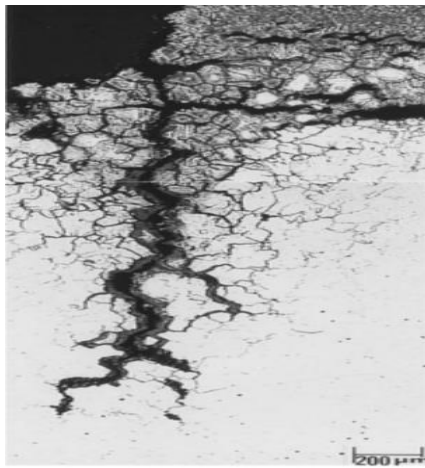
Figure 2.3 An example of intergranular corrosion of Ni-Cr-Fe alloy by molten chloride salt after 6 months at 870°C [29].

2.5 Cathodic Protection

It is well known that cathodic protection (CP) can inhibit metal corrosion [35, 36]. Among the various corrosion control methods available, cathodic protection is a widely used technique adopted to control the corrosion of the alloy by effecting a change in potential from the natural corrosion potential (E_{corr}) to a protective potential in the immunity region. In principle, it can reduce or prevent the corrosion of any metal or alloy

26

exposed to any electrolyte. Corrosion can be reduced to virtually zero, and a properly maintained system will provide protection indefinitely. The first application of CP can be traced back to 1824, when Sir Humphrey Davy, in a project financed by the British Navy, succeeded in protecting copper sheathing against corrosion from seawater by the use of iron anodes [37]. CP reduces the corrosion rate by cathodic polarization of a corroding metal surface. Cathodic polarization reduces the rate of the half-cell reaction with an excess of electrons. Metal structure can be cathodically protected by connection to a second metal, called a sacrificial anode, which has a more active corrosion potential. The noblest structure in this galvanic couple is cathodically polarized, while the active metal is anodically dissolved. Magnesium, zinc and aluminum sacrificial anodes, provide long-term cathodic protection [38]. Matson et.al [39] developed the experiments to determine the feasibility of using cathodic protection to reduce the attack in the fluoride volatility process for recovery of nuclear fuel at 650 °C. Their results show that CP would reduce the corrosion of submerged Inor-8 components in fused fluoride salt systems by factor of 10. For the KCl-$MgCl_2$ molten salt system, metallic Mg was identified as a potential corrosion inhibitor [40]. As it is the most electrochemically active metal, which corrodes so readily in some environments that Mg and Mg alloys are purposely utilized as sacrificial anodes in engineering applications [41]. Figure 2.4 shows the electrochemical equilibrium potential for Mg going to $MgCl_2$ and compares that to the potentials for other alloy components going to their molten chlorides. This shows that the equilibrium potential is well below the equilibrium potentials of the Cr that is selectively oxidized.
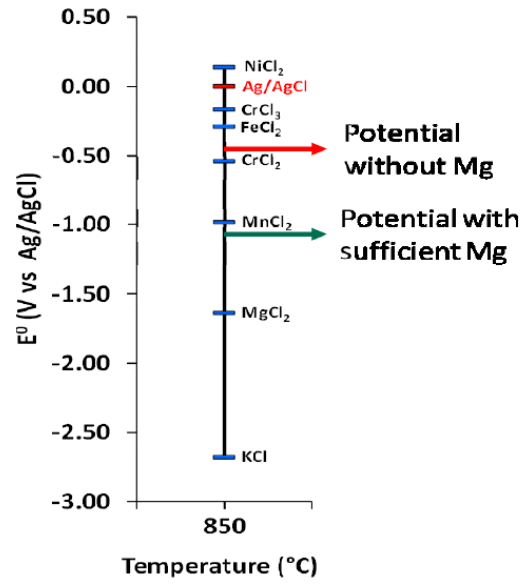
Figure 2.4 Electrochemical potential for alloy components and Mg corrosion inhibitor [40].

2.6 Modeling of High Temperature Corrosion

Corrosion predictive models are a very useful tool that can be used to determine corrosion allowances, make predictions of facilities remaining life, and provide guidance in corrosion management. For high temperature molten salt systems, it has been found that Cr will be dealloyed primarily in high temperature regions where selective attack results in the formation of voids [42]. If the chromium content in the depleted-zone is lower than a critical level, it is then vulnerable to environmental corrosion, leading to inter-granular attack [43], or intergranular stress corrosion cracking (IGSCC) [44]. For these reasons, many studies have been devoted to correlating IGSCC to grain boundary characteristics and to a quantitative evaluation of the dechromised zones by experimental analysis and empirical or analytical computer modelling [44-46]. Thrvaldsson et al. [45] used the error function solution of Fick's second law for Cr diffusion, for Cr depleted zones adjacent to the grain boundaries of stainless steel. They used the error function solution, to give a good

28

approximation of the depleted zone morphology in the early stages of aging. A three dimensional (3-D) modeling technique has been also developed to predict the Cr depletion from grain boundaries in a Ni-Cr-Fe alloy (Inconel 690) [44]. In Anderko et al. [46] a grain boundary microchemistry model has been developed that calculate the chromium and molybdenum depletion profiles in the vicinity of grain boundaries. Their model could relate the repassivation potential to the microchemistry and environmental conditions. The literature models have been successful in predicting the Cr depletion profiles. However, the corrosion model developed for nickel-based alloys in molten salts that considers the fluid flows in the non-isothermal condition of CSP plants has not been fully defined. A corrosion model reliably simulating the corrosion processes under realistic CSP plant conditions can help identify critical corrosion parameters that can lead to improved material durability. Combined CFD and electrochemical analysis of CSP plant heat transfer systems can lead to predictions and insights on the interplay of thermal and concentration gradients under convection. The coupling of the corrosion model with CFD can allow predictions of local corrosion rates as functions of heat and mass transport in the local environment of the heat transfer systems.

CHAPTER 3. MULTIDIMENSIONAL MODELING OF NICKEL ALLOY CORROSION INSIDE HIGH TEMPERATURE MOLTEN SALT SYSTEMS

One challenge with concentrated solar power (CSP) systems is the potential corrosion of the alloys in the receivers and heat exchangers at high-temperature (700-1000 °C), which leads to a reduction of heat transfer efficiency and influences the systems durability. In this work, a corrosion model has been developed to predict the rates and mechanisms for corrosion of a nickel-based alloy that is in contact with a molten salt heat transfer system. In addition to accounting for heat and mass transfer effects on the corrosion, the model takes into account the electrochemical kinetics. Coupled with computational fluid dynamics (CFD), the local electrochemical environment and corrosion rates in a high temperature molten salt system can be predicted. The kinetic and heat and mass transfer parameters used in the model are based on experimental studies conducted in a thermosiphon. The immersion cell was designed to expose coupons to the molten salt at isothermal or non-isothermal conditions between 700-1000 °C. The model can predict the effect of thermal gradients between the top and the bottom of the reactor which induce natural convection of the molten salt. The model has been validated against experimental results at different isothermal and non-isothermal conditions and good agreement has been achieved between the model predictions of the corrosion rates and corrosion potentials with the experimental observations.

3.1 Introduction

Concentrated solar power (CSP) is a promising technology for large-scale, dispatchable renewable electricity generation. These systems provide an environmentally-friendly source of energy, producing almost no pollution and requiring only sunlight and occasional maintenance once built. Molten salts have been proposed for use with high-temperature Brayton and superheated Rankine cycles in some of these systems. These molten salts are usually molten halides above ~550 °C due to their relatively low melting points, very high boiling points, and good heat transfer properties [47, 48]. Superalloys have been developed that are able to withstand high temperatures (700-1000 °C) because of properties such as: high strength, good oxidation resistance on the air side, and creep-rupture resistance. However, a drawback with using high-temperature molten halide salts is the potential material degradation if specific alloys/salt systems are paired together [49]. Decreasing corrosion of the alloys where they are in contact with the molten salt will lower system maintenance costs due to less frequent component failures and replacement. The corrosion management strategies employed with high-temperature halide salts are often drastically different compared to those of lower temperature nitrate salts that have well-known oxide passivation layers for corrosion prevention. Activity gradient-driven mass transfer and thermal gradient-driven mass transfer are often dominant in many chloride and fluoride salt systems, which are among the most promising high operating temperature heat transfer fluids [50]. A number of experimental studies on the corrosion behavior of nickel-based alloys in molten halides have been performed at high temperatures [13, 26, 51-55]. Several different literatures [13, 26, 34, 51-56] have shown that the corrosion in molten salts mainly occurs through the dissolution of alloying elements into the melt. Olson et al. [34] found

that corrosion mainly occurred at the grain boundaries of nickel-based alloys and the corrosion rate were dependent on the initial Cr-content of these alloys. In another work Olson et al. [51] described the effects of crucible material choice on nickel-based alloy corrosion rates in immersion tests in high-temperature molten salt systems. Their experimental work demonstrated that graphite and nickel crucibles can promote the dissolution of Cr from nickel-based alloys, while the pyrolytic boron nitride (PyBN) crucible had almost negligible interaction with the alloys. Ludwig et al. [56] measured the dissolved Cr concentration in the high-temperature molten salt system exposed to Cr containing structural materials. Their results showed that there is a linear correlation between the integrated currents from the anodic curve and the Cr content of the salt. The work by Wang et al [53] showed the galvanic corrosion behavior of pure metals in high-temperature molten salt systems. Several studies have also demonstrated that the corrosion behaviors are highly affected by the presence of impurities and humidity in molten salts [13].

Some studies also focused on the modeling of the chromium depletion of nickel-based alloys from grain boundaries [45]. Thrvaldsson et al. [45] used the error function solution of Fick's second law for Cr diffusion, within Cr-depleted zones adjacent to the grain boundaries of stainless steel. They used the error function solution, to give a good approximation of the depleted zone morphology in the early stages of aging. A three dimensional (3D) modeling technique has also been developed to predict the Cr depletion from grain boundaries in a Ni-Cr-Fe alloy (Inconel 690) [44]. However, the corrosion model developed for nickel-based alloys in molten salts, which considers the fluid flows in the non-isothermal condition of CSP plants has not been fully defined. A corrosion

model reliably simulating the corrosion processes under realistic CSP plant conditions can help identify critical corrosion parameters that can lead to improved material durability. Combined CFD and electrochemical analysis of CSP plant heat transfer systems can lead to predictions and insights on the interplay of thermal and concentration gradients under convection. The coupling of the corrosion model with CFD can allow predictions of local corrosion rates as functions of heat and mass transport in the local environment of the heat transfer systems. In our previous work [57] a high temperature corrosion model was developed that accounts for the impact of thermal gradients and fluid flow on the corrosion rate for the selective oxidation of chromium. Dimensionless parameters were utilized in that model to characterize the heat and mass transfer in the system. Dimensionless analyses of Sherwood number led to prediction of the limiting currents (i.e., corrosion rates) assuming zero surface concentration of chromium. The model could predict the average corrosion rate, although it only considered the effect of mass transfer and could not evaluate the local electrochemical environment.

In order to understand the corrosion phenomena in CSP plants, it is important to determine not only the average corrosion rate but also the distribution of the corrosion at the surface of the alloys that are used in CSP plants. As evidenced by recent experiments, corrosion happens in a layer of finite thickness, possibly microns to hundreds of microns thick at the surface of the alloys (i.e. the studies by the National Aeronautics and Space Administration (NASA) [58] showed that the depth of reaction can change from 8 μm to 270 μm for different alloys). The effect of critical parameters like the diffusion of metal cations in this layer is critical and it cannot be fully understood with only experimentation. A modeling approach can not only help to calculate the uniformity of the corrosion at the

surface of the alloys but can also help to identify the correlation between the critical corrosion parameters and the corrosion rate at the high-temperature conditions of CSP plants. This paper develops a high-temperature corrosion model that couples electrochemical kinetics with heat and mass transfer. A CFD model is used to calculate the temperature gradient and fluid flow, then, the corrosion potential and corrosion rate are calculated by adding user defined subroutines in the system to account the electrochemistry of the reactions. The corrosion mechanisms of KCl-MgCl$_2$ salt and Haynes 230 alloy were considered which are of interest in CSP plants. The KCl-MgCl$_2$ salt used in this work is composed of 32 mol% MgCl$_2$ and 68 mol% KCl. The main compositions of Haynes 230 are Ni (59.98 wt%) and Cr (22.08 wt%). The kinetic, heat and mass transfer parameters used in the model are based on experimental coupon studies conducted between 700-1000°C within KCl-MgCl$_2$ molten salt in crucibles and thermosiphon that exposed coupons to the isothermal and non-isothermal conditions, respectively [57]. This corrosion model coupled with CFD provides enhanced evaluations of corrosion as a function of heat and mass transport to the local electrochemical environment in the heat transfer systems.

3.2 Experimental Procedures

Since the experimental procedure has been reported in detail in Appendix A, they will only be briefly discussed here. A thermosiphon was designed to test the exposure of metal coupons to both the isothermal and the non-isothermal conditions. There were three isothermal cases in which the temperature was kept constant in the system at 750, 850, and 950 °C. Due to the constant temperature, there was no fluid flow in the system. There were also two non-isothermal conditions where there were temperature gradients inside the

thermosiphon (i.e., non-isothermal conditions with temperature gradients of 600-850 °C and 800-950 °C around the coupons). In these conditions, the fluid flow circulated by natural convection due to changes in the molten salt properties between the top and bottom of the thermosiphon. Figure 3.1 shows a sketch of the thermosiphon used for corrosion measurements. The thermosiphon had four coupons placed in both the bottom and the top that were called the hot and cold zones respectively for the non-isothermal conditions. They are also shown in Figure 3.1. For the non-isothermal conditions, hot and cold zones were attained by inserting the bottom of the thermosiphon into a furnace, with the top either in an insulated region or partially out of the furnace. After the entire salt media was added to the thermosiphon, the thermosiphon was brought to the final temperature and the experiment began. At the end of the exposure period, the reactor heating was turned off and the contents were allowed to cool to room temperature. Afterwards, the samples were broken out of the condensed salt media and cleaned for analysis. A sample of the salt was saved as well for analysis by using inductively coupled plasma atomic emission spectroscopy (ICP-AES) to examine trace elemental impurities. The primary post-experimental measurements were the mass loss and change in physical dimensions using the analytical balance and caliper measurements, respectively. These measurements were made using the analytical balance and caliper measurements, respectively.

3.3 Model Development

3.3.1 Model Geometry

The model geometry was based on the thermosiphon that was designed to test the effect of exposure of metal coupons to both the isothermal and the non-isothermal conditions

35

(i.e., Experimental Procedures). Figure 3.2 shows the model geometry and computational mesh of the thermosiphon that was created by CATIA® and HyperMesh®, respectively to represent the experimental system. The cylindrical geometry and symmetry in the thermosiphon design allows for simplification of the computational domain as shown in Figure 3.2. Symmetric boundary conditions were applied to a 90° section of the model for the CFD study. The thermosiphon consists of the Ni crucible and a Ni crucible insert, the Haynes 230 coupons, which are located at the top and bottom of the thermosiphon, and eutectic KCl-MgCl$_2$.
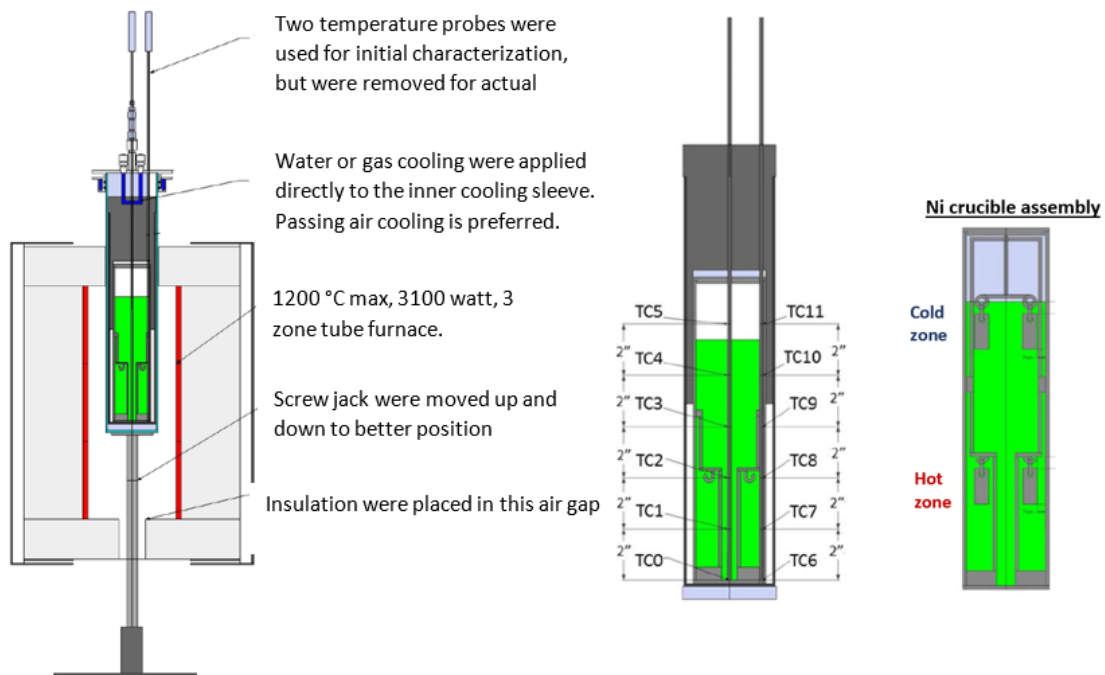
Figure 3.1 Thermosiphon reactor for non-isothermal corrosion experiments. Assembled reactor shown within well of furnace (left), reactor showing thermocouple locations for thermal profile experiments (center), and internal corrosion vessel shown with sample locations in upper cold zone and lower hot zone (right) [57].
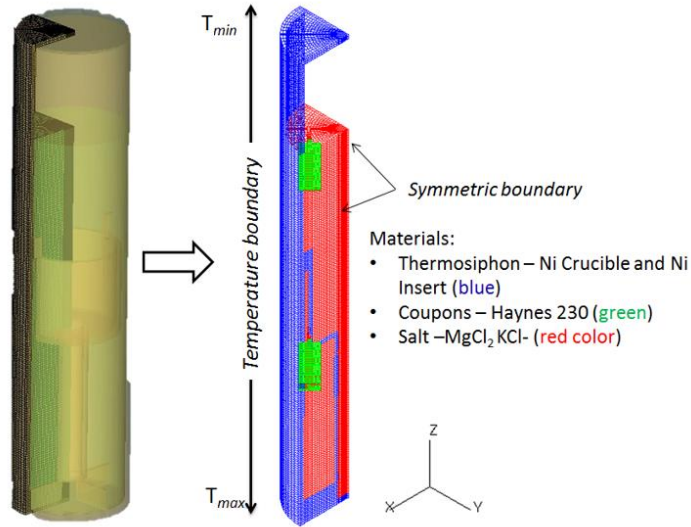
Figure 3.2 The model geometry of the thermosiphon consists of a Ni crucible, a Ni crucible insert, coupons and the salt [57].

Table 3.1 shows the KCl-MgCl$_2$ properties used for the model predictions. The temperature boundary conditions at the surface of the thermosiphon were applied to match the formerly-used experimental measurements for non-isothermal conditions. Equations 3-1a and 3-1b calculate the temperature boundary conditions as a function of height for the low temperature (600-850 ℃) and high temperature (800-950 ℃) non-isothermal cases, respectively.

$$T = \begin{array}{ll} 820 + 200\,z & 0 \leq z \leq 0.05m \\ 869 - 781\,z & 0.05 \leq z \leq 0.242m \\ 2163 - 6129\,z & 0.242 \leq z \end{array} \qquad \text{3-1a}$$

$$T = \begin{array}{ll} 1000(1 - z) & 0 \leq z \leq 0.05m \\ 976 - 521\,z & 0.05 \leq z \leq 0.242m \\ 2997 - 8871\,z & 0.242 \leq z \end{array} \qquad \text{3-1b}$$

Table 3.1. Equations for KCl-MgCl$_2$ salt properties as inputs to the model

Property	Unit	Equation	Temperature	Remark
Density	(kg m^{-3})	$\rho = 2000.7 - 0.4571T$	1030-1140K	Ref. [57]
Dynamic viscosity	(kg m^{-1}s^{-1})	$\mu = 1.46 \times 10^{-4} \exp(\frac{2230}{T})$	873-1073K	Ref. [57]
Thermal conductivity	(W m^{-1} K^{-1})	$\kappa = 0.0005T + {32.0}/{73.7} - 0.34$		Ref. [57]
Specific heat capacity	(J kg^{-1} K^{-1})	1150	No correlation	Ref. [57]
Vapor pressure	(mmHg)	< 2	1173K	Ref. [57]
Melting point	(°C)	435		
Boiling point	(°C)	>1418		

3.3.2 Governing equations and electrochemical kinetics

Figure 3.3 shows the SEM/EDS images of nickel-based alloy (Haynes 230) in contact with KCl-MgCl$_2$ salt. EDS results show that the Cr depletion at the surface and along the grain boundaries are the most important corrosion phenomena [57]. The electronegative metals (i.e., Cr) corrodes into the salt with a low oxidation state (i.e., CrCl$_2$) and can transfer to electropositive metals in the container alloys (i.e., Ni) by a simultaneous oxidation (CrCl$_3$) and reduction [16] reactions. The following oxidation and reduction reactions of Haynes 230 in the KCl-MgCl$_2$ salt are assumed and used in the model:

Oxidation reaction: $Cr + 2Cl^- \rightarrow CrCl_2 + 2e^-$ 3-2

Reduction reaction: $2CrCl_3 + 2e^- \rightarrow 2CrCl_2 + 2Cl^-$ 3-3
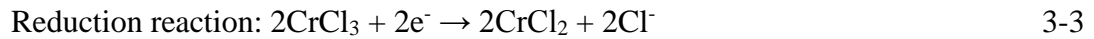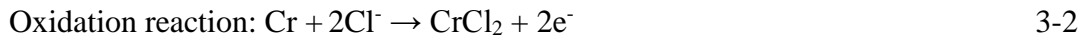
where CrCl$_3$ results from disproportionation reaction of CrCl$_2$ at the Ni crucible:

Oxidation reaction: $2CrCl_2 + 2Cl^- \rightarrow 2CrCl_3 + 2e^-$ 　　　　　　3-4

Reduction reaction: $Ni + CrCl_2 + 2e^- \rightarrow NiCr + 2Cl^-$ 　　　　　　3-5
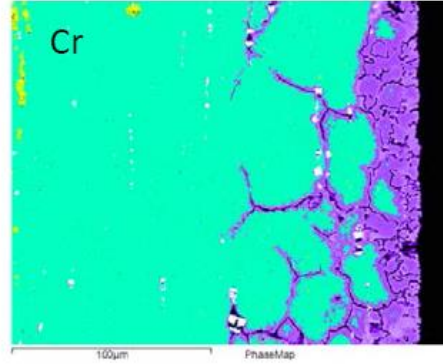
Figure 3.3. EDS X-ray mapping of Cr of Haynes 230 after 100 h exposure in KCl-MgCl$_2$ at 850 °C [57].

At high temperatures, not only the salt components but also the container material (i.e. Ni crucible in this paper) can act as a metal oxidizers [31], which means that there is a galvanic coupling between the Haynes-230 and the Ni crucible. As a result, the disproportionation product, Cr^{3+}, can facilitate the oxidation of the structural alloy [53]. The presence of Cr^{2+} and Cr^{3+} in molten salt are considered as an effect of Reactions 3-4 and 3-5 at the Ni crucible.

Reactions 3-2 and 3-3 can be rewritten as a simplified format of Equations 6 and 7 [53]:

Oxidation reaction: $Cr \rightarrow Cr^{2+} + 2e^-$ 　　　　　　3-6

Reduction reaction: $2Cr^{3+} + 2e^- \rightarrow 2Cr^{2+}$ 　　　　　　3-7

For the oxidation and reduction reactions (i.e. reactions 3-6 and 3-7), the kinetics for anodic and cathodic reactions are described respectively by:

$$i_a = i_{0,a} \frac{C^*_{Cr^{2+}}}{C^{ref}_{Cr^{2+}}} \exp\left[\frac{(1-\alpha_a)n_1 F}{RT}(\eta_a)\right] \qquad \text{3-8}$$

$$i_c = i_{0,c} \frac{C^*_{Cr^{3+}}}{C^{ref}_{Cr^{3+}}} \exp\left[\frac{-\alpha_c n_c F}{RT}(\eta_c)\right] \qquad \text{3-9}$$

$$\eta = E - E^{eq} \qquad \text{3-10}$$

where subscripts a and c refer to oxidation and reduction reactions, respectively, i is the current density, η is overpotential, E is surface potential, E^{eq} is equilibrium potential, and i_0 is exchange current density. C^*_i is the concentration of species i adjacent to the surface. The concentration reaction expressions has been assumed to be first order as the experimental results showed a linear increase in the corrosion rate with chromium species in the salt. The equilibrium potentials of the oxidation and reduction reactions are determined by Nernst equations:

$$E_a^{eq} = E_a^0 - \frac{RT}{n_a F} \ln(C_{Cr^{2+}}) \qquad \text{3-11}$$

$$E_c^{eq} = E_c^0 - \frac{RT}{n_c F} \ln\left(\frac{C_{Cr^{3+}}}{C_{Cr^{2+}}}\right) \qquad \text{3-12}$$

where C_i is the concentration of species i in the bulk, and E_a^0 and E_c^0 are the anodic and cathodic standard potential vs Li/LiCl, calculated from the standard Gibbs energy of each corrosion product. The calculated E^0 values which are functions of temperature for oxidation and reduction reactions are shown in Table 3.2, respectively [57]. These potentials assume all species have an activity of 1 and the potentials are referenced with respect to the Li/LiCl reaction (LiCl + e⁻ = Li+ Cl⁻). The Li/LiCl reaction was chosen as a reference for the molten salt potentials since there is less variation with temperature when compared to using the hydrogen electrode.

The corrosion potential is calculated by applying the mixed-potential theory. The convention that anodic current densities are positive and cathodic current densities are negative has been applied [59].

$$-i_c = i_a = i_{corr} \qquad\qquad 3\text{-}13$$

Table 3.2. Standard potentials for main corrosion reactions of Haynes 230 in KCl-MgCl$_2$ as inputs to the model [57].

Electrochemical reactions	Temperature (K)	E (V) vs Li/LiCl
CrCl$_2$ + 2e$^-$ = Cr + 2Cl$^-$	T ≤ 900	$E^0 = -0.0002T + 2.198$
	900 < T ≤ 1150	$E^0 = -0.0001T + 2.112$
	1150 < T	$E^0 = -0.0004T + 2.485$
CrCl$_2$ + Cl$^-$ = CrCl$_3$ + e$^-$	T ≤ 900	$E^0 = 0.0002T + 2.561$
	850 < T ≤ 1150	$E^0 = 0.0004T + 2.438$
	1150 < T	$E^0 = 0.0001T + 2.729$

Once the corrosion potential is obtained by solving Equation 3-13, the corrosion current density is also computed.

Kinetic parameters were obtained from fitting the values to the polarization data at the isothermal conditions (i.e., 750 °C, 850 °C, and 950 °C) under condition that $\frac{\varepsilon^{1.5}}{\delta}$ is small (i.e., 0.16 (m^{-1})) where the kinetic effects are dominant and mass transfer effects can be neglected. The parameters then can be used for non-isothermal conditions where both kinetic and mass transfer effects are important. Kinetic parameters that were put in to the model are listed in Table 3.3 (i.e., the calculations are shown in Appendix B).

Table 3.3. Kinetic parameters used for the prediction of Haynes 230 corrosion in KCl-$MgCl_2$ salt as inputs to the model.

Electrochemical reactions	Temperature T (°C)	Kinetic parameters		
		i_0 (A cm^{-2})	$\alpha_{a,c}$ [60]	n
$CrCl_2 + 2e^- = Cr + 2Cl^-$	750	2.9×10^{-5}	0.5	2
$CrCl_2 + Cl^- = CrCl_3 + e^-$		4.9×10^{-7}	0.5	1
$CrCl_2 + 2e^- = Cr + 2Cl^-$	850	2.3×10^{-4}	0.5	2
$CrCl_2 + Cl^- = CrCl_3 + e^-$		1.6×10^{-6}	0.5	1
$CrCl_2 + 2e^- = Cr + 2Cl^-$	950	1.5×10^{-3}	0.5	2
$CrCl_2 + Cl^- = CrCl_3 + e^-$		4.8×10^{-6}	0.5	1

3.3.3 Transport of ionic species

As evidenced by the SEM results and the energy dispersive X-ray spectroscopy (EDS) mapping, there is a layer near the surface of the alloy which is hundreds of microns thick that participates in the corrosion reaction. Experiments have showed that the selective depletion of Cr in this layer forms a porous microstructure that is open to the salt (see Figure 3-3). This can be concluded from the X-ray maps of the cross-section of the corroded alloy, which indicates a gradient in the metal concentration, showing that the metal diffuses out from this layer. The Cr depletion at this layer mostly occurred at the grain boundaries of the alloy [57]. The experimental data [57] for Haynes 230 showed a 64 micron average grain size which is proportional to the 0.1% of the volume fraction. From this evidence, the grain boundary layer at the surface of the alloy is assumed to be of a constant thickness of δ and acts as a porous layer and diffusion of the ionic species takes place in this region.

Cr^{3+}, as a result of disproportionation reaction of $CrCl_2$ at the Ni crucible (reactions 3-4 and 3-5) can diffuse through this porous layer to the surface of the alloy and Cr^{2+} ions can

diffuse back to the salt as products of oxidation\reduction reactions on the surface of the alloy (reactions 3-2 and 3-3). Figure 3-4 shows the cross-section of the coupon and the region prone to porous layer attack with thickness of δ (yellow region). The part of the coupon that was used as a connection to the Ni crucible and a Ni crucible insert was neglected to simplify the geometry. The diffusion of different species through this porous layer is shown schematically in Figure 3.4 as well.
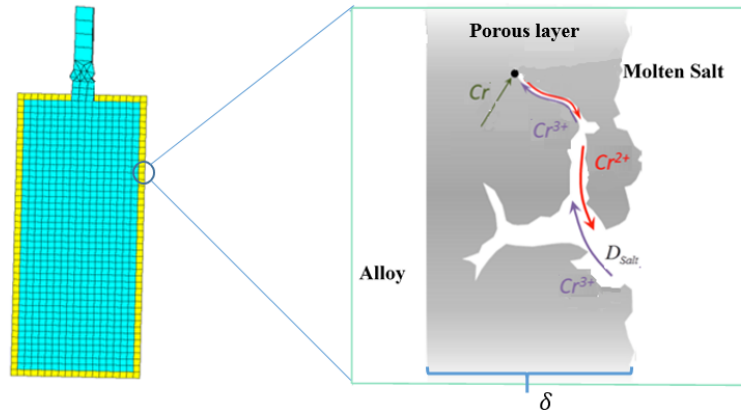
Figure 3.4. The coupon cross section by considering the area of the sample surface that is covered by grain boundaries.

The complete mass and momentum equations (Navier-Stokes flow) and heat equations were solved, with the inclusion of the gravity effect (i.e., the details described in our previous publication [57]). As a result, the concentrations of species (i.e., Cr^{3+} and Cr^{2+}) inside the salt are attained. Due to the small value of the diffusion coefficient, the concentration of species differs significantly from their bulk values at the surface of the alloy. In comparison to the bulk of the molten salt where both diffusion and convection are important, inside the porous layer, the velocity is small, and the diffusion is of primary importance to the transport process. In addition as explained by Newman et al [61] , for the

reactions of minor ionic species in the solution containing excess supporting electrolyte, it should be permissible to neglect the contribution of ionic migration to the flux of the reacting ions. As a result, the potential field equation in this study is neglected (i.e., the amount of Cr^{2+} and Cr^{3+} was at most 1000 ppm measured by ICP-AES which means this assumption is reasonable). So for the flux of ionic species i, inside the porous layer we have:

$$\mathbf{N}_i = -D_i^{eff}[\frac{\partial C_i}{\partial x}]c_{x=0} \qquad \text{3-14}$$

where D_i^{eff} is the effective diffusion coefficient of the species i that can be expressed as [62]:

$$D_i^{eff} = \frac{\varepsilon D_i}{\tau} \qquad \text{3-15}$$

D_i is the diffusion coefficient of species i in the salt, and the values of pre-exponential factor for D_i are listed in Table 3.4 [57]. In this paper the ε (porosity) is defined as the volume fraction of grain boundaries which is a function of grain boundary size [63] as discussed earlier. In the absence of information about the grain boundaries' tortuosity, it is taken to be inversely proportional to the square root of porosity, in an analogy with the theory of porous electrodes [64].

$$\tau = \varepsilon^{-0.5} \qquad \text{3-16}$$

Table 3.4. Pre-exponential factor for the diffusion coefficients of various species as inputs to the model: T [=] K

	Pre-exponential factor ($cm^2\,s^{-1}$)
Cr^{2+} in KCl-NaCl [57]	log D = -2.43 – 2118/T$\pm$0.03
Cr^{3+} in KCl-NaCl [57]	log D = -2.44 – 2294/T$\pm$0.03

A single reaction can be written in symbolic form as [65]:

$$n_j e^- \leftrightarrow \sum_{i=1}^{n} s_{i,j} S^{z_i} \qquad \text{3-17}$$

where $s_{i,j}$ is the stoichiometric coefficient and S is the ith species with a charge z_i and the sum is over all the species for a given reaction at one electrode. For any species, the influx at the surface can be determined from:

$$N_i = -\sum_{j=1}^{r} \frac{s_{i,j} i_j}{n_j F} \qquad \text{3-18}$$

The flux of ionic species of Cr^{2+} and Cr^{3+} at the surface of the alloy can be determined by:

$$\mathbf{N}_{Cr^{2+}} = \frac{i_a}{n_a F} - \frac{2 \, i_c}{n_c F} \qquad \text{3-19}$$

$$\mathbf{N}_{Cr^{3+}} = \frac{2 \, i_c}{n_c F} \qquad \text{3-20}$$

By considering Equation 3-13 and the equality of n_a and n_c, the equation 3-19 can be simplified as:

$$\mathbf{N}_{Cr^{2+}} = \frac{3 \, i_a}{n_a F} \qquad \text{3-21}$$

3.3.4 Numerical procedure

The numerical model is three-dimensional, steady state, and non-isothermal. The process of corrosion is in general a time dependent event, however since the time scale of the corrosion process is substantially larger than most other transport process, a quasi-steady state can be assumed [66]. The coupled heat, mass and momentum transfer of the flow inside the thermosiphon was solved by using a commercial CFD code STAR-CD

4.18. The detailed equations and boundary conditions have been described in our previous publication [57]. The total grid size of this model geometry is 208,033 hybrid grid cells consisting of structured and unstructured grids (i.e. Figure 3.2). The equations are solved by using the SIMPLE (Semi-Implicit Method for Pressure Linked Equations) algorithm and the calculations are carried out with double precision accuracy. The convergence criteria for the species transport for all residuals was set for less than 1×10^{-12}. In this paper, additional models have been developed for solving corrosion rates and corrosion potentials at the surface of the coupons (i.e., Equations 3-8 through 3-21). The additional models are incorporated via user defined function modules linked to the CFD code.

3.4 Results and Discussions

The local temperature in the thermosiphon is the main factor controlling the corrosion rates on the surface of the coupons because it directly influences the transport of chromium cations, the properties of the salt, and the kinetic parameters. The temperature boundary conditions on the wall surface correspond to the experimental setup parameters (i.e., Equations 3-1a and 3-1b) and using these boundary conditions, CFD calculations were performed to predict the thermal gradients inside the thermosiphon and at the surfaces of the coupons at both the top (cold zone) and the bottom (hot zone). The temperature profile calculation is discussed in detail in our previous study and is in good agreement with reported experimental data with only 1.0% error [57]. In this paper the calculations are carried out in the same temperature ranges of 650–800 ℃ and 800-950 ℃ [57]. Figures 3.5 (a) and 3.5 (b) show the temperature gradient at the surfaces of the coupons by applying Equations 3-1a and 3-1b as boundary conditions. The temperature distribution is fairly uniform around the coupons in both temperature ranges (i.e., 650–800 ℃ and 800-950 ℃).

Due to the temperature profiles, naturally convective flow occurs inside the thermosiphon where the flow moves from the cold zone to the hot zone (bottom) as a downward flow in the center tube. The localized regions close to the coupon surfaces have more mixing with fewer gradients compared to the side wall regions. In addition to the temperature profile Figures 3.5 (a) and 3.5 (b) show the velocity streamlines for temperature ranges of 650–800 ℃ and 800-950 ℃, respectively. The model predicted a small magnitude of flow moving around the coupons which is shown in Figures 3.5 (a) and 3.5 (b). By comparing the flow profiles of molten salt for the lower temperature range (650-800 ℃) with those of the higher temperature range, one finds that the differences in the flow profiles are caused by the variation of density at different points in the thermosiphon.

To study the effect of temperature on the corrosion rate, experiments were performed for the corrosion rates of Haynes 230 coupons in KCl-MgCl$_2$ for three different isothermal conditions and two different non-isothermal conditions with different temperature ranges and fluid flow. Table 3.5 shows the different operational conditions in addition to the corrosion rate predictions by model. The calculations were carried out in the temperature range of 600–950 ℃ for the non-isothermal, and 750 ℃, 850 ℃, and 950 ℃ for the isothermal conditions. By comparing the corrosion currents and potentials for different isothermal temperatures conditions, it can be concluded that the model shows higher corrosion rates and potentials with increasing temperature. Figures 3.6 (a) and 3.6 (b) show these effects respectively and compare the model with experimental results. The predicted average corrosion currents and corrosion potentials agree reasonably well with experimental data by less than 10% difference.

47

The effect of temperature gradient on the corrosion rate at the surface of the coupons for non-isothermal conditions are shown in Figure 3.7. Figures 3.7 (a) and 3.7 (b) show the influence of temperature on the corrosion rate occurring at the surface of the coupons for the temperature range of 650–800 ℃ and 800-950 ℃ inside the thermosiphon, respectively.

The comparison of predicted corrosion current densities for both cold zone and hot zone (bottom) inside the non-isothermal thermosiphon shows higher corrosion rates than the rates shown in isothermal conditions for similar average reactor temperatures. Therefore, thermally driven fluid flow accelerates the corrosion rates. Since the flow velocity governs the Cr^{3+} concentration on the alloy surface, the corrosion rate increases. As expected, the corrosion rate is higher in the hot zone of the reactor. Comparisons of the experimental and predicted local corrosion rates for Haynes 230 coupons in KCl-MgCl₂ for the thermosiphon at 800-950 ℃ are shown in Table 3.6. The conditions that are chosen for corrosion rate calculations are also listed in Table 3.7.

Figure 3.8 shows the effect of the porosity (volume fraction) on the system corrosion distribution for the temperature range of 800-950 ℃. Selective depletion of Cr forms a porous microstructure layer at the surface of the alloy. The volume fraction of this surface for Haynes 230 is around 0.1% [62].
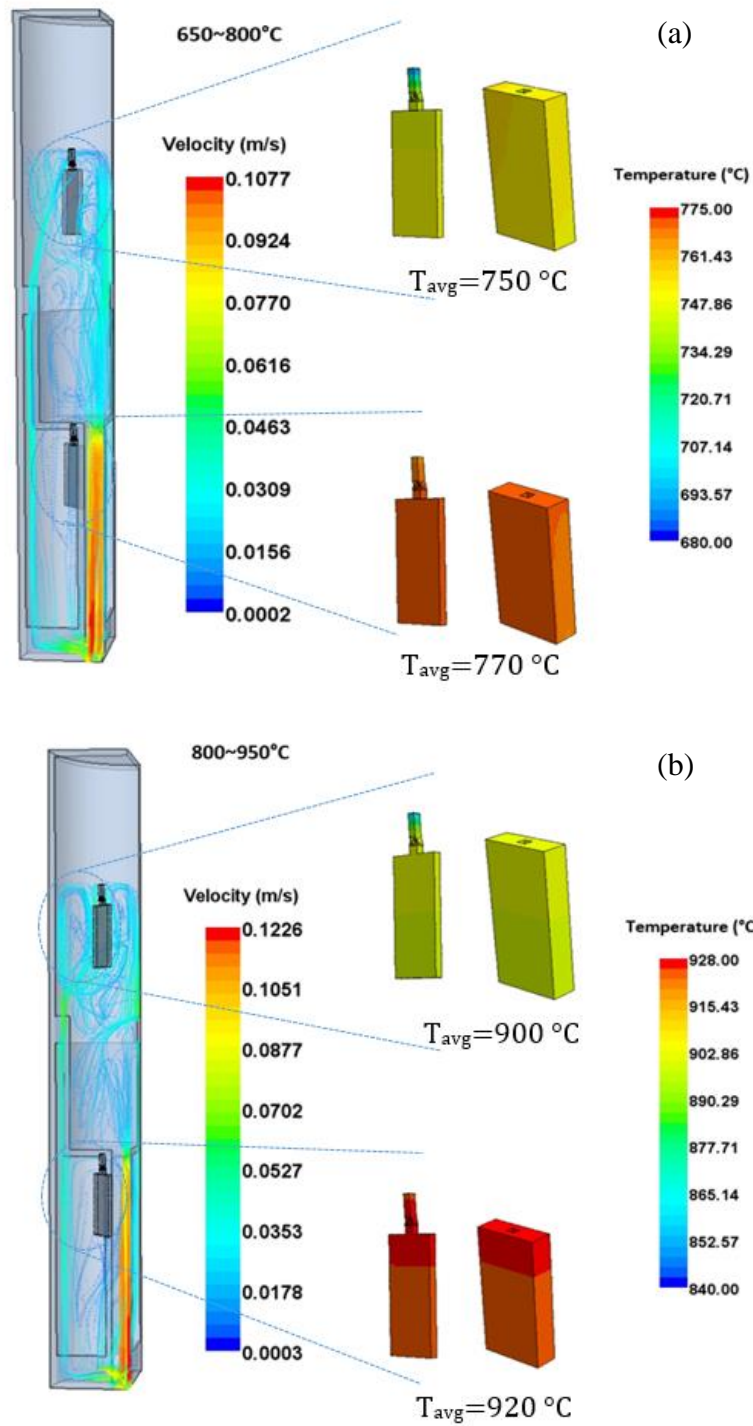
Figure 3.5. Distributions of velocity streamline of the thermosiphon and temperature distributions at the surface and around the coupons (a) at 650-800 °C and (b) at 800-950 °C.
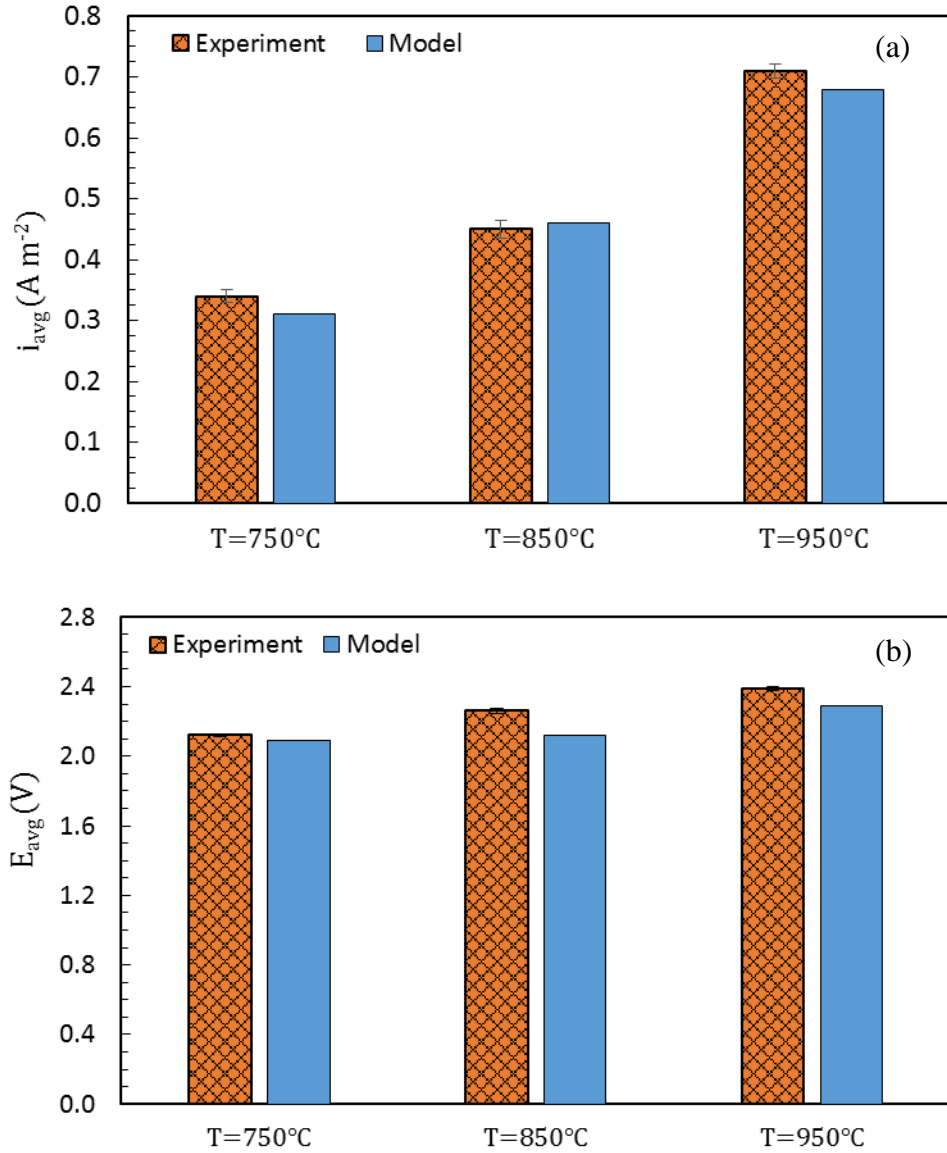
Figure 3.6. Prediction of average corrosion rate (current density) (Am^{-2}) (a) and average corrosion potential (V) (b) for Haynes 230 coupons for stagnant conditions at three different temperature.

Table 3.5. Comparison of corrosion rates for Haynes 230 in KCl-MgCl$_2$ at different operational conditions.

Temperature [°C]	Average (°C)	Predictions i_{avg} (A m^{-2})
750	750	0.31
850	850	0.46
950	950	0.68
690-800 (Cold zone)	738	1.27
690-800 (Hot zone)	760	1.34
800-950 (Cold zone)	908	1.82
800-950 (Hot zone)	926	2.18

Table 3.6. Comparison of corrosion rates for Haynes 230 in KCl-MgCl$_2$ with experimental data at 800-950 ℃.

i_{avg} (A m^{-2})	Cold zone	Hot zone
Model prediction	1.70	2.18
Experiment	1.82	2.20
Error%	6.0	1.0

Table 3.7. Parameters used for the prediction of Haynes 230 corrosion in KCl-MgCl$_2$ salt as inputs to the model for thermosiphon at 650-800 ℃ and 800-950 ℃.

Parameters	Cold zone	Hot zone
δ (μm)	50	50
ε (%)	0.1	0.5
$Y_{Cr^{3+}}$	0.001	0.001
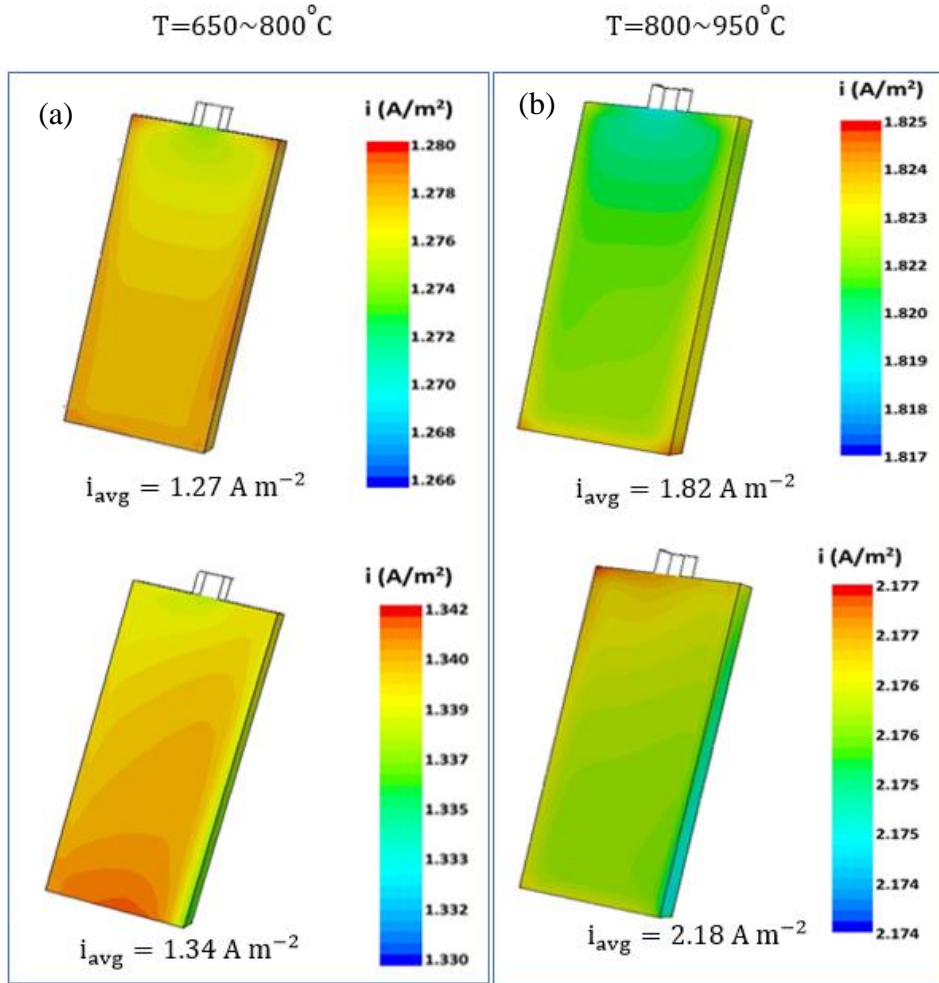
Figure 3.7. Prediction of local and average corrosion rate (current density) for Haynes 230 coupons in KCl-MgCl$_2$ with fluid flows (a) at 600-850 °C, (b) at 800-950 °C for both cold zone and hot zone.

As selective depletion of Cr at this layer causes the increase in porosity, three different porosities of 0.1, 0.3 and 0.5 percent were chosen for comparison. The results show almost uniform distribution of corrosion at the surface of the coupons with slightly higher corrosion rates at the edges rather than in the middle part for all cases. This is due to the fact that the corrosion rate distribution is influenced by the temperature gradient and fluid flow around the coupons. Figure 3.5 shows the temperature distribution is very uniform and the flow moving around the coupons has a small magnitude of 10^{-3} ms^{-1} [57]. Figure

3.8 shows that lower porosity, which naturally corresponds to a lower area of the alloy exposed to the molten salt, gives a lower corrosion rate. As the pores are interconnected and open to the environment, lower porosity hinders diffusion of species toward and away from the surface and as a result the corrosion rate is reduced These results show that any possible changes in the grain boundary size or morphology that could increase the porosities from 0.1 to 0.5 percent could increase the average corrosion rate, by a factor of four.

Figure 3.9 shows the comparison of four different thicknesses of the porous layer. As described earlier, the corrosion happens in a layer of finite thickness at the surface of the coupons (i.e., the thickness can be changed from 8 μm to 270 μm for different alloys in contact with the molten salt [58]). In the model described, if the corrosion rate in this porous layer is to be calculated, the user has to specify this layer thickness. The volume fraction (porosity) of 0.5 percent was picked for the CFD run. The results show that the corrosion rate is decreased by increasing the thickness of the porous layer. As an example, increasing the thickness by 10 times reduces the corrosion rate by 6%. That is caused by the fact that a thicker layer has a higher corrosion resistance as the species should diffuse a longer distance to react with the alloy surface.

To better understanding of the effect of mass transfer parameters on the corrosion rate (i.e, porosity and the thickness of the porous layer), the parameter $\frac{\varepsilon^{1.5}}{\delta}$ has been defined. Figure 3.10 shows the effect of this parameter on the corrosion rate. The results show that increasing the parameter $\frac{\varepsilon^{1.5}}{\delta}$ from 0.16 (m^{-1}) to 1.77 (m^{-1}) can increase the corrosion rate by 10% at both the cold zone and the hot zone. These results showing increasing the diffusion of species at the surface of the coupons can accelerate the corrosion rate.
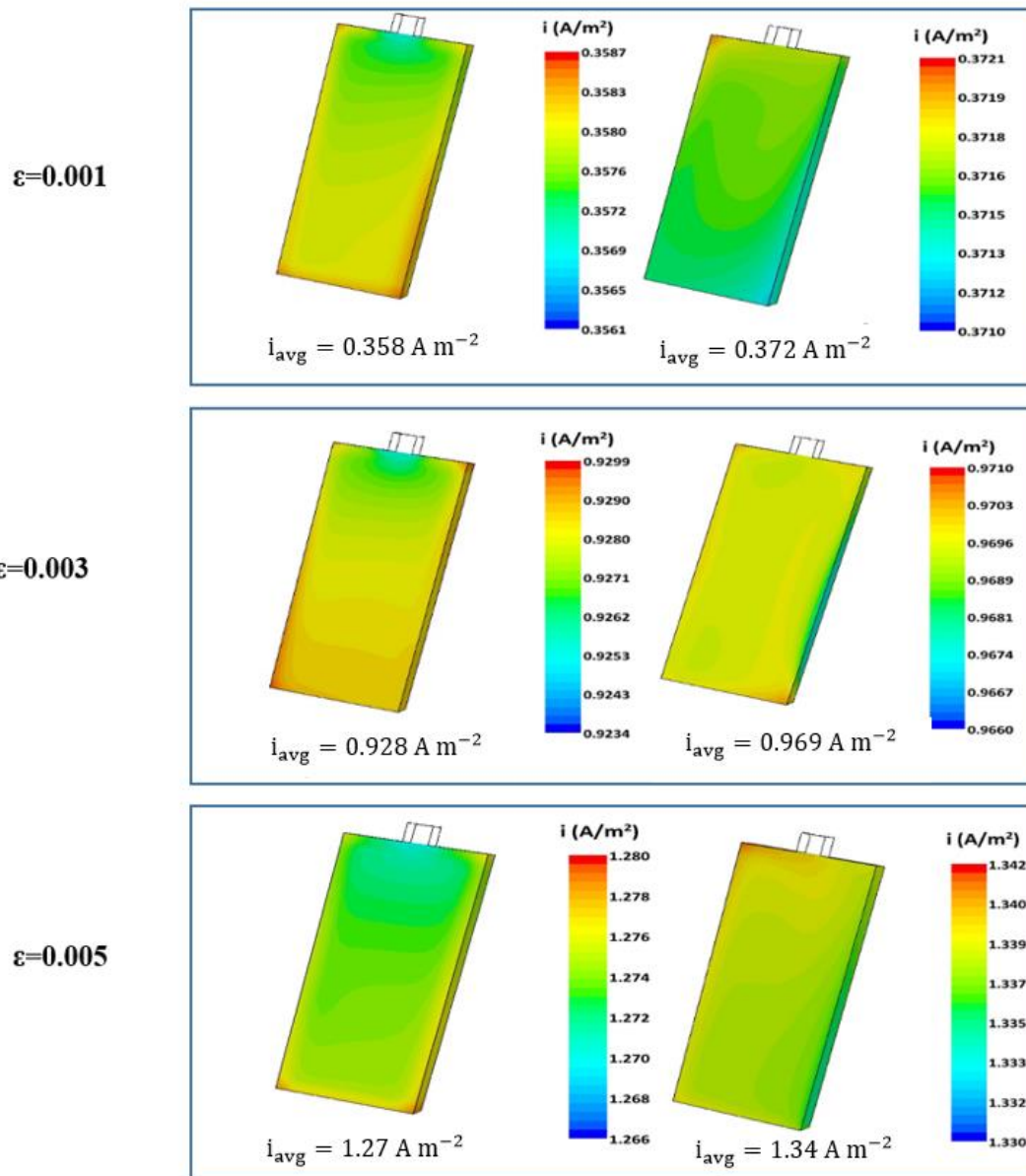
Figure 3.8. The comparison of the corrosion rate distribution at cold zone (left side) and hot zone (right side) for three different porosities at 800-950 ℃.
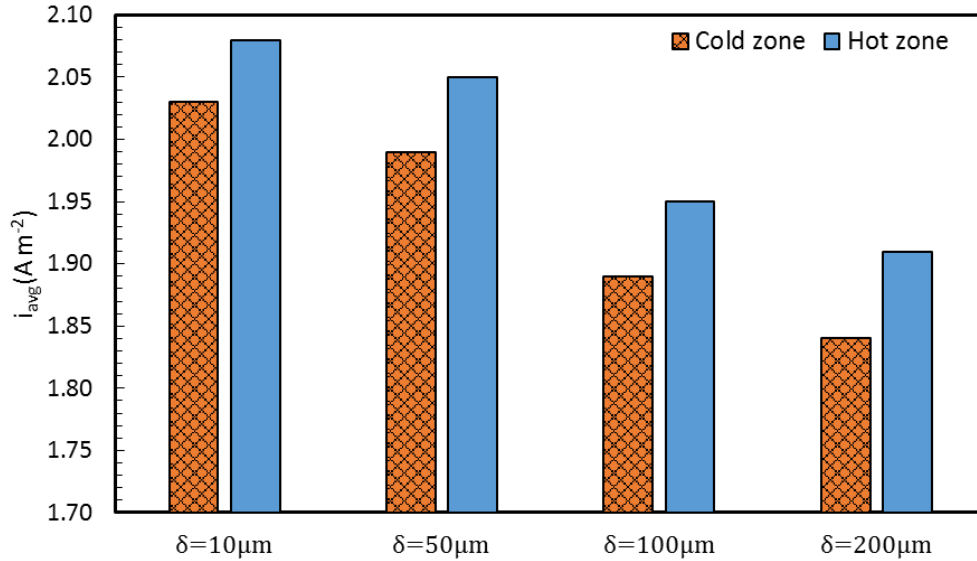
Figure 3.9. The comparison of the average corrosion rate at the coupon surfaces at both hot zone and cold zone for different porous layer thicknesses at 800-950 ℃.

As reactions 3-4 and 3-5 show, the creation of Cr^{3+} from the oxidation of Cr^{2+} creates an oxidizing agent that goes back to the alloy surface of the coupon and accelerates the Cr dissolution. Figure 3.11 shows the effect of different mass fractions of Cr^{3+} in the molten salt on the corrosion rate of the coupons at both hot and cold zones for the temperature range of 800-950 ℃. The corrosion rate is much higher for the case of larger Cr^{3+} concentration. As the concentration gradient of Cr^{3+} between the salt and the alloy surfaces increases, it can force more diffusion of species into the grain boundaries. These results are consistent with the experimental results provided by Wang et al. [53] that showed the presence of substantial concentrations of Cr^{3+} in the melt accelerates the dissolution of Cr from the alloy, and thus, accelerates corrosion. It is clear that reducing the impurity levels is imperative to reducing the corrosion of materials in molten chloride salts, which is consistent with the literature [67].
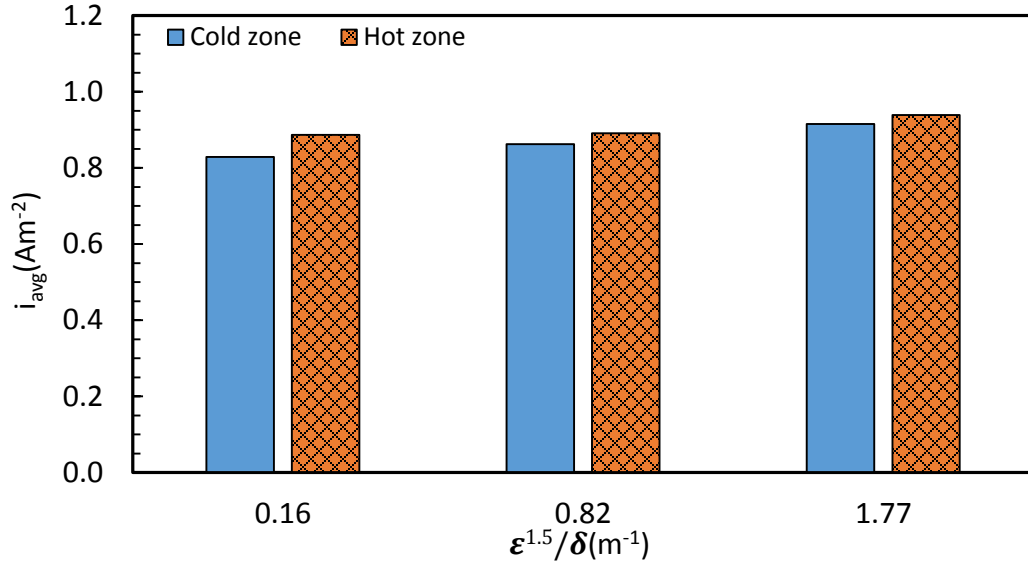
Figure 3.10. The comparison of the average corrosion rate at the coupon surfaces at both hot zone and cold zone for different $\frac{\varepsilon^{1.5}}{\delta}$ (m^{-1}) at 800-950°C.
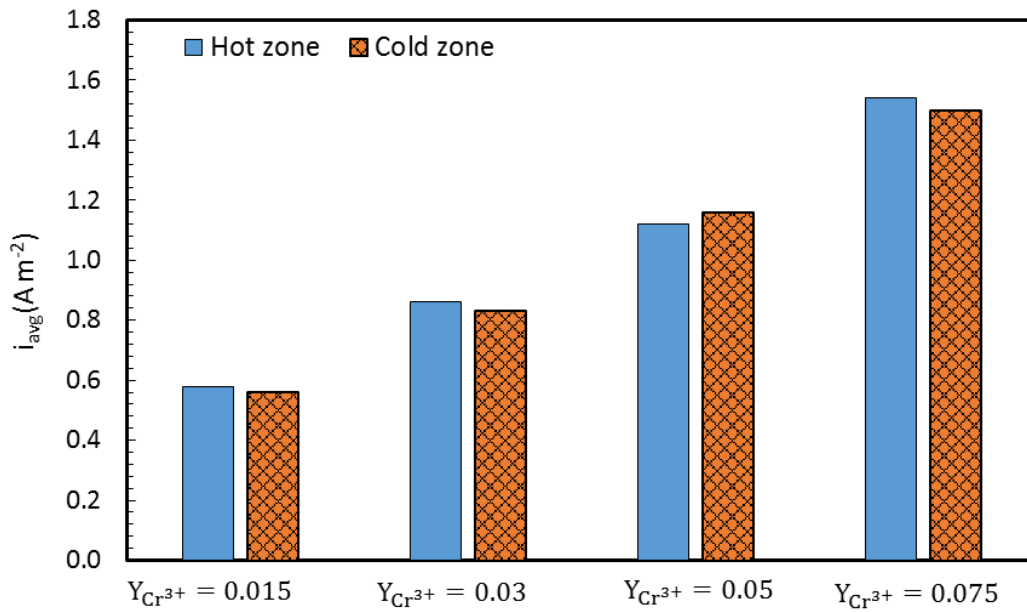
Figure 3.11. The comparison of the average corrosion rate at the coupon surfaces at both hot zone and cold zone for different Cr^{3+} mass fraction at 800-950°C.

3.5 Summary

A steady state 3D model has been developed which accounts for the corrosion mechanisms of nickel-based alloy in KCl-MgCl$_2$ with thermal gradients for concentrated solar power (CSP) systems. The model couples electrochemical kinetics with heat and mass transfer. It considers the effect of the critical corrosion parameters on the corrosion rate (e.g. temperature, grain boundaries properties) and can calculate the distribution of the corrosion rates at the surface of the coupons at the high temperature conditions of the CSP. The corrosion rates obtained by the model are in good agreement with experimental results with less than a 5% difference. The results reveal that temperature has an important effect on the corrosion rate of nickel-based alloys in molten salt. For the case with the higher temperature range 800-950 ℃, the corrosion rate is almost twice that of the case with the low temperature range 650-800 ℃. For all of the cases of non-isothermal conditions similar corrosion rates are predicted for both coupons at the hot and cold zones with slightly higher corrosion rates in the hot zone, and with slightly higher corrosion rates at the edges of the coupons for both cases. It was also shown that the porosity and thickness of the porous layer has an effect on the corrosion rate as it can influence the species diffusivity. Another important factor is the concentration of Cr^{3+}, the concentration affects the mass transfer rate which can in turn affect the corrosion rate of the system. The model is capable of considering the effects of kinetic and mass transfer on the corrosion rate under high-temperature fluid flow systems.

CHAPTER 4. MODELING THE EFFECT OF CATHODIC PROTECTION ON HIGH-TEMPERATURE ALLOYS INSIDE HIGH TEMPERATURE MOLTEN SALT SYSTEMS

One way to potentially reduce the costs of concentrated solar power (CSP) systems is to operate the central receiver at high temperatures which allow for more efficient thermodynamic power conversion cycles. Molten salts are one potential heat transfer fluid that can operate efficiently at these temperatures, but their use will introduce other technological challenges, such as corrosion reactions. The corrosion of alloys at high-temperatures (700-1000°C) in the receivers and heat exchangers cause a reduction in the heat transfer efficiency and durability of the alloy. Cathodic protection may mitigate corrosion of metal surfaces by shifting the potential of the alloy below its oxidation potential. The behavior of molten salt concentrated solar power (CSP) systems under cathodic protection can be obtained by developing a 3D model. A corrosion model was designed for and benchmarked against a thermosiphon reactor. This thermosiphon reactor exposed the alloy coupons to isothermal and non-isothermal conditions expected in concentrated solar power (CSP) plants. The model compared the corrosion rates for the cases with and without cathodic protection.

For the cathodic protection case Magnesium (Mg) was added to the salt which changed the potential from the natural corrosion potential (E_{corr}) to a protective potential in the

immunity region, then the model calculated the corrosion rate at the surface of the coupons. Results were in good agreement with experimental values for the runs with and without the cathodic protection and at isothermal and non-isothermal conditions with less than 3% difference.

4.1 Introduction

Concentrated solar power (CSP) plants are considered one of the best candidates for providing the majority of renewable energy by converting sunlight to heat as an intermediate step to generate electricity [68]. In these systems molten salts, specifically molten halides, are widely applied as the heat transfer medium due to their good thermal conductivity, large specific heat, low melting point, and relatively good chemical inertness [47, 48]. However, the molten halide salts are highly corrosive, especially at high temperatures (700-1000 °C) [54]. Although super-alloys have been developed for high-temperature applications, they are not able to meet both the high-temperature strength and the high temperature corrosion resistance simultaneously. To increase the lifetime operation of the system, it is of utmost importance to prevent the corrosion of the super-alloys in contact with molten salts. One of the most commonly used methods of retarding corrosion and extending the life of the structure is cathodic protection.

Cathodic protection is a well-known method to prevent the corrosion of the alloy at aqueous solution by shifting the potential of the alloy to the least probable range for corrosion [69]. However, cathodic protection has rarely been applied at high-temperature molten salt systems. The only example thus far has been in the nuclear industry, where reactor materials were protected from the attack of fluoride salts. Matson et.al [39]

59

developed the experiments to determine the feasibility of using cathodic protection to reduce the attack in the fluoride volatility process for recovery of nuclear fuel at 650 °C. Their results show that CP would reduce the corrosion of submerged Inor-8 components in fused fluoride salt systems by a factor of 10. Recent studies by Garcia-Diaz et al. [1] showed that metallic Mg can use as a corrosion inhibitor for the KCl-MgCl$_2$ molten salt systems at high operational temperatures (700-1000 °C).

As evidenced by recent experimental studies [40, 53, 54], for super-alloys the principle corrosion mechanism at high-temperature molten salt systems is the selective oxidation of Cr that occurs preferentially at the surface of the alloys along the grain boundaries.. Adding the cathodic species to the system such as Mg can hold the redox potential of the salt at a point where Cr dissolution from super-alloys into the molten salt and transport of Cr from the alloys is suppressed [1]. This would result in the corrosion rate distribution at the surface of the alloys be a function of the corrosion environment, ionic diffusivity in the salt, and the reaction kinetics at the metal-salt interfaces. In addition, the effect of environmental conditions on these processes should be taken into account, including the temperature gradient and fluid flow.

A modeling approach can help to identify the relationship between these processes and the performance of cathodic protection in molten salt systems. Numerical techniques that incorporate the nonlinear boundary conditions can describe the reaction kinetics and provide the reliable estimation of corrosion rate at the surface of the alloys under cathodic protection. In this study, a corrosion model was developed that considers the cathodic protection of super-alloys Haynes-230, Haynes NS-163, and Incoloy 800H under the realistic conditions of CSP plants. The model is based on experimental coupon studies

which were conducted between 700-1000°C within KCl-MgCl$_2$ molten salt in a thermosiphon reactor that was designed previously [57, 70] to allow exposure of the coupons to the isothermal and non-isothermal conditions. The model was developed to predict the corrosion rates associated with cathodic protection in non-isothermal systems with fluid flow and heat transfer, which is coupled to a computational fluid dynamic (CFD) component to calculate the temperature gradient and fluid flow. The Mg cathodic protection of super-alloys in KCl-MgCl$_2$ salt was considered because of their interest in use in CSP plants [1]. It is expected from the thermodynamic equilibrium potentials of the metals that the corrosion potential of the samples in contact with Mg will have a lower corrosion potential than samples that have no contact with Mg. This indicates that the Mg is working to decrease the corrosion potential of the sample and, as a result, the corrosion current. The polarization method was used to determine the corrosion potential and the corrosion current. The rate of Mg consumption, the corrosion potential, and the corrosion current are dependent on several studied variables such as temperature, fluid flow, Mg concentration, and the alloy's grain boundaries, which are all examined in detail in this work.

4.2 Model Development

4.2.1 Model Geometry

Figure 4.1 shows a sketch of a thermosiphon reactor that was designed for the experimental set up. Due to the temperature gradient in the system the upper and lower portions of the thermosiphon are designated as the cold and hot zone, respectively. The thermosiphon contains four coupons at the bottom and four coupons at the top. The

61

temperature boundary conditions were put into the model according to the temperature gradients were attained by inserting the thermosiphon into a furnace, as described before [57, 71]. The geometry mesh that represents the experimental system of the thermosiphon was created by using CATIA® and HyperMesh® software. Since the model geometry and computational mesh has been reported in detail in our previous publication [57], they will only be briefly discussed here. The computational domain of the thermosiphon is shown in Figure 4.1 (a) which is composed of: Ni crucible, Ni crucible insert, super-alloys coupons (which are located at the top and bottom of the thermosiphon, and eutectic KCl-MgCl$_2$ salt. The cross section of the coupon is shown in Figure 4.1 (b). Figure 4.1 (c) shows the thin layer at the surface of the coupon where the electrochemical reactions happen. The cylindrical geometry and symmetry in the thermosiphon design allows simplification of the computational domain when performing CFD. Symmetric boundary conditions were applied to a 90° section of the model for the CFD study. The total grid size of this model geometry is composed of 208,033 hybrid grid cells made up of structured and unstructured grids. For cathodic protection case, different amounts of Mg from 0 to 1.15 mol% considered in KCl-MgCl$_2$ as it has a non-negligible solubility in KCl-MgCl$_2$. Table 3.1 is showing the KCl-MgCl$_2$ properties that were used for the model prediction.

4.2.2 Governing Equations

Our previous study [57] showed that immersing Haynes 230 in KCl-MgCl$_2$ salt for 100 hours at 850℃ had caused Cr depletion at the surface and along the grain boundaries. Cr is selectively attacked in alloys immersed in molten chlorides by oxidation of Cr at the alloy surface, followed by dissolution of the chloride from the alloy surface into the salt. The electrochemical oxidation and reduction reactions for Haynes 230, Haynes NS-163,

and Incoloy 800H in the KCl-MgCl$_2$ salt are assumed to be a chromium oxidation reaction and CrCl$_3$ reduction reaction as explained in detail before [57].

$$\text{Oxidation reaction: } Cr + 2Cl^- \rightarrow CrCl_2 + 2e^- \qquad\qquad 4\text{-}1$$

$$\text{Reduction reaction: } 2CrCl_3 + 2e^- \rightarrow 2CrCl_2 + 2Cl^- \qquad\qquad 4\text{-}2$$
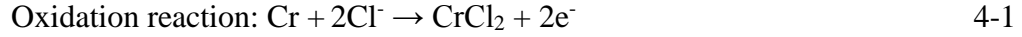
By introducing the magnesium (Mg) species in the salt solution in this work, an undesirable reaction of oxidation of chromium (i.e. reaction 4-1) is replaced by a more desirable reaction of oxidation of Mg (i.e. reaction 4-3). As by using Mg, all other metals that are more noble (higher reduction potential than Mg) will tend to stay in the metallic state until all Mg is oxidized. The new oxidation and reduction reaction that were introduced to the system are:

$$\text{Oxidation reaction: } Mg + 2Cl^- \rightarrow MgCl_2 + 2e^- \qquad\qquad 4\text{-}3$$

$$\text{Reduction reaction: } 2CrCl_3 + 2e^- \rightarrow 2CrCl_2 + 2Cl^- \qquad\qquad 4\text{-}4$$
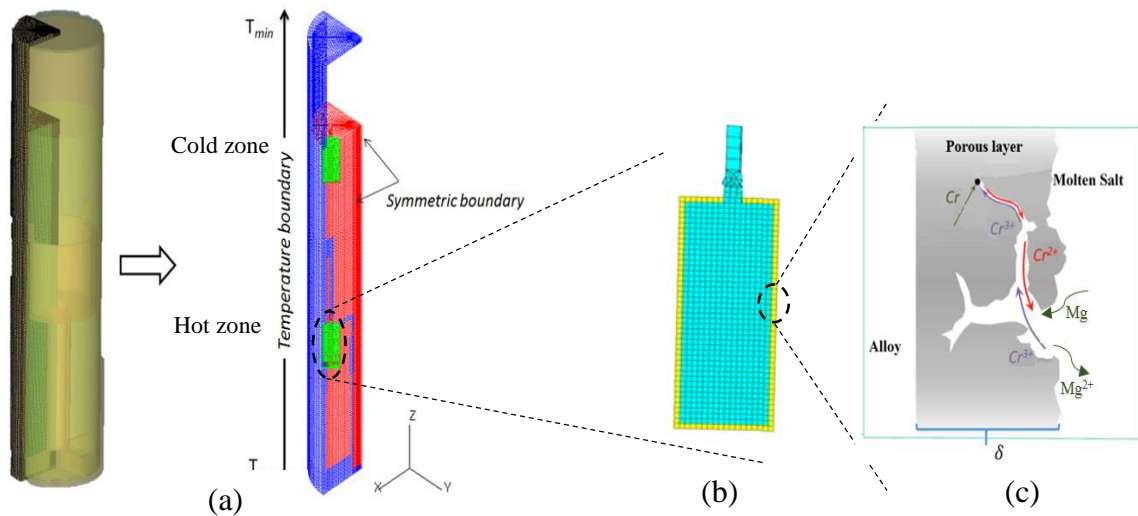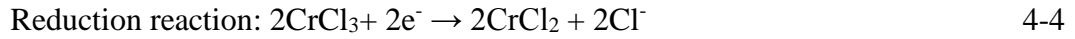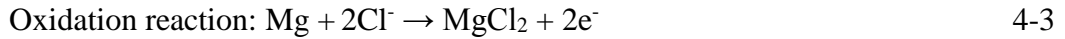
Figure 4.1. (a) The model geometry of the thermosiphon consists of a Ni crucible, a Ni crucible insert (blue), coupons (green) and the molten salt , (b) The coupon cross section (c) considering the area of the sample surface that is considered as porous layer [57].

It is expected from the thermodynamic equilibrium potentials of the metals that the corrosion potential of samples in contact with Mg will have a lower corrosion potential than the samples that have no contact with Mg. This indicates that the Mg is working to decrease the corrosion potential of the sample and as a result the corrosion current [40]. The polarization method was used to determine the corrosion potential and corrosion current without Mg and with Mg. An Evans diagram (Figure 4.2) was constructed for Haynes 230 in KCl-MgCl$_2$ with and without Mg as an example by using such parameters as Tafel slopes, exchange current densities, and equilibrium potentials to describe the electrochemical corrosion system virtually. The parameters that were used are shown in Table 4.1.

The construction of the Evans diagram allows for predictions and explanations of the effects that were observed experimentally. Figure 4.2 shows that for Cr oxidation reaction and CrCl$_3$ reduction reaction of Haynes 230 in KCl-MgCl$_2$ (i.e., without Mg), the corrosion current, i''_{corr}, and the corrosion potential, E''_{corr} occur at the point of intersection of the oxidation and reduction curve (dotted line).

Adding Mg to the system caused the cathodic polarization of the structure, thereby controlling the kinetics of the reactions occurring on the metal-electrolyte interface. As shown in Figure 4.2, polarization of the oxidation reaction in a negative direction from the corrosion potential decreases the corrosion rate. Polarizing the system from E''_{corr} from reactions 4-1 and 4-2 to the sacrificial potential of E_{corr} from reactions 4-3 and 4-4 causes the corrosion current density to decrease from i''_{corr} from reactions 4-1 and 4-2 to a new smaller value of current density, i_{corr}. This Evans diagram applied for all of the cells at the surface of the coupons (i.e., Figure 4.1(b)).

64
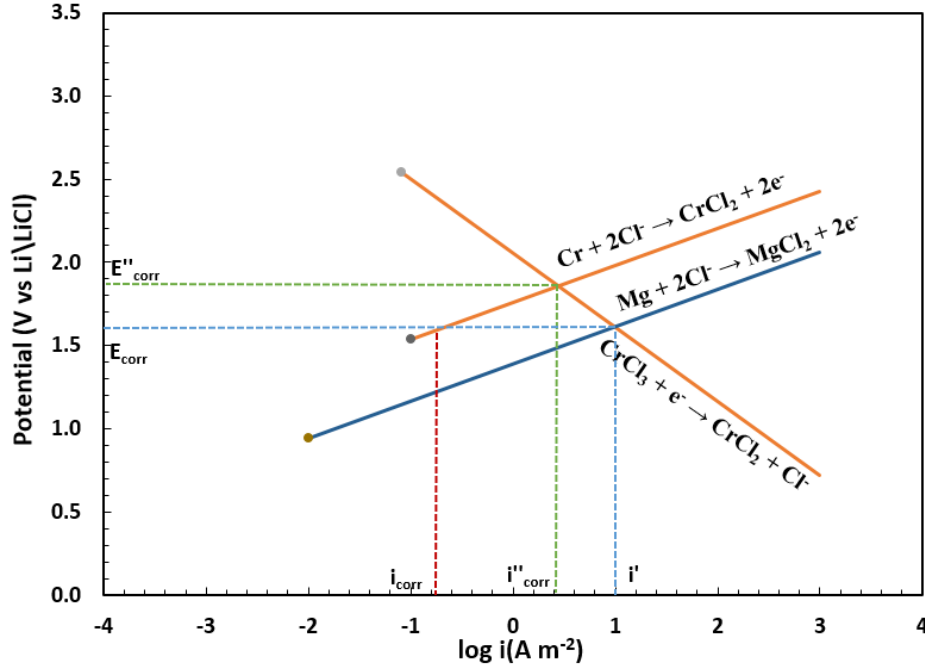
Figure 4.2. Evans diagram-principle of cathodic protection.

Table 4.1. Kinetic parameters used for the prediction of Haynes 230 corrosion in KCl-$MgCl_2$ salt as inputs to the model.

Electrochemical reactions	T (°C)	$\alpha_{a,c,a',c'}$ [60]	n	Kinetic parameters		
				Haynes 230 i_0 (A/cm²)	Haynes NS-163 i_0 (A/cm²)	Incoloy 800H i_0 (A/cm²)
$CrCl_2 + 2e^- = Cr + 2Cl^-$		0.5	2	3.5×10^{-4}	5.2×10^{-4}	4.9×10^{-4}
$CrCl_2 + Cl^- = CrCl_3 + e^-$	850	0.5	1	1.6×10^{-6}	1.8×10^{-6}	2.5×10^{-6}
$MgCl_2 + 2e^- = Mg + 2Cl^-$		0.5	2	5.5×10^{-6}	1.5×10^{-6}	8.5×10^{-7}

Introducing Mg to the system caused the Mg to oxidize to Mg^{2+} by reducing $CrCl_3$ to $CrCl_2$ (i.e., reactions 4-3 and 4-4) according to the experimental data. According to Butler-Volmer kinetics, in the present model, kinetics of these oxidation and reduction reactions (i.e. reactions 4-3 and 4-4) can be estimated from:

$$i_a = i_{0,a} \frac{C_{Mg}^*}{C_{Mg}^{ref}} \exp\left[\frac{(1-\alpha_a)n_a F}{RT}(\eta_a)\right] \tag{4-5}$$

65

$$i_c = -\, i_{0,c} \frac{C^*_{Cr^{3+}}}{C^{ref}_{Cr^{3+}}} \exp\left[\frac{-\alpha_c n_c F}{RT}(\eta_c)\right] \qquad \text{4-6}$$

$$\eta = E^{eq} - E \qquad \text{4-7}$$

where subscripts a and c refer to reactions 4-3 and 4-4 respectively, i is the current density, η is overpotential, E is surface potential, E^{eq} is equilibrium potential, and i_0 is the exchange current density. C^*_i is the concentration of species i adjacent to the surface. The equilibrium potentials of oxidation and reduction reactions are determined by the Nernst equation:

$$E^{eq}_a = E^0_a - \frac{RT}{n_a F}\ln\left(\frac{C_{Mg^{2+}}}{C_{Mg}}\right) \qquad \text{4-8}$$

$$E^{eq}_c = E^0_c - \frac{RT}{n_c F}\ln\left(\frac{C_{Cr^{3+}}}{C_{Cr^{2+}}}\right) \qquad \text{4-9}$$

where C_i is the concentration of species i in the bulk, and E^0_a and E^0_c are the oxidation and reduction standard potentials calculated from the standard Gibbs energy of each corrosion product. The calculated E^0 values which are functions of temperature for oxidation and reduction reactions are shown in Table 4.2, respectively. The calculated E^0 values versus Li/LiCl reaction (LiCl + e⁻ = Li+ Cl⁻) which are functions of temperature for oxidation and reduction reactions are shown in Table 4, respectively. The details of calculation have been described in our previous studies

Kinetic parameters were obtained from fitting the values to the polarization data at the isothermal condition (i.e., 850 °C) by considering $\frac{\varepsilon^{1.5}}{\delta}$ has a small amount (i.e., 0.16 (m⁻¹)) where the kinetic effects are dominant and mass transfer effects can be neglected. (i.e., the calculations are shown in Appendix B) so that mass transfer effects can be neglected. Variables that were input in to the model are listed in Table 4.1.

Mixed potential theory and kinetic equations were used to explain Mg dissolution. As a result of the reaction of Mg, an equilibrium state is established. The free corrosion condition for Mg requires the reactions 4-3 and 4-4 currents to be equal and opposite.

Where the convention that anodic current densities are positive and cathodic current densities are negative has been applied [59].

$$-i_c = i_a = i'$$ 4-10

Where i' is the reaction current (see Figure 4.2). Once the corrosion potential, E_{corr} for Mg reaction is obtained by solving Equation 4-10, the corrosion current density is also computed.

This reaction potential, E_{corr} can be applied for the Cr depletion reaction (i.e. reaction 4-2) at the surface of the alloy and allows us to be able to predict corrosion rate, i_{corr}, for the alloy in contact with molten salt.

$$i_{corr} = i_{0,a'} \frac{C^*_{Cr^{3+}}}{C^{ref}_{Cr^{3+}}} \exp\left[\frac{(1 - \alpha_{a'})n_{a'}F}{RT}(E^{eq}_{a'} - E_{corr})\right]$$ 4-11

Where subscripts a' refers to the Chromium depletion reaction (i.e. reaction 4-1) at the surface and along the grain boundaries. The reaction potential, E_{corr} is much lower than the corrosion potential that was calculated from reactions 4-1 and 4-2 (i.e., E''_{corr}) which causes the lower corrosion rate.

4.2.3 Transport of ionic species under cathodic protection

The experimental results from SEM and the energy dispersive X-ray spectroscopy (EDS) mapping without cathodic protection [57] showed the selective depletion of Cr in the alloy that formed a porous microstructure near the surface which is open to the salt (i.e.

Figure 4.1c). This can be concluded from the X-ray maps of the cross-section of the corroded alloy, which indicates a gradient in the metal concentration, showing that metal diffuses out from this layer. The Cr depletion at this layer mostly occurred at the grain boundaries of the alloy [57]. The grain boundaries layer at the surface of the alloy is assumed to be of a constant thickness of δ and acts as a porous layer with constant porosity of ε, that diffusion of the ionic species takes place in this region.

Table 4.2. Equilibrium potentials for main corrosion reactions of Haynes 230 in KCl-MgCl$_2$ as inputs to the model

Electrochemical reactions	Temperature ([K)	E (V)
$CrCl_2 + 2e^- = Cr + 2Cl^-$	$T \leq 900$	$E = -0.0002T + 2.198$
	$900 < T \leq 1150$	$E = -0.0001T + 2.112$
	$1150 < T$	$E = -0.0004T + 2.485$
$CrCl_2 + Cl^- = CrCl_3 + e^-$	$T \leq 900$	$E = 0.0002T + 2.561$
	$850 < T \leq 1150$	$E = 0.0004T + 2.438$
	$1150 < T$	$E = 0.0001T + 2.729$
$MgCl_2 + 2e^- = Mg + 2Cl^-$	$T \leq 900$	$E = -0.00006T + 0.927$
	$900 < T \leq 1000$	$E = 0.0002T + 0.703$
	$1000 < T$	$E = 0.00003T + 0.873$

For the case of cathodic protection, Mg and Mg^{2+} ions in addition to Cr^{3+} and Cr^{2+} can diffuse and diffuse back through this porous layer and react with Cr^{3+} ions at the surface. The flux of each dissolved species, through the electrolyte in the pores of the porous layer is given by:

$$\mathbf{N}_i = -D_i^{eff}[\frac{\partial C_i}{\partial x}]_{x=0} \qquad \text{4-12}$$

D_i^{eff} is the effective diffusion coefficient of species i that that can be expressed as [62]:

$$D_i^{eff} = \frac{\varepsilon D_i}{\tau} \qquad \text{4-13}$$

D_i is the diffusion coefficient of species i in the salt which is listed in Table 4.3. In this paper the ε (porosity) is defined as the volume fraction of grain boundaries which is a function of the grain boundary size [63]. In the absence of information of the grain boundaries' tortuosity, it is taken to be inversely proportional to the square root of porosity, in an analogy with the theory of porous electrodes [64].

$$\tau = \varepsilon^{-0.5} \tag{4-14}$$

The flux of ionic species at the surface of the alloy can be determine by:

$$N_{Mg^{2+}} = \frac{i_a}{n_a F} \tag{4-15}$$

$$N_{Mg} = \frac{-i_a}{n_a F} \tag{4-16}$$

$$N_{Cr^{2+}} = \frac{i_{a'}}{n_{a'} F} - \frac{2\,i_c}{n_c F} - \frac{2\,i_{c'}}{n_{c'} F} \tag{4-17}$$

$$N_{Cr^{3+}} = \frac{2\,i_{c'}}{n_{c'} F} + \frac{2\,i_c}{n_c F} \tag{4-18}$$

where subscripts a and c refer to reactions 4-1 and 4-2 and subscripts a′ and c′ refer to reactions 4-3 and 4-4 respectively.

4.2.4 Numerical Procedure

The numerical model is three-dimensional, steady state, and non-isothermal. The conservation of mass and energy along with the Navier-Stokes equations were all solved in the three-dimensional commercial CFD software, STAR-CD 4.18. The process of

69

corrosion is in general a time dependent event, however since the time scale of the corrosion process is substantially larger than most other transport process, a quasi- steady state can be assumed. The CFD code is modified to include the electrochemical corrosion reactions under cathodic protection. The additional models are incorporated via the user defined functions modules linked to the CFD code. This numerical model predicts the three-dimensional effect of heat transfer and fluid flow on the corrosion rates at the surface of the coupons under cathodic protection. The equations are solved by using the SIMPLE (Semi-Implicit Method for Pressure Linked Equations) algorithm and the calculations are carried out with double precision accuracy. The convergence criteria for the species transport were set for all residuals less than 1×10^{-12}. The detailed equations and boundary conditions have been described in our previous publication [57] and will not be repeated here in detail. Two different kinds of boundary conditions were applied for isothermal (850 ℃) and non-isothermal condition that are matched with the experimental measurements. For the non-isothermal case (T~800-950 ℃) there is a temperature gradient inside the thermosiphon which causes the temperature gradient around the coupons at the bottom to be different from the temperature around the coupons at the top. For convenience we called the upper and lower side of the thermosiphon, the cold and hot zones respectively, as are shown in Figure 4.1 (a).

4.3 Results and Discussions

4.3.1 Isothermal Conditions

For the study on the effect of Mg on the corrosion rate, experimental results were performed for the local corrosion rates of Haynes 230, Haynes NS-163, and Incoloy 800H coupons in KCl-MgCl$_2$ for 100 hours in isothermal condition of 850 °C without Mg and

with different concentrations of Mg. The results show that Haynes 230 has the lowest corrosion rate without cathodic protection and can be the best candidate for high temperature KCl-MgCl$_2$ molten salt system. Figures 4.3 (a), 4.3 (b), and 4.4 (c) compare the corrosion rates at the surface of the alloy with varying Mg content in the salt for Haynes 230, Haynes NS-163, and Incoloy 800H respectively. These results show that even by adding a small amount of Mg to the salt, the corrosion rate fell rapidly to a small value and then changed slowly as a function of Mg concentration. The experimental corrosion test results for the coupons in the salt were also obtained by a number of investigations and the results are also shown in Figures 4.3 (a)-4.3 (c). The results proved that the models calculated corrosion rate matches the experimental values with less than a 1% difference.

Figure 4.4 shows the corrosion rate predictions by the model at different temperatures for the isothermal case without Mg and with 1.15 mol% Mg for Haynes 230. The temperature of thermosiphon was varied between 650°C and 1050°C in the model while keeping constant all other parameters. The results show that increasing the salt temperature increases the corrosion rate for both cases with and without Mg. These results also show that adding the Mg to the salt caused significant reductions in the corrosion rates for all of the temperatures.

As discussed on previous chapter the creation of Cr^{3+} from the oxidation of Cr^{2+} at the surface of the Ni crucible creates an oxidizing agent that can diffuse to the alloy surface of the coupon and accelerates the Cr dissolution. Figure 4.6 shows the effect of different mol% of Cr^{3+} in the salt on the corrosion rate of the coupons for Haynes 230, Haynes NS-163, and Incoloy 800H at isothermal condition of 850°C. The linear relationship are shown in Figure 4.5 (a)-4.5 (c) between the amount of Cr^{3+} and the corrosion rate for all cases.

It is extremely evident that decreasing the amount of Cr^{3+} is imperative to decreasing the corrosion rate of materials in molten chloride salts. Although Cr^{3+} can diffuse through the porous layer, when there is Mg in the salt, the Cr^{3+} first is depleted due to cathodic protection reactions (i.e., reactions 4-3 and 4-4) and then the rest of Cr^{3+} consumed by the Cr in the alloy (i.e., reactions 4-1 and 4-2). The results also show that increasing the Cr^{3+} concentration causes a more rapid increase in the corrosion rate of Incoloy 800H when compared to Haynes 230 and Haynes NS-163 which is shown by experimental data.

4.3.2 Non-isothermal Condition

For the non-isothermal condition, the model's temperature distribution at the surface of the coupons and around the coupons for Haynes 230 are shown in Figure 4.6 (a) and 4.6 (b) for both cases without and with 1.15% Mg respectively. Figure 4.7 shows the temperature gradient for the case with Mg is slightly higher than the case without Mg. The average temperature around the coupons for the hot and cold zones respectively are 905.5 °C and 926.5 °C for the case of without Mg, and are 911.5 °C and 929.6 °C for the case of with Mg. This difference is due to the fact that the physical properties of the $KCl-MgCl_2$ salt have changed by adding Mg to the salt. From the experimental results the change in density and viscosity of salt mixture was negligible, but significant increase in thermal conductivity of the salt mixture was observed with addition of just 1% Mg (i.e., Table 4.1). The data showed that the thermal conductivity of $KCl-MgCl_2$ salt increased with increasing the amount of Mg linearly.

This increase is mainly because of the thermal conductivity of Mg which is much greater than that of $KCl-MgCl_2$ salt. Addition of Mg to the $MgCl_2$ salt promotes the thermal conductivity and as a result the average temperature at the surface of the coupons. Figure

72

4.7 shows the corrosion current density distribution at the coupon surfaces without and with 1.15 mol% Mg introduced into the salt for the non-isothermal condition. The average corrosion rate and corrosion potential are also shown in Figure 4.8. The overall results show that after introducing Mg into the salt solution, the corrosion current and corrosion potential were reduced around 99% and 20% respectively. The local distribution of corrosion current looks more uniform with the addition of Mg from the case without Mg. This could be because of the effect of mass transfer of ionic species in the porous layer which is more important for the case without Mg, as in that case the corrosion rate is influenced more by the temperature gradient and fluid flow rather than just kinetic parameters as the case with Mg.

The effect of Mg concentrations in the salt on the corrosion rate at the surface of the coupons for non-isothermal case of Haynes 230 are also considered. The results in Figure 4.8 shows that for this case like the isothermal case (i.e. Figure 4.3) adding even small amounts of Mg reduces the corrosion rate significantly. This reduction is seen at both the cold and hot zones. In this case there is a convective flow moving inside the thermosiphon. More rapid movement of the solution causes Mg to be brought into the metal surface at an increased rate. As a result the rate of Mg reactions are increased (i.e. Reactions 4-3 and 4-4) which causes more reduction in corrosion rate in comparison to the isothermal case.

For the non-isothermal condition, the distribution of corrosion rates at the surface of the coupons for Haynes 230 for different porous layer porosity are shown in Figure 4.9. The results show that there is almost a uniform distribution of corrosion rates at the surface for all cases. The comparison of corrosion rate for different porosity for the cases without Mg and with 1.15% Mg are also showed in Figures 4.10 (a) and 4.10 (b) respectively.
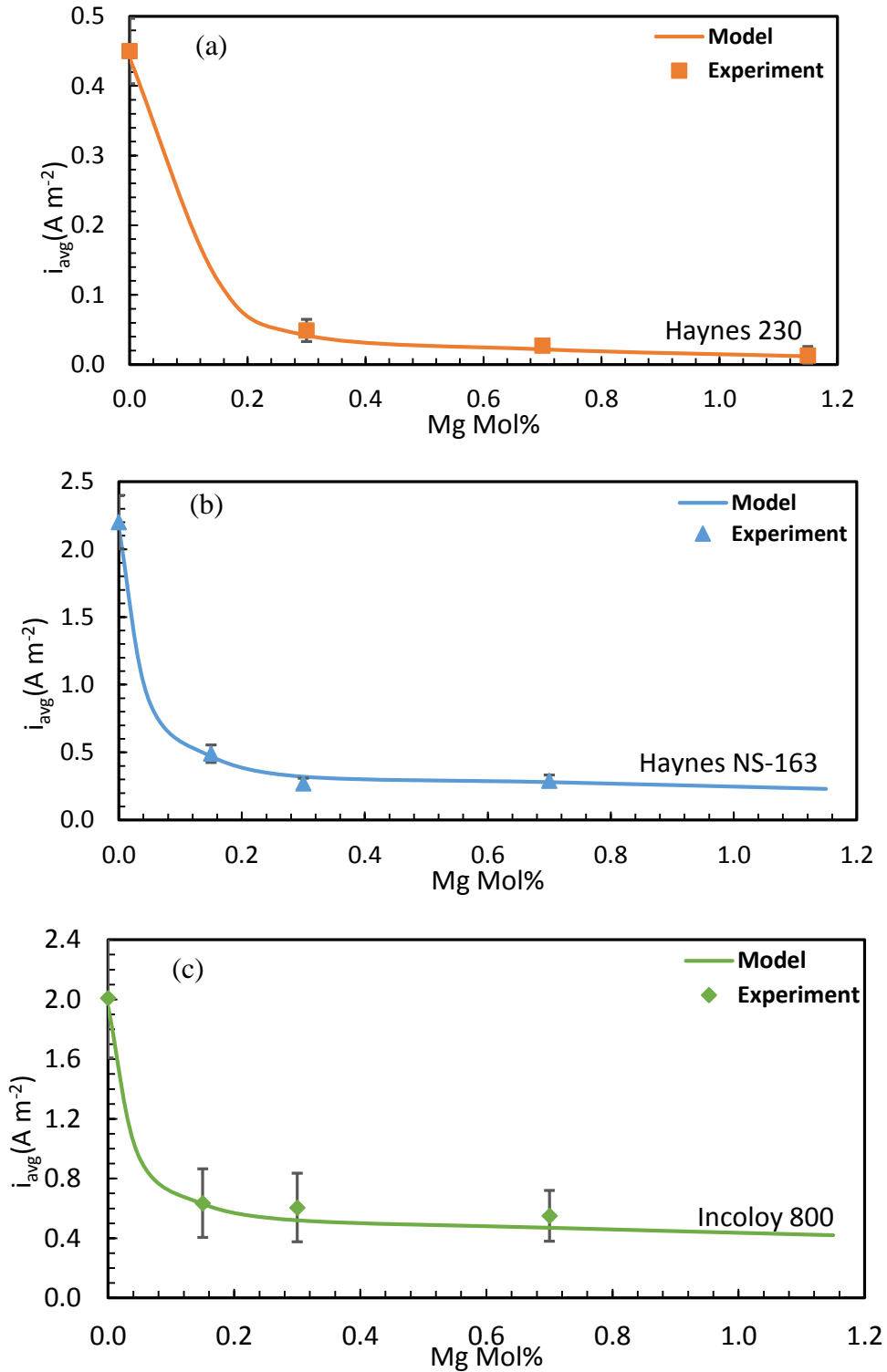
Figure 4.3. The comparison of corrosion rates at the surface of the alloy with varying Mg content in the salt for isothermal condition 850 °C (a) Haynes 230, (b) Haynes NS-163, and (c) Incoloy 800H.
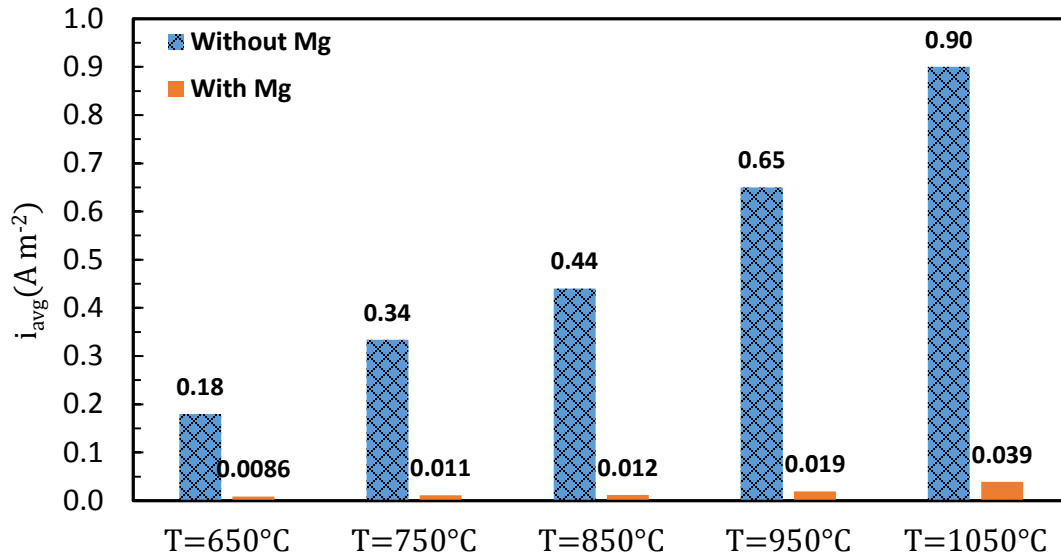
Figure 4.4. Prediction of average corrosion rate (current density) for Haynes 230 coupons for stagnant conditions at different temperature for the case with and without cathodic protection.
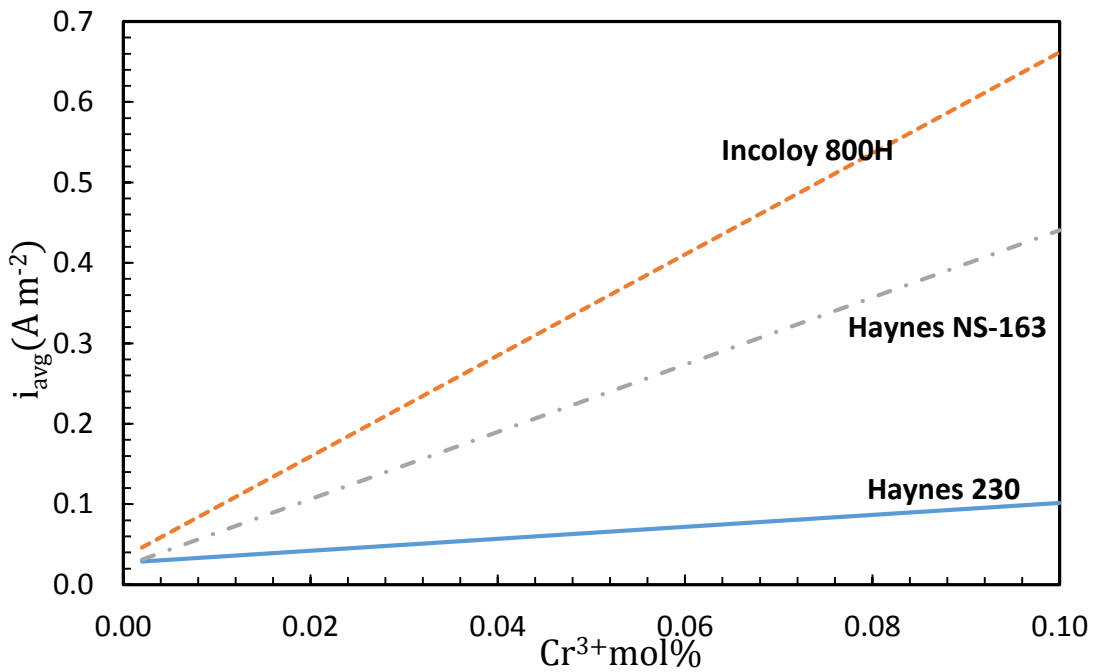
Figure 4.5. The effect of Cr^{3+} mol% at 850 ℃ on the average corrosion rate at the coupon surfaces with cathodic protection.

The corrosion rate seemed to be hardly affected by porosity for the cathodic protection case, as increasing the porosity from 0.1% to 0.5% only increased the corrosion rate by 2.0% and 5.0% at the cold and hot zones respectively, while increasing the porosity from 0.1% to 0.5% for the case without Mg, changes the corrosion rate by 70.0% and 30.0% at the cold and hot zones, respectively. This can be due to the fact that the mass transfer parameters have more effect on the corrosion rate for the case without Mg, as the kinetic effect is more than the mass transfer effect when Mg was added to the system.

SEM results of exposed Haynes 230 sample to KCl-MgCl$_2$ at 850 ℃ for 100 hours [57] showed that the corrosion happens in a layer of finite thickness, possibly microns to hundreds of microns thick. As described earlier this layer was considered as a porous microstructure that is open to the salt. The corrosion rate distributions at the surface of the coupons at cold and hot zones are shown in Figure 4.11. The results show that the thickness of the porous layer has an effect on the corrosion rate at both the cold and hot zones.The corrosion rate is decreased by increasing the thickness of the porous layer, as increasing the thickness by 10 times reduces the corrosion rate around 6.0% at the cold and hot zones for the case of with Mg and without Mg. That is caused by the fact that a thicker layer has a higher corrosion resistance, as the species should diffuse a longer distance to react with the alloy surface.

4.4 Summary

A 3D corrosion model has been developed that accounts for the corrosion mechanisms of super-alloys in KCl-MgCl$_2$ molten halide salts under cathodic protection. The electrochemical kinetics were incorporated into the CFD model, and both isothermal and non-isothermal conditions were considered. The model results well reproduce the

experimental data that was performed in the in-house SRNL thermosiphon reactor. The results were compared with the model was in good agreement with experimental results, showing less than a 1% difference. The effect of Mg concentration was considered in the model and the results showed adding even small amounts of Mg into the salt can rapidly reduce the corrosion rate at the surface of the coupons for both isothermal and non-isothermal conditions. The predicted results also showed that the thermal driven fluid flows in the non-isothermal condition could accelerate the corrosion rates reduction due to the more rapid movement of Mg to the metal surface. The results of cathodic protection showed that the corrosion rate of Haynes 230 in KCl-$MgCl_2$ containing 1.15 mol% Mg showed 35 times lower corrosion than baseline tests with no cathodic protection and met the DOE SunShot target.
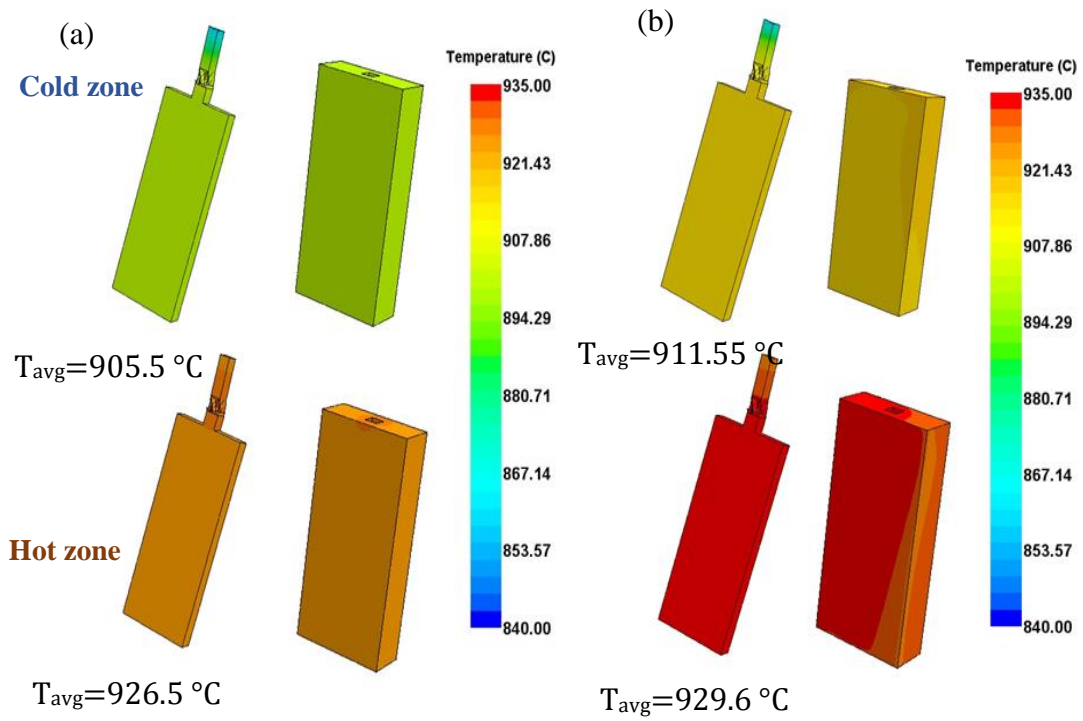
Figure 4.6. The model's temperature distribution at the surface of the coupons and around the coupons for the case of without cathodic protection (a) and with cathodic protection (b) at non-isothermal condition of 800-950 ℃.
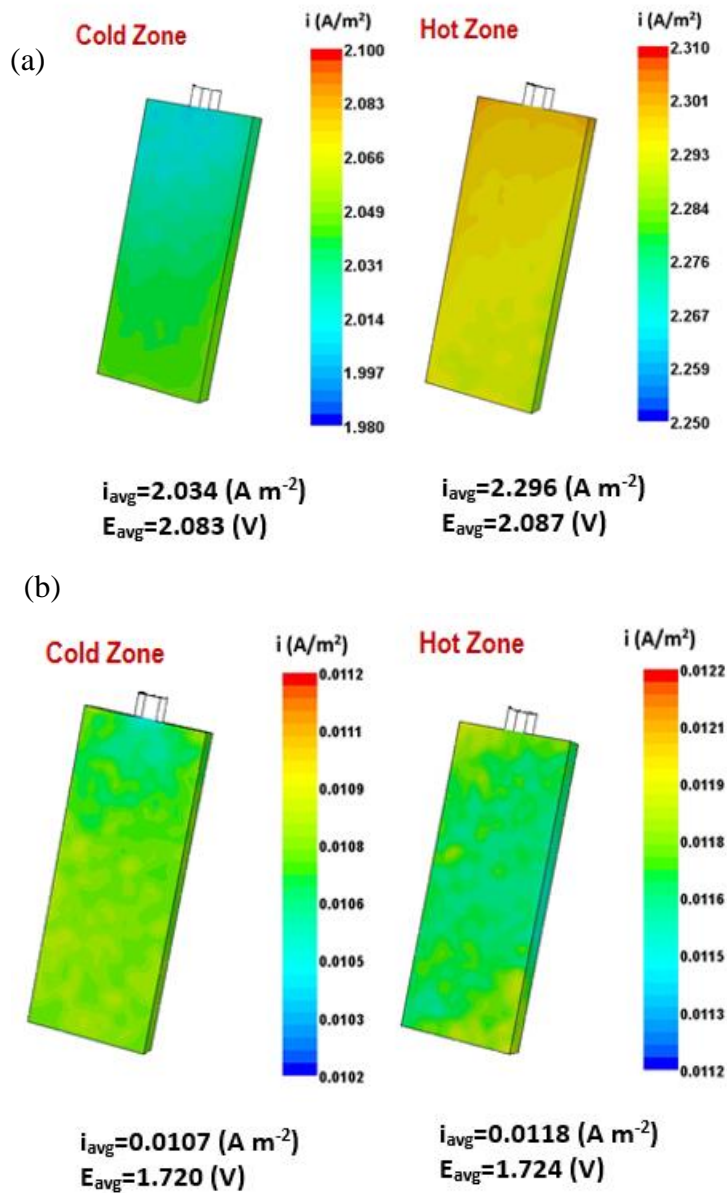
Figure 4.7. The corrosion current density distribution at the coupons without (a) and with Mg (b) introduced into the salt solution at the control temperature of 800-950°C and the amount of Mg of 1.15 mol%.
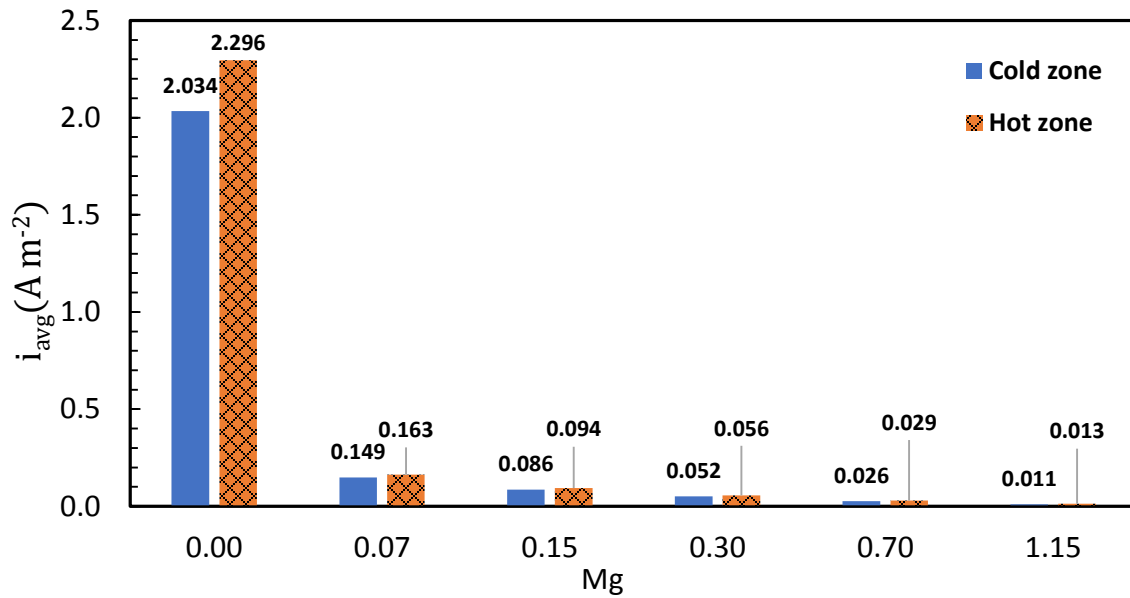
Figure 4.8. The predicted corrosion rates at the surface of the alloy with varying Mg content in the salt for both cold zone and hot zone at non-isothermal case (800-950 ℃).

$\varepsilon= 0.1\%$ $\varepsilon= 0.3\%$ $\varepsilon= 0.5\%$

Cold zone

$i_{avg} = 0.015$ A m^{-2} $i_{avg} = 0.016$ A m^{-2} $i_{avg} = 0.017$ A m^{-2}

Hot zone

$i_{avg} = 0.017$ A m^{-2} $i_{avg} = 0.018$ A m^{-2} $i_{avg} = 0.019$ A m^{-2}
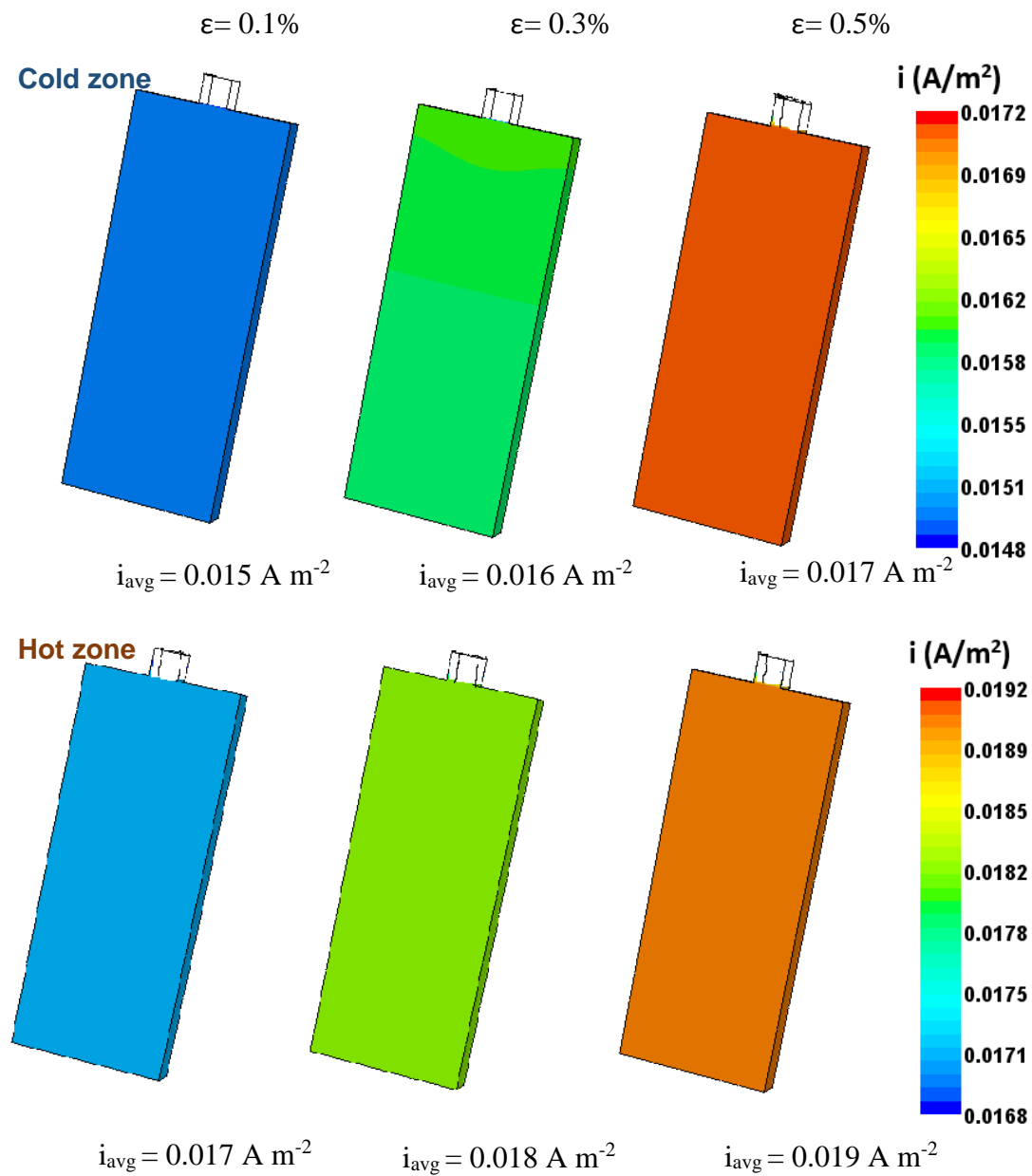
Figure 4.9. The effect of porous layer porosity on the corrosion rate distributions at both cold and hot zones for the case with 1.15% Mg at non-isothermal condition (800-950 ℃).
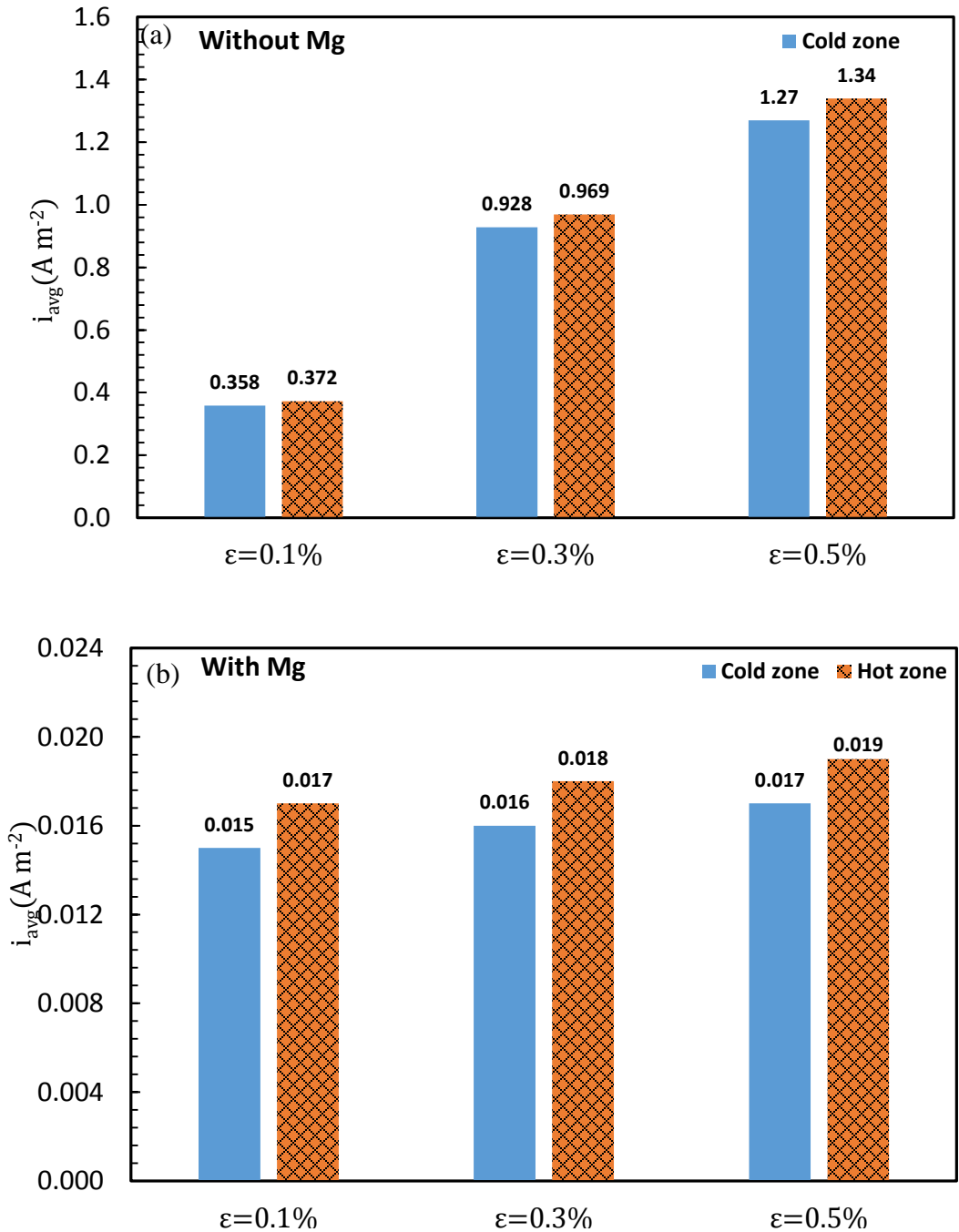
Figure 4.10. The effect of porous layer porosity on the corrosion rate at both cold zone and hot zone for the cases (a) without Mg and (b) with 1.15% Mg at non-isothermal case (800-950 ℃).
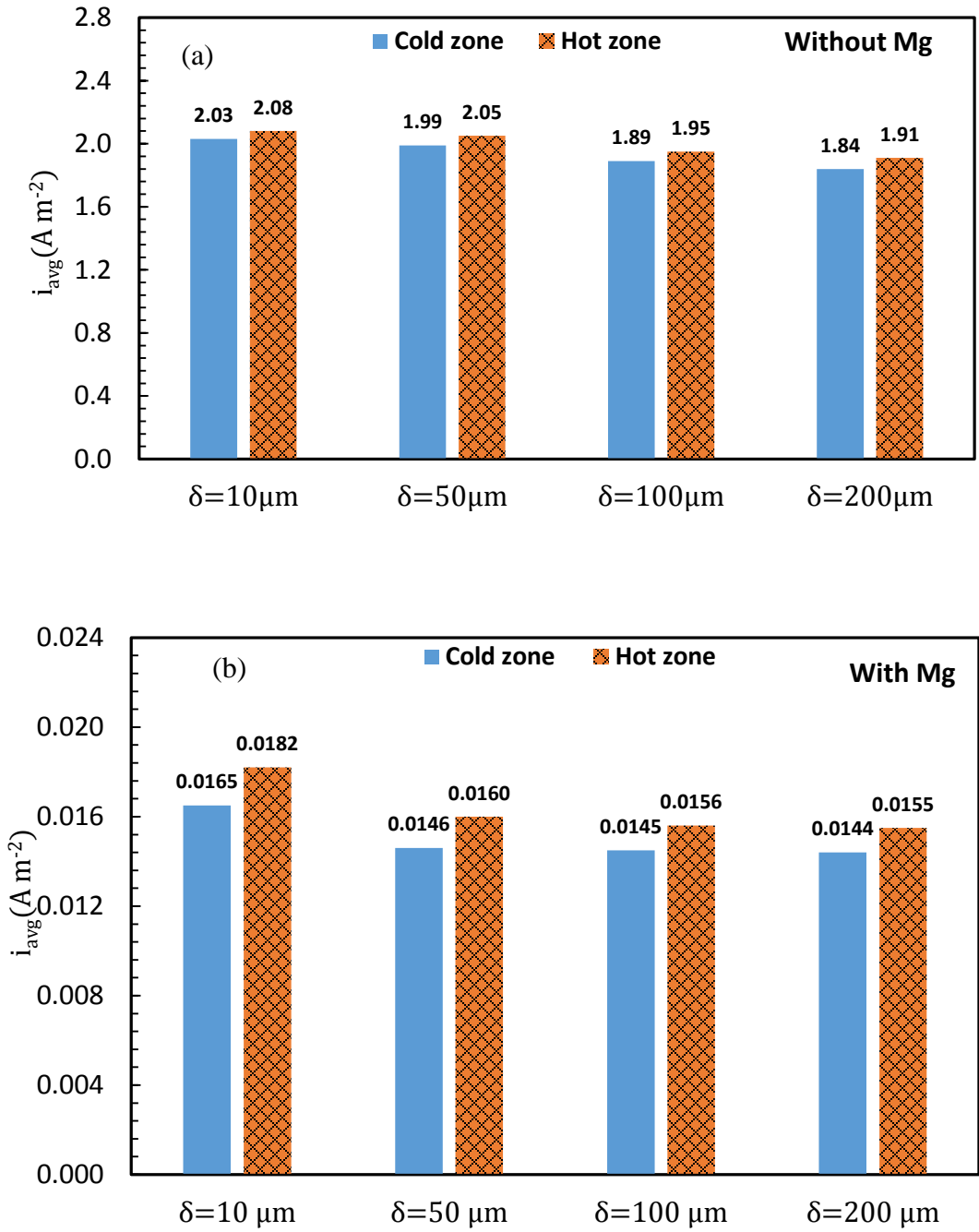
Figure 4.11. The effect of porous layer thickness on the corrosion rate at both cold zone and hot zone for the cases (a) without Mg and (b) with 1.15% Mg at non-isothermal case (800-950 ℃).

CHAPTER 5. EFFECT OF SYSTEM CONTAMINANTS ON THE PERFORMANCE OF A PROTON EXCHANGE MEMBRANE FUEL CELL

The performance loss and recovery of the fuel cell due to Balance of Plant (BOP) contaminants was identified via a combination of experimental data and a mathematical model. The experiments were designed to study the influence of organic contaminants (e.g. those from BOP materials) on the resistance of the catalyst, ionomer and membrane, and a mathematical model was developed that allowed us to separate these competing resistances from the data collected on an operating fuel cell. For this reason, based on the functional groups, four organic contaminants found in BOP materials, diethylene glycol monoethyl ether (DGMEE), diethylene glycol monoethyl ether acetate (DGMEA), benzyl alcohol (BzOH) and 2,6-diaminotoluene (2,6-DAT) were infused separately to the cathode side of the fuel cell. The cell voltage and high frequency impedance resistance was measured as a function of time. The contaminant feed was then discontinued and voltage recovery was measured. It was determined that compounds with ion exchange properties like 2,6-DAT can cause voltage loss with non-reversible recovery, so this compound was studied in more detail. The degree of voltage loss increased with an increase in concentration, and/or infusion time, and increased with a decrease in catalyst loadings.

5.1 Introduction

The major technical challenges for polymer electrolyte membrane fuel cells (PEMFCs) in general are performance, reliability, durability and cost. There is an opportunity to reduce overall system cost by choosing lower cost balance of plant (BOP) materials for PEMFC systems. However, choosing any new system BOP material (e.g., assembly aids, structural plastics, and hoses) without compromising function, fuel cell performance, or life requires understanding the effects of the contaminants that leach from these materials. The contaminants in a fuel cell system originate from the fuel, air, and the different component materials used in construction.

Previous studies [72-93] have reported on the effect of contamination on PEMFCs by impurities found in the fuel, fuel-cell components, or the external environment such as carbon monoxide (CO)) [79], hydrogen sulfide (H_2S) [81, 94], and ammonia (NH_3) [82, 84, 95]. Works have also been reported on the effects of air contaminants, such as nitrous oxides (NO_x) [85, 86], sulfur oxides (SO_x) [77, 87, 88], and volatile organic compounds present in the atmosphere (toluene) [89] . It has been demonstrated that even trace amounts of impurities in the fuel or air stream can severely poison the anode, membrane, and cathode, particularly at low-temperature operation [75]. These contaminants impact PEMFC performance by hindering kinetics (e.g. CO and H_2S) or reducing membrane conductivity (e.g. NH_3 and metal cations) [79, 96, 97]. Several models are available that capture kinetic [85, 90, 91] and ohmic overpotentials [92, 93] during the contamination and recovery studies.

Although there has been a lot of research on contamination caused by fuel and air side impurities, the effect of contamination originating from system components have only

recently been briefly studied [98-104]. These results showed that despite the contamination caused by fuel and air side impurities that can effect only the catalyst (e.g., CO) or the membrane (e.g. metal cations), organic contaminants (e.g., those from BOP materials) can have severe effects on the catalyst, ionomer and membrane at the same time. Opu et al. [105] selected twenty assembly aids BOP materials and categorized them according to their intended use and chemical composition. Their data indicated three different phenomena affect the cell: adsorption of contaminant species on the Pt catalyst, ion exchange with the sulfonate sites in the membrane and ion exchange with the ionomer of the catalyst layer. Their studies also showed the effect of individual functional groups in poisoning the fuel cell. The effects of contamination by some organic model compounds derived from the fuel cell BOP on performance in PEMFCs were examined by Cho et al. [99]. Their results revealed severe impacts on performance in PEMFCs depending on functionalities which allowed multiple contamination mechanisms. In another work Cho et al. [106] developed a mathematical model for organic contaminants that come from BOP materials by considering the effect of contamination on the catalyst, electrode ionomers and membrane. However they looked at the limited conditions and their derivation did not extend to the case of the cell performance after recovery from a contamination period. They also included mass transport phenomena in the model, which is not necessary to achieve model accuracy [89], resulting in computational inefficiencies.

The purpose of the work reported here is to identify the causes for performance loss and recovery of a fuel cell due to BOP contaminants via a combination of experimental data and a mathematical model. An analysis procedure was developed to quantify the various voltage losses caused by contaminants during both fuel cell contamination and recovery

86

operations. The impacts of contamination examined are the adsorption onto the Pt surface (kinetic losses) and ion exchange with the membrane and ionomer in the catalyst layer. The ion exchange with acidic sites in the catalyst layer ionomer results in both a loss in conductivity (ohmic loss); and loss in proton activity (kinetic loss).

Based on the functional groups examined in previous studies, four organic contaminants were chosen as these compounds have been identified in leachates from BOP materials [107]. They are listed as: diethylene glycol monomethyl ether (DGMEE), diethylene glycol monoethyl ether acetate (DGMEA), benzyl alcohol (BzOH) and 2,6-diaminotoluene (2,6-DAT). Their chemical structures are shown in Figure 5.1. The effect on performance of 2,6-DAT was the more complex and irreversible, and so more detailed analysis was performed under a variety of concentration, infusion times, and cathode catalyst loadings. The experimental data was then used with the model to correlate cell voltage to contamination levels and cathode catalyst loadings. This analysis provides insight into the effect of contaminant on fuel cell performance.
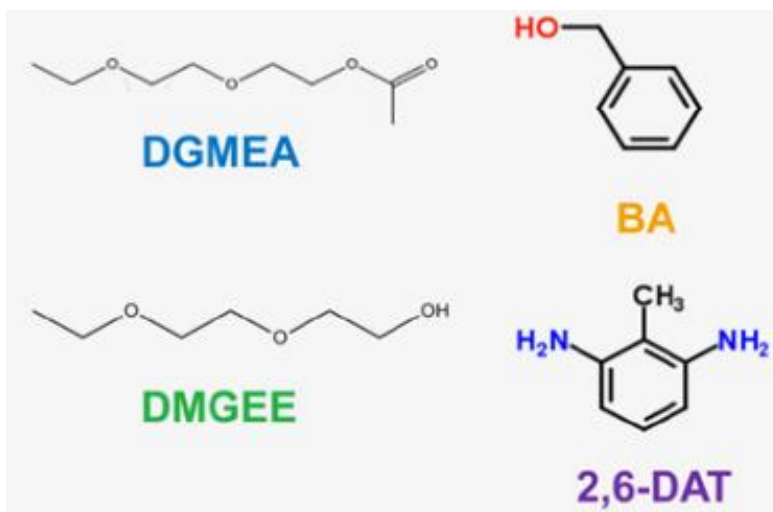
Figure 5.1. Chemical structures of DGMEA, BA, DMGEE and 2,6-DAT.

87

5.2 Experimental

Experiments discussed in this work were tested on a Model 850e test station made by Scribner Associates Inc. High purity hydrogen and compressed air were used as the fuel and reactant. The temperature of the cell was controlled at 80°C with heating by cartridge rods and cooling with a fan controller system. The same operating temperature was used for all experiments. The back pressure was 150 kpa. Our experimental MEAs with 50 cm^2 membrane active area are prepared by General Motors Electrochemical Energy Research Lab using a DuPont Nafion 211 membrane, a 0.05 mg/cm^2 Pt-C (Tanaka carbon) loading on anode, and different loading of 0.1 and 0.4 mg/cm^2 Pt-C (Tanaka carbon) on cathode side. The infusion experiment was run at 0.2 A/cm^2 constant current.

After the MEA was conditioned, a few beginning of test (BOT) diagnostics were performed. The BOT diagnostics included a dry (32% relative humidity) polarization curve and cathode hydrogen adsorption CV scans at 80°C. Following the BOT diagnostics, a micro-nebulizer (ES-4040 Polypro ST Nebulizer) was attached between the outlet of the test stand and the cathode inlet of the cell. The micro-nebulizer was used to deliver the contaminant solution to the test cell in an aerosol form. The anode side was humidified from the test stand to 32% RH and the nebulizer delivered the cathode humidity. After attaching the nebulizer to the cell through the cathode inlet, the infusion experiment was started. The experiment were run around 20 hours with DI water to make a stable baseline before introducing the contaminant leachate solution. Following this 20 hours, the leachate solution was infused through the nebulizer to the cathode inlet at the same rate as before. After the contaminant solution infusion was stopped, air was humidified with deionized (DI) water via infusion for certain length of time, to determine if any voltage loss induced

from the contaminants in the solution was recoverable with normal operation. This is the self-induced recovery (SIR) period. The cell voltage and high frequency resistance (HFR) were monitored continuously during the infusion time.

Four assembly aids system materials, Diethylene glycol monoethyl ether (DGMEE), Diethylene glycol monoethyl ether acetate (DGMEA), Benzyl alcohol (BzOH) and 2,6-Diaminotoluene (2,6-DAT) with total organic carbon of 64 ppm are compared. In addition, six different concentration of 2,6-DAT with total organic carbon (TOC) amount of 10 ppm, 25 ppm, 64 ppm, 128 ppm, 200 ppm and 256 ppm at three different infusion times of 30, 50, and 90-hour are examined.

Figure 5.2 shows a typical IR_m corrected cell voltage E_m, in response to exposure to 64 ppm 2,6-DAT. The experiment is divided into three distinct phases, which are labeled in Figure 5.2. Phase 1 is the pre-poisoning period conducted with clean H_2/air. Extrapolation of the Phase 1 value serves as the baseline (dashed line). Phase 2 (i.e. t=0) begins with the introduction of contaminant into the cathode feed stream. In the experiments reported in this work, contaminant concentration was held constant throughout Phase 2. In Phase 3 (i.e., $t = t_1$) the self-induced recovery (SIR) period begins when the flow of the contaminant is stopped and operation of clean H_2/air is resumed. During these phases we bypass the cathode humidifier and the humidity is maintained with contaminant solution flowing through the nebulizer.
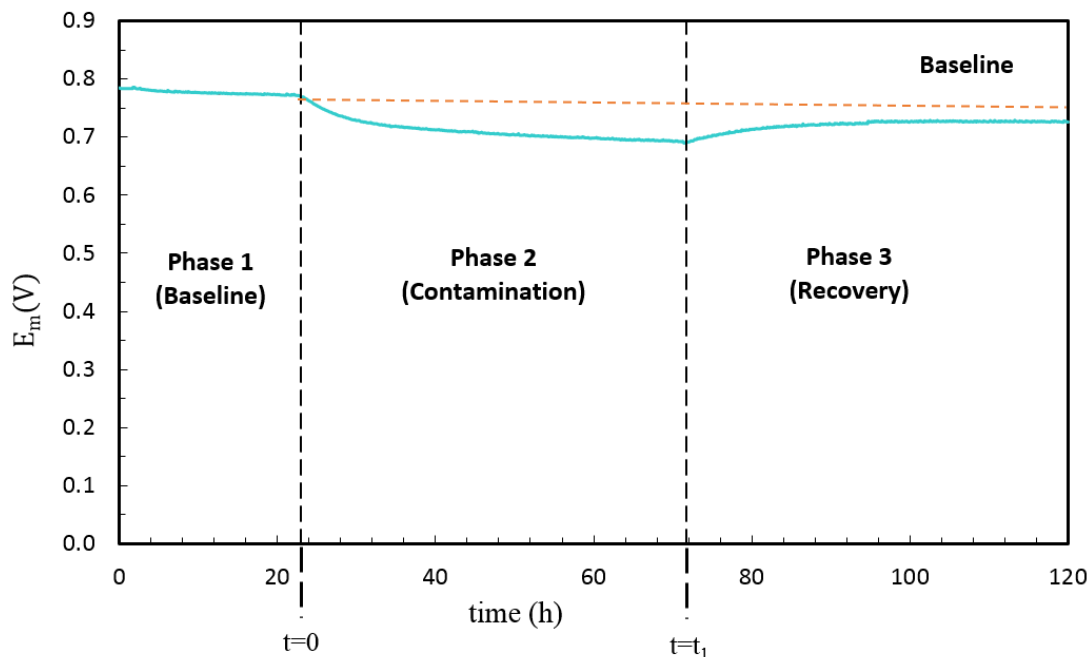
Figure 5.2. Example of IR_m corrected cell voltage (ΔE_m) vs. time for a 50-hour infusion of 64 ppm 2,6-DAT at 0.2 A/cm^2 into a 0.4 mg/cm^2 Pt/C cathode catalyst loading.

5.3 Model Description

In developing the model below, we assume the contaminants affect performance in three primary ways: (1) adsorption onto the Pt surface, (2) ion exchange with the membrane, and (3) ion exchange with the ionomer in the catalyst layer. The latter effect has two contributions to the voltage losses. One is the ionomeric resistance increase (ohmic losses) from the reduction in acidic sites and the other is the kinetic losses due to the proton concentration changes in the catalyst layer. We ignore secondary effects such as changes in transport rates of reactants through the catalyst layer [108, 109], increase in peroxide production [108-110] or changes in Tafel slopes [111-113] as has been reported previously. Also, ion exchange with the membrane can lead to highly non-linear effects at high currents or significant cation exchange [96, 97]. These effects have been ignored due to the

90

relatively low current densities (current density $= 0.2$ A/cm^2) and mild contamination conditions (contaminant concentration < 256 ppm) investigated here.

As a result the total voltage change by contamination can be written as follows:

$$V_{cell} = E_{eq} - \eta_a - \eta_c - IR_i - IR_m \qquad \text{5-1}$$

where the variables are defined in the list of symbols. IR_i represents the overpotential arising from the resistance of the ionomer in the electrode and IR_m is the ohmic loss across the membrane. As we want to isolate the effect of contamination on the electrode from the effect of contamination on the membrane, we measured the membrane resistance using high frequency resistance (HFR). The HFR value was then used to determine the IR_m corrected voltage, E_m as is given below:

$$E_m = V_{cell} + IR_m = E_{eq} - \eta_a - \eta_c - IR_i \qquad \text{5-2}$$

We assumed the anodic overpotential is negligible and the oxygen reduction reaction follows Tafel kinetics:

$$\eta_c = \frac{1}{\beta} \ln \left[\left(\frac{I}{\delta a i_0} \right) \left(\frac{C_{O_2}}{C_{O_2,0}} \right) \left(\frac{C_{H^+}}{C_{H^+,0}} \right)^{-1.5} \right] = \frac{1}{\beta} \ln \left[\left(\frac{I}{\delta a i_0} \right) (1-y)^{-1.5} \right] \qquad \text{5-3}$$

where y is the fraction of contamination in the ionomer at the catalyst layer (i.e., $y = 1 - \frac{C_{H^+}}{C_{H^+,0}}$), and $1/\beta$ is the Tafel slope that we set to 0.060 V/decade [114]. The concentration of O_2 in the catalyst layer is eliminated in Equation 5-3, as it was assumed constant through the experiment. The reaction rate is assumed to be a 1.5 order with respect to the proton concentration as proposed previously [115]. δ is the catalyst layer thickness assumed equal to 2.5 and 10 μm for 0.1 and 0.4 mg/cm^2 respectively. The active surface area of the catalyst

per unit volume, a, changes with time due to contamination of the Pt particles. The fraction of active platinum sites loss during contamination, θ, is related to a by:

$$\theta = \left(1 - \frac{a}{a_0}\right)$$

5-4

where a_0 is the active surface area of the catalyst per volume before contamination.

Substituting Equations 5-3 and 5-4 into the Equation 5-2 and writing it relative to the baseline (see dashed line in Figure 5.2) gives:

$$\Delta E_m = \Delta\eta_c + \Delta IR_i = -\frac{1}{\beta}\ln[(1-\theta)(1-y)^{-1.5}] - \frac{\delta I}{\sigma_0}\left[1 - \frac{\sigma_0}{\sigma}\right]$$

5-5

where $\Delta\eta_c$ is kinetic loss and ΔIR_i is ohmic loss. Two contributions on ionomer voltage losses are considered in Equation 5-5. One is from proton concentration changes by ionomer contamination y, and the other is ohmic loss due to the inomer cation composition has changed, σ. The fraction of active platinum sites loss changes exponentially with time during both contamination and recovery as given by Pierre [85] and Zhang et al. [107], resulting in the following expressions.

$$\theta = \theta_1(1 - e^{-\gamma_{cc}t}) \qquad \text{for } 0 \le t \le t_1$$

5-6

$$\theta = \left[\theta_1 - (\theta_1 - \theta_2)(1 - e^{-\gamma_{cr}(t-t_1)})\right] \qquad \text{for } t_1 < t$$

5-7

where θ_1 is the fractional loss of catalyst sites after steady-state contamination, and θ_2 is the fractional loss of catalyst sites after steady-state recovery. The parameters γ_{cc} and γ_{cr} are the rates of catalyst poisoning and recovery, respectively.

The second contribution to the kinetic loss in Equation 5-5 is the change in proton concentration in the ionomer, y. The level of poisoning in the ionomer during

contamination and recovery is also expected to follow an exponential relationship similar to Equations 5-6 and 5-7 [92, 93]. However, the rate of ionomer poisoning during contamination is observed to be very small relative to complete ionomer poisoning. Therefore, the exponential relationship is linearized during contamination (Equation 5-8) but the full exponential form is used during the recovery step (Equation 5-9), to predict the change in proton concentration in the ionomer.

$$y = \gamma_{ic}t \qquad \text{for} \quad 0 \le t \le t_1 \qquad \text{5-8}$$

$$y = y_1 - (y_1 - y_2)[1 - e^{(-\gamma_{ir}(t-t_1))}] \qquad \text{for} \quad t_1 < t \qquad \text{5-9}$$

where γ_{ic} and γ_{ir} are the rates of ionomer poisoning and recovery, respectively, and y_1 is the fraction of contamination in the ionomer at $t = t_1$, and y_2 is the fraction of contamination in the ionomer after steady state recovery (i.e., $t \to \infty$).

The proton concentration in the ionomer not only affects the kinetics, but it also impacts the ionic conductivity. The ionomer conductivity, σ_0, is the effective ionic conductivity of the catalyst layer which can be obtained by Equation 5-10 [116].

$$\sigma_0 = 0.167 \, \sigma_m \qquad \text{5-10}$$

where σ_m is the pure ionomer conductivity without any carbon, catalyst, contamination, etc. which is equivalent to the uncontaminant polymer membrane conductivity and equal to 10 mS/cm for Nafion 211 at 80 °C and 30% humidity [116].

The ion exchange reaction of 2,6-DAT in the membrane is similar to aniline and ammonia [99]. The ionomer conductivity is exponentially related to the proton concentration [93] and can be related to y by:

$$\sigma = \sigma_0[1 - 1.33(1 - e^{-1.4y})] \qquad\qquad 5\text{-}11$$

The parameters 1.33 and 1.4 are obtained by using experimental data provided by Hongsirikan [117] for NH_4^+ exchange membrane at 30% RH and 80°C for Nafion 211. Although the 2,6-DAT cation is much bigger than NH_4^+, the mechanism for ion conductivity loss is similar [99].

The parameters θ_1, γ_{cc} and γ_{ic} are obtained by fitting Equations 5-5, 5-6, 5-8, 5-10 and 5-11 to the experimental data by the method of least squares. The parameter y_1 is then obtained by setting $t = t_1$ in Equation 5-8. For recovery, the parameters $\theta_2, \gamma_{cr}, \gamma_{ir}$ and y_2 are obtained by fitting Equations 5-5, 5-7 and 5-9 through 5-11 to the data. Finally, the parameters are correlated to operating conditions (e.g., contaminant concentrations, infusion times, and catalyst loading) as presented below.

5.4 Results and Discussions

Figure 5.3 shows the IR_m-corrected cell voltage difference (ΔE_m) in response to two aliphatic compounds and two aromatic compounds at 64 ppm. The aliphatic being diethylene glycol monoethyl ether (DGMEE) and diethylene glycol monoethyl ether acetate (DGMEA), and two aromatic compounds named, benzyl alcohol (BzOH) and 2,6-diaminotoluene (2,6-DAT). The model fits to these data are also shown as lines in Figure 5.3 (Equations 5-5 through 5-11). Three parameters are used to fit the contamination part:

94

the fractional loss of catalyst sites after steady state contamination, θ_1, the rate of catalyst poisoning, γ_{cc}, and the rate of ionomer poisoning, $\gamma_{i,c}$. The proton concentration at the start of recovery (y_1) is then obtained from Equation 8. Finally, four parameters are used to fit recovery: the fractional loss of catalyst sites after steady state recovery θ_2, the rate of catalyst recovery, γ_{cr}, the rate of ionomer recovery, $\gamma_{i,r}$, and the fraction of contamination in the ionomer after steady state recovery, y_2.

5.4.1 Effect of Different Organic Compound Functional Groups

Figure 5.3 shows that the voltage response of DGMEE, DGMEA, and BzOH are qualitatively different from the voltage response of the compound 2,6-DAT. The voltage difference reached steady state very quickly with the infusion of compounds DGMEE, DGMEA, and BzOH; and near complete (reversible) performance recovery was observed in these three cases after switching back to the normal operating conditions during the self-induced recovery (SIR) period. The results from previous studies [118] for similar molecules such chlorobenzene[118] and toluene [119] has also shown similar effects. As these contaminants mainly affected the catalyst and there was little coupled phenomena of catalyst and ionomer poisoning. For these compounds a similar fit would be obtained if using the model presented by St-Pierre et al. [90, 91]. In contrast, poisoning with 2,6-DAT was more gradual and complete recovery was not observed with this compound (irreversible).

The main reason for irreversible poisoning of 2,6-DAT could be due to the fact that it has the capability of ion-exchange with the proton sites of the ionomer, while the

compounds BzOH, DEGMEA and DGMEE have no protonated functionalities in their chemical structures and have dominant interactions with the catalyst rather than the ionomer. As a result, the parameters associated with the ionomer poisoning and recovery (γ_{ic}, γ_{ir}, and y_2) are negligibly small, and the rate parameters associated with catalyst poisoning and recovery (γ_{cc}, γ_{cr}) are larger for these three compounds (see Figure 5.4a). For example, γ_{cc} is nearly 4 times larger (poisons 4 times faster), and γ_{cr} is almost 20 times larger (recovers 20 times faster) for BzOH compared to 2,6-DAT. This is due to the fact that BzOH does not interact with the ionomer and immediately poisons the catalyst during the contamination and recovery, respectively. According to Cho et al. [120] the difficult removal of 2,6-DAT is due to the strong electrostatic interaction (i.e., ion-exchange reaction) between hydrolyzed amines of 2,6-DAT and the sulfonic acid groups of the ionomer, so the absorbed 2,6-DAT can be difficult to remove from the catalyst layer. If the poison cannot leave the ionomer, a portion will remain adsorbed on to the catalyst. Figure 5.4 (b) shows that the catalyst surface coverage during the contamination (θ_1) is almost identical for DGMEE, DGMEA, and 2,6-DAT ($\theta_1 \sim 0.8$) and slightly larger for BzOH ($\theta_1 \sim 0.95$). However the catalyst almost completely recovers for DGMEE, DGMEA and BzOH ($\theta_2 \leq 0.10$), where 37% of the Pt sites poisoned during the contamination step are unrecoverable after 2,6-DAT is stopped ($\theta_2 = 0.30$). Again, this could be due to the fact that the poison remains trapped in the catalyst layer during the recovery for 2,6-DAT.

Although three parameters (θ_1, γ_{cc} and γ_{ic}) were fit simultaneously during the contamination (and four parameters, θ_2, γ_{cr}, γ_{ir} and y_2, during recovery), some of their values can be confirmed by examining various regions of the voltage-loss curves. For

example, the initial voltage lose is dominated by catalyst contamination such that the initial slope in Figure 5.3 is directly related to the rate of catalyst poisoning, γ_{cc}. Also the more gradual linear portion of the voltage loss at longer times (e.g., between 20 and 30 hours in Figure 3) is dominated by the rate of ionomer poisoning. Similar, the initial voltage recovery at $t_1 < t$ is dominated by the recovery of the catalyst site (i.e., γ_{cr}).This analysis gives us confidence that we are extracting a unique set of parameters values from our least-squares fit.
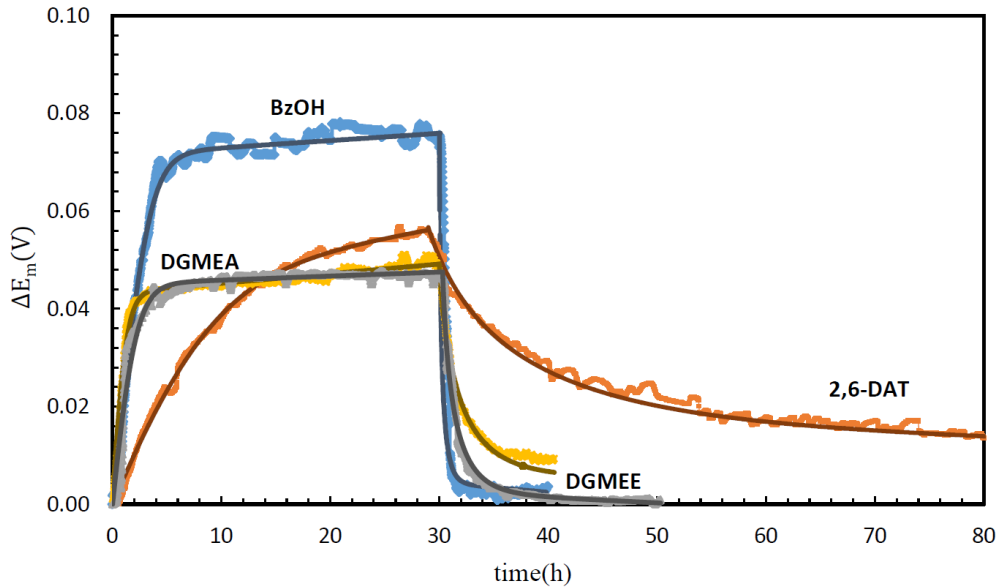
Figure 5.3. Corrected cell voltage, ΔE_m, for different model compounds (64 ppm) for 0.4 mg/cm^2 catalyst loading. The symbols are the experimental data and the lines are the model prediction.
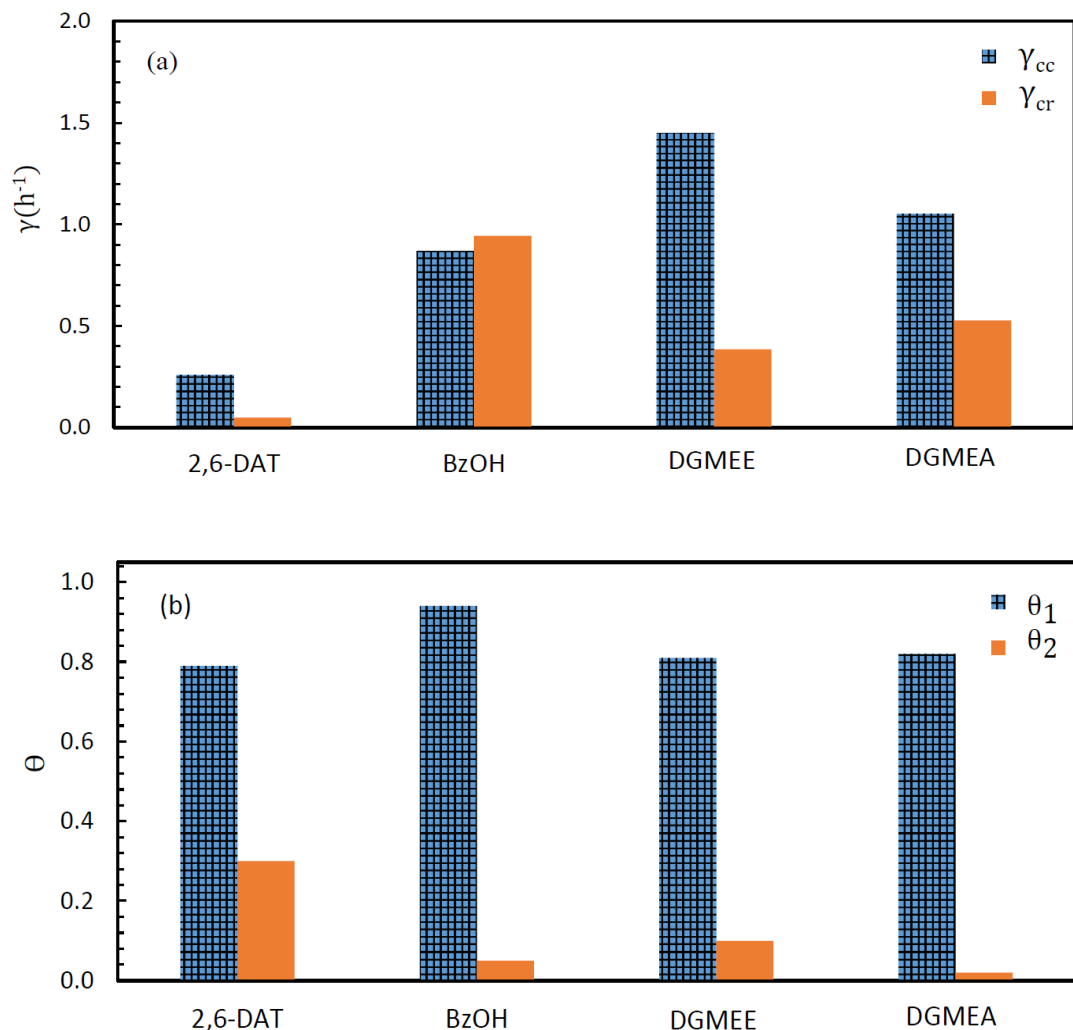
Figure 5.4. Parameters obtained by fitting the model to the experimental data at 30-hour, 0.4 mg/cm^2 cathode catalyst loading at 64 ppm for four organic compounds (a) the rate of catalyst poisoning and recovery during contamination (γ_{cc}) and recovery (γ_{cr}), (b) the fraction of sites poisoned during contamination (θ_1) and recovery (θ_2).

5.4.2 Effect of Concentration and Infusion Time

Since 2,6-DAT is the only contaminant that interacts with the ionomer and catalyst, the effect of the 2,6-DAT concentration, infusion time, and catalyst loading on voltage loss and recovery was examined in detail. Figure 5.4 (a) shows ΔE_m in response to 128 ppm

2,6-DAT at 30 and 50 hour infusion times and 64, 128 and 256 ppm at a 30 hour infusion time. Comparing the effects of infusion time, the voltage losses are nearly identical during contamination with parameters values of $\theta_1 = 0.86$, $\gamma_{cc} = 0.51$ (h^{-1}) and $\gamma_{ic} = 0.01$ (h^{-1}). As expected the parameters during contamination are not influenced by when the infusion of contaminant is stopped. Recovery though is effected because the loss of ion-exchange sites in the ionomer at the end of infusion, y_1, is a function of infusion time. That is from Equation 5-8, y_1 increases from 0.24 to 0.40 as infusion time is increased from 30 to 50 hours. The resulting recovery parameters θ_2, γ_{cr} , γ_{ir} and y_2 are changed from 0.45 to 0.52 , 0.09 (h^{-1}) to 0.14 (h^{-1}) , 0.60 (h^{-1}) to 0.50 (h^{-1}) , and 0.08 to 0.09 , respectively. The results show the parameters θ_2, γ_{cr}, and y_2 are increased by increasing y_1 and the parameter γ_{ir} is decreased by increasing y_1. Hence a higher level of ionomer contamination affects the eventual recovery of both the ionomer and the catalysts.

Figure 5.5 (a) also shows a higher voltage loss for 128 and 256 ppm compared to 64 ppm. The parameters obtained by fitting of the model to the experimental data show that θ_1 increases from 0.79 to 0.87 by increasing the concentration of the contaminant from 64 to 256 ppm. The values for θ_2 also increased from 0.30 to 0.70 by increasing the concentrations from 64 to 256 ppm. From these results, the parameters in the model are not a function of contamination dosage but rather the feed concentrations.

To gain more insight into the voltage loss, ΔE_m at 256 ppm is divided into kinetic ($\Delta \eta_c$) and ohmic (ΔIR_i) contributions in Figure 5.4 (b) (i.e., Equation 5-5). As Figure 5.4 (b) shows the ohmic contribution to the voltage loss (ΔIR_i) is small in the beginning since kinetic losses dominant at low concentrations and short infusion times. The ohmic

contribution to the voltage loss increases exponentially with time due to the exponential dependence of ionomer conductivity with proton concentration (Equation 5-11).
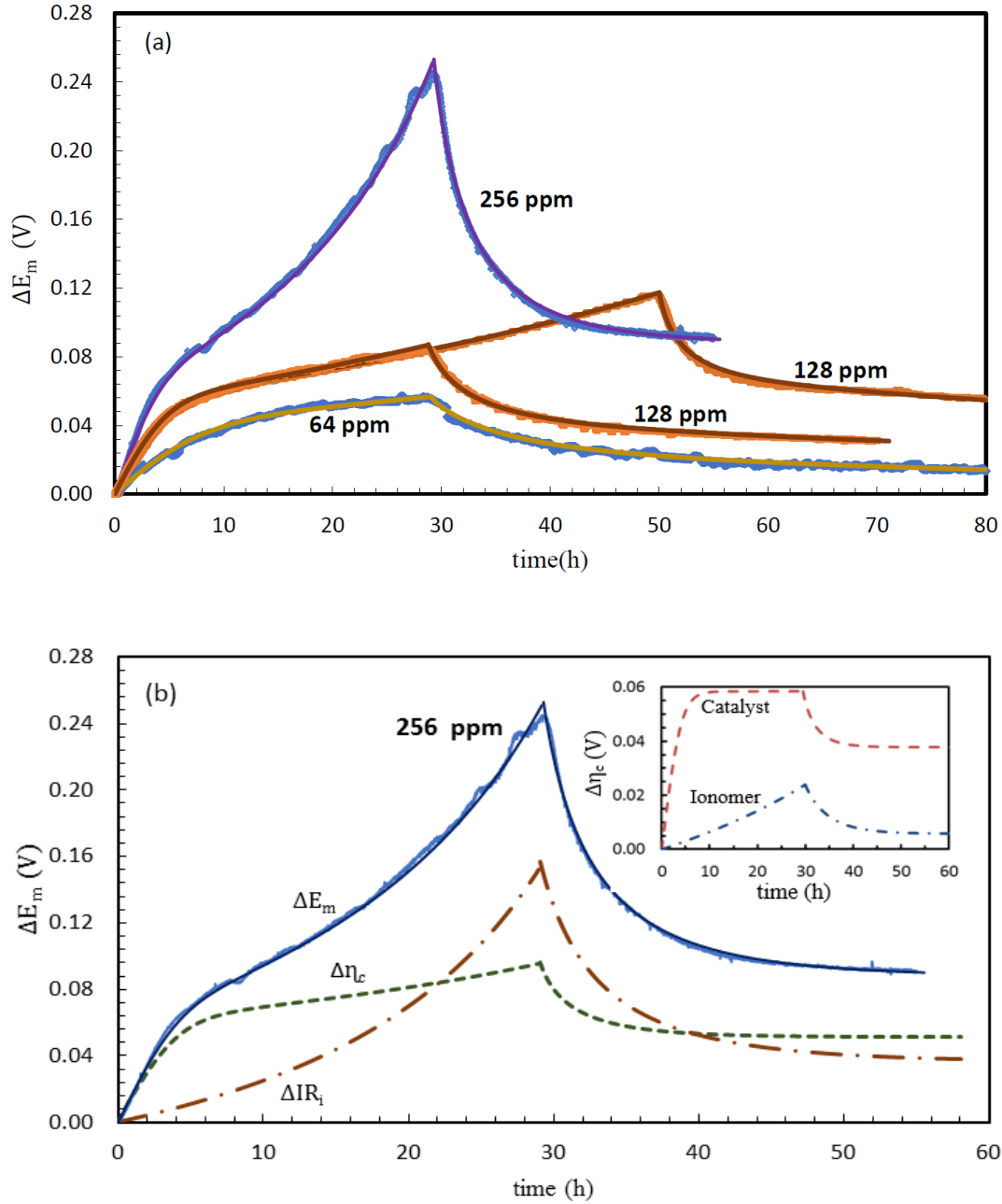
Figure 5.5. a) ΔE_m for different concentrations and infusion times of 2,6-DAT. The symbols are the experimental data and the lines are the model prediction. b) The contribution of kinetic and ohmic loss during the contamination and the recovery for the case of 256 ppm. The inset shows the contribution from each of the kinetic contamination (i.e., catalyst, and ionomer) to the voltage loss for the case of 256 ppm for 0.4 mg/cm^2 catalyst loading.

The kinetic losses can be further divided into losses from the catalyst (θ) and the ionomer (y), which are shown in the inset. The inset shows the voltage loss due to catalyst poisoning rises rapidly and levels off after approximately 10 hours via Equation 5-6. The voltage loss by contamination of the ionomer is small at the beginning but continues to increase as y increases with time (Equation 5-8). The data in Figure 5.5 (b) also indicates that at 256 ppm the voltage loss after 10 hours deviates from linearity in comparison to 64 and 128 ppm in Figure 5.5 (a). This nonlinearity is caused by the nonlinearity in ohmic resistance, which is caused by the nonlinear relationship between y and the conductivity (Equation 5-11).

5.4.3 Effect of Catalyst Loading

The plot in Figure 5.6 shows ΔE_m in response to 64 ppm 2,6-DAT contamination at two different cathode catalyst loadings of 0.4 and 0.1 mg/cm^2. As expected, lower catalyst loading resulted in a stronger response to an identical contaminant concentration. The ΔE_m for the catalyst loading of 0.1 mg/cm^2 also shows the deviation from linearity after 10 hours in comparison to 0.4 mg/cm^2. This result has the similar trend to what was observed for the higher concentration of 256 ppm at catalyst loading of 0.4 mg/cm^2 (Figure 5.5). The comparison of model parameters for these two cathode catalyst loadings show that decreasing the cathode catalyst loading by a factor of four, change the values of θ_1 and θ_2 from 0.80 and 0.30 to 0.90 and 0.80 respectively. A similar change in parameter values occurs when the catalyst loading is held constant at 0.4 mg/cm^2 but the concentration of 2,6-DAT is increased by a factor of four from 64 to 256 ppm. Therefore, we do not need to correlate the model parameters to the concentration and catalyst loadings separately.

Rather we can correlate them to the ratio, φ (ppm/mg$_{Pt}$), which is defined as the ratio of contaminant concentration to the amount of Pt.
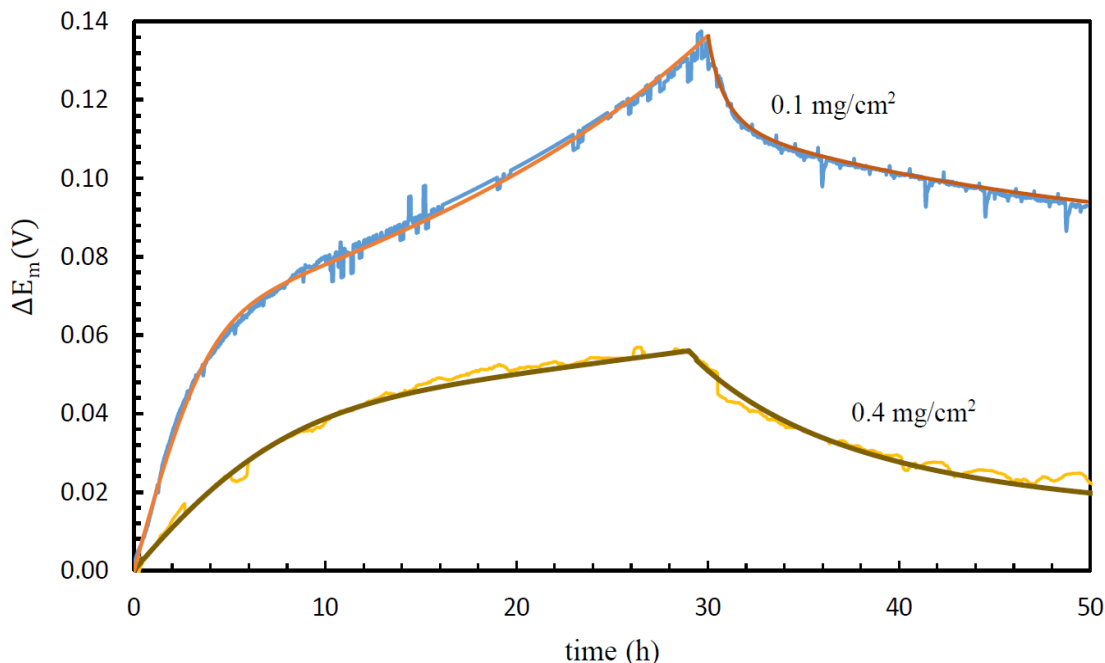
Figure 5.6. ΔE_m for different catalyst loadings at 30-hour infusion time and 64 ppm 2,6-DAT.

The effects of all of the experimental conditions, (i.e., concentrations, infusion times and cathode catalyst loadings) on model parameters (i.e., θ_1, γ_{cc}, and γ_{ic}) during the contamination were evaluated and plotted in Figures 5.7-5.9, respectively. The experimental conditions for these data are shown in Table 5.1 along with the symbol used in Figures 5.7-5.13. Figure 5.7 shows the fraction of sites poisoned during contamination (θ_1) obtained by fitting the model to the experimental data at different conditions as a function of φ. For example, the value of θ_1 from Figure 5.5 (a) increased from 0.79 to 0.87 as the concentration of 2,6-DAT increased from 64 to 256 ppm. Also θ_1 increased from

0.79 to 0.90 as the catalyst loading decreased from 0.4 to 0.1 mg/cm^2. The parameter values

are fit to the following empirical expression, and shown as the dotted line in Figure 5.7.

$$\theta_1 = 0.873(1 - e^{-1.21\varphi})$$
<div align="right">5-12</div>

Table 5.1. Different experimental conditions and symbols correspond to these experimental conditions.

Time (h)	TOC (ppm)	Catalyst loading (mg$_{Pt}$/cm^2)	φ(TOC/mg$_{Pt}$)	y_1	Symbol
30	10	0.4	0.5	0.024	●
30	25	0.4	1.3	0.060	●
30	64	0.4	3.2	0.120	●
30	128	0.4	6.4	0.240	●
30	200	0.4	10.0	0.405	●
30	256	0.4	12.8	0.609	●
50	25	0.4	1.3	0.100	■
50	64	0.4	3.2	0.200	■
50	128	0.4	6.4	0.400	■
90	25	0.4	1.3	0.180	▲
90	64	0.4	6.4	0.360	▲
30	64	0.1	12.8	0.630	◆

The results show that the fraction of sites poisoned increase with increasing contaminant

concentration or decreasing Pt loading in the catalyst layer, and then it levels off at $\theta_1 =$

0.87. These results have the same trends as ex-situ adsorption isotherm of 2,6-DAT

reported by Cho et al [106]. The maximum value for θ_1 reported in Figure 5.7 and Equation

5-12 is 0.873. This corresponds to maximum voltage loss of 60 mV due to catalyst

poisoning or 8% of the initial voltage of 780 mV. To keep the voltage loss due to catalyst

poisoning less than to 1%, θ_1 would need to stay below 0.4, which means the contaminant

concentration needs to stay below 10 ppm at 0.4 mg/cm^2. However, the total voltage loss

will continue to increase due to ionomer poisoning.

Figure 5.8 shows the rate of catalyst site poisoning during contamination (γ_{cc}), obtained by fitting the model to the experimental data as a function of φ. The results show that γ_{cc} increases with increasing contaminant concentration or decreasing Pt loading in the catalyst layer. As an example, the value of γ_{cc} increased from 0.35 to 0.73 as the concentration of 2,6-DAT increased from 64 to 256 ppm. Also γ_{cc} increased from 0.35 to 0.71 as the catalyst loading decreased from 0.4 to 0.1 mg/cm². The parameter values are fit to the following empirical expression, and shown as the dotted line in Figure 5.8.

$$\gamma_{cc} = 0.762(1 - e^{-0.202\varphi}) \qquad\qquad 5\text{-}13$$
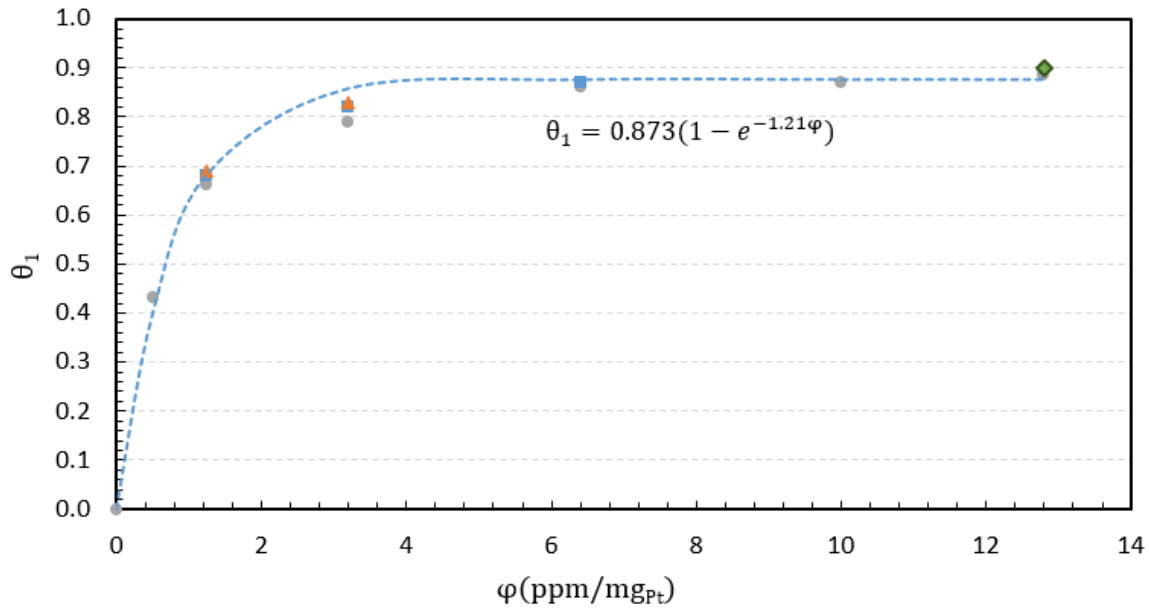
Figure 5.7. The fraction of sites poisoned during the contamination time (θ_1) for 2,6-DAT. The symbols correspond to the experimental conditions, given in Table 5.1 and the dotted line is the empirical fit to these parameter values (Equation 5-12).

It can be seen that γ_{cc} is higher for higher φ that suggests that the time required to reach steady state is shorter during contamination time for higher values of φ . Good

agreement was found with results of St-Pierre et al. [85] for their NO_2 contamination model.
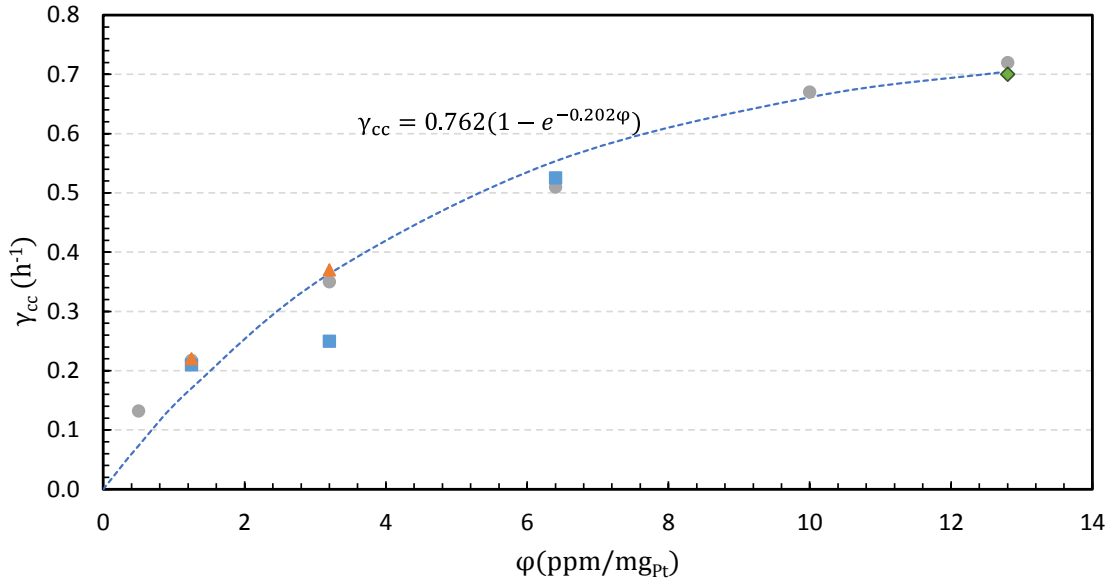
Figure 5.8. The rate of catalyst poisoning during the contamination time for 2,6-DAT. The symbols correspond to the experimental conditions, given in Table 5.1 and the dotted line is the empirical fit to these parameter values (Equation 5-13).

Figure 5.9 depicts the rate of ionomer poisoning in the catalyst layer during contamination (γ_{ic}) obtained by fitting the model to the experimental data as a function of φ. The data in Figure 5.9 is fit to the following linear relationship and shown as a dotted line in this figure.

$$\gamma_{ic} = 1.95 \times 10^{-3}\varphi \qquad \qquad 5\text{-}14$$

The parameter $\gamma_{i,c}$ increases as a function of φ, indicating an ion-exchange affinity of 2,6-DAT that is even more than observed for NH_4^+ [120]. As the sulfonic sites present in Nafion have a higher affinity for foreign cations than H^+, the presence of the impurity

105

cations decrease the proton concentration and in turn the conductivity of the polymer electrolyte [92].
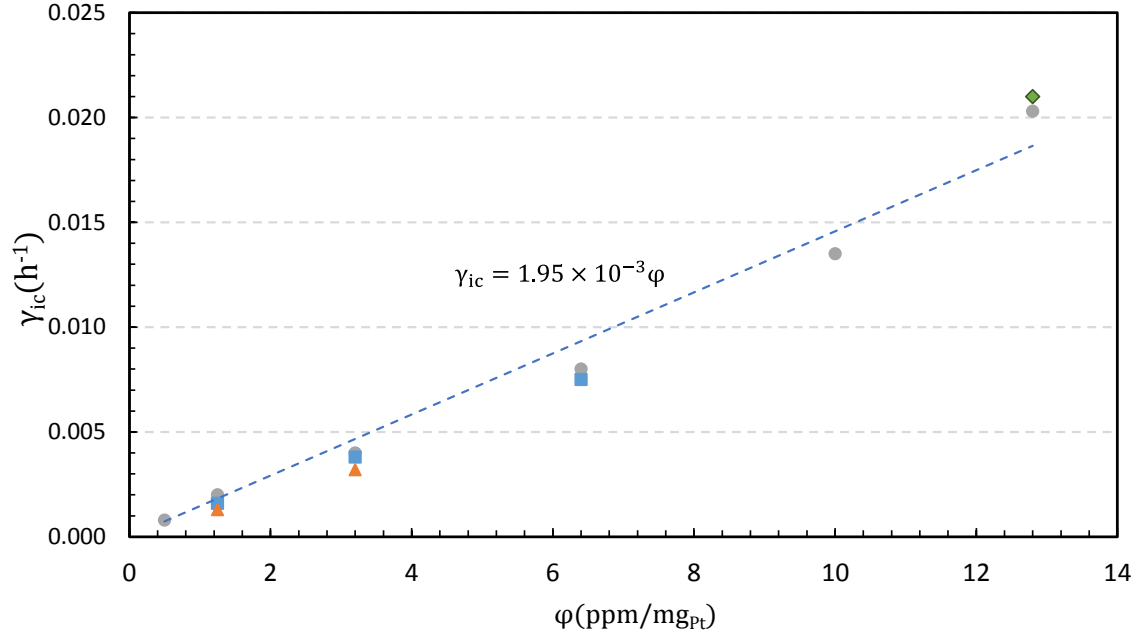
Figure 5.9. The rate of ionomer poisoning during contamination γ_{ic} with 2,6-DAT. The symbols correspond to the experimental conditions, given in Table 5.1 and the dotted line is the empirical fit to these parameter values (Equation 5-14).

The effect of all experimental conditions (i.e., concentrations, infusion times and cathode catalyst loadings) on model parameters (i.e., θ_2, γ_{cr}, γ_{ir}, and y_2) during the recovery are shown in Figures 5.10-5.13, respectively. The parameter values are fit to empirical expressions, resulting in Equations 5-15-5-18 and the dotted lines in Figures 5.10-5.13.

$$\theta_2 = 0.82(1 - e^{-3.92y_1}) \qquad\qquad 5\text{-}15$$

$$\gamma_{cr} = 0.032e^{3.74y_1} \qquad\qquad 5\text{-}16$$

$$\gamma_{ir} = -1.34y_1 + 0.98 \qquad\qquad 5\text{-}17$$

$$y_2 = 0.010e^{5.82y_1} \qquad\qquad 5\text{-}18$$

As discussed earlier, the only experimental condition that varies during recovery from Equation 5-8 is y_1, the fraction of contamination in the ionomer at catalyst layer at $t = t_1$. It is not surprising that we have more scattered for the correlation to y_1, as y_1 is an unknown parameter that is calculated after fitting the experimental data to the model equations. The amount of y_1 at different experimental conditions is shown in Table 5.1. For small values of y_1, most parts of the ionomer is recovered, therefore as y_1 is increased a lower percentage of recovery is observed. For example, for $y_1 = 0.024$, 90% of the contaminant in the ionomer is recovered while for $y_1 = 0.63$ less than 40% of y_1 is recovered. This low level of recovery (irreversibility) are consistent with previous studies [93, 121, 122], who showed the effect of NH_3 recovery can be both reversible and irreversible, depending on the NH_3 concentration and exposure time.
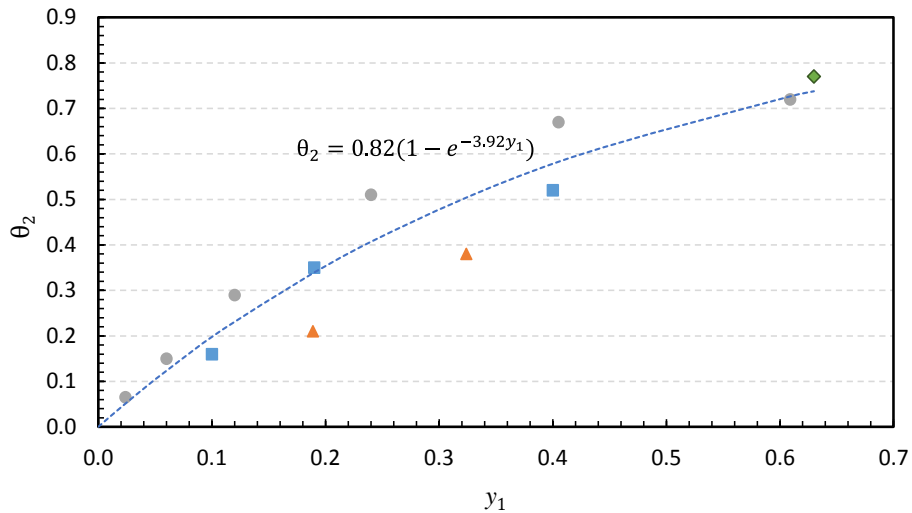
Figure 5.10. The fraction of sites poisoned during recovery (θ_2) with 2,6-DAT. The symbols correspond to the experimental conditions, given in Table 5.1 and the dotted line is the empirical fit to these parameter values (Equation 5.15).
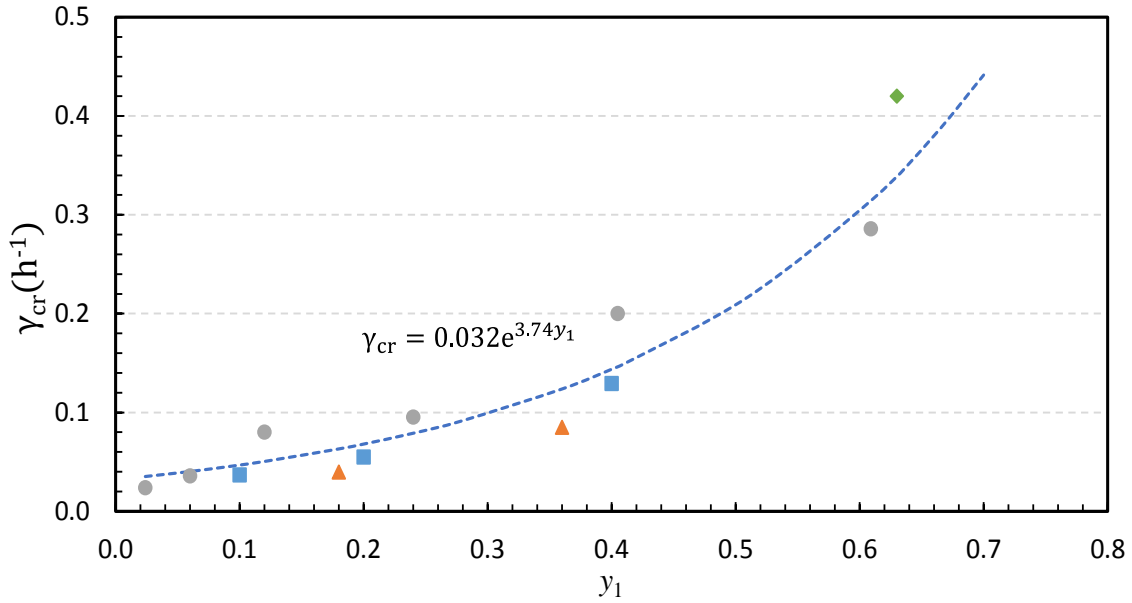
Figure 5.11. The rate of catalyst recovery during the recovery with 2,6-DAT. The symbols correspond to the experimental conditions, given in Table 5.1 and the dotted line is the empirical fit to these parameter values (Equation 5-16).

The equation shown in the figure:

$$\gamma_{cr} = 0.032e^{3.74y_1}$$
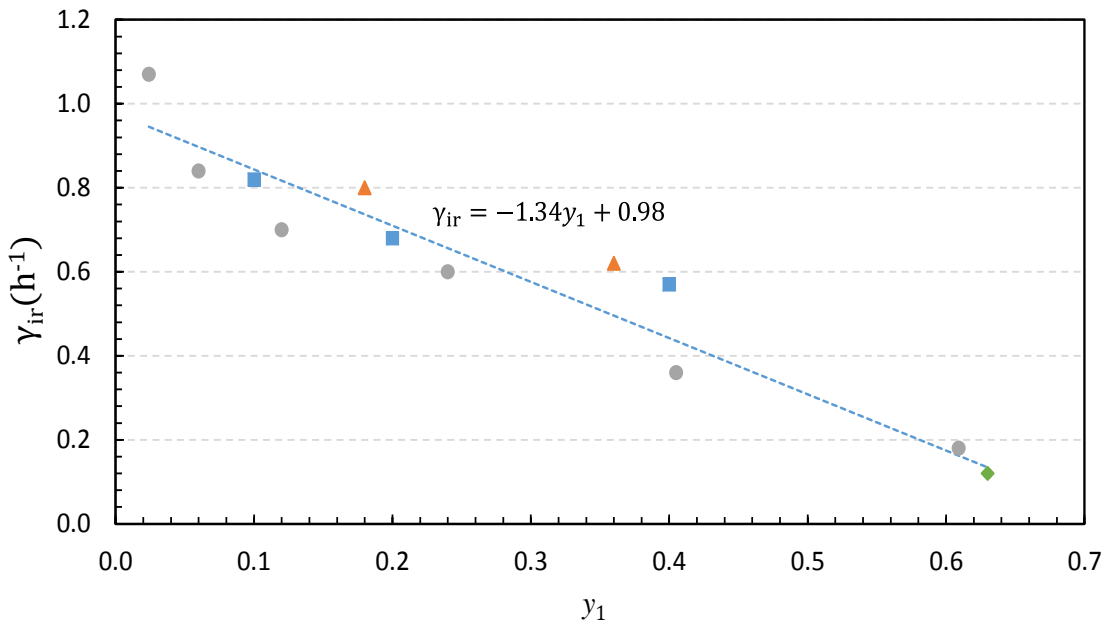
Figure 5.12. The rate of ionomer recovery during recovery (γ_{ir}) with 2,6-DAT. The symbols correspond to the experimental conditions, given in Table 5.1 and the dotted line is the empirical fit to these parameter values (Equation 5-17).

The equation shown in the figure:

$$\gamma_{ir} = -1.34y_1 + 0.98$$
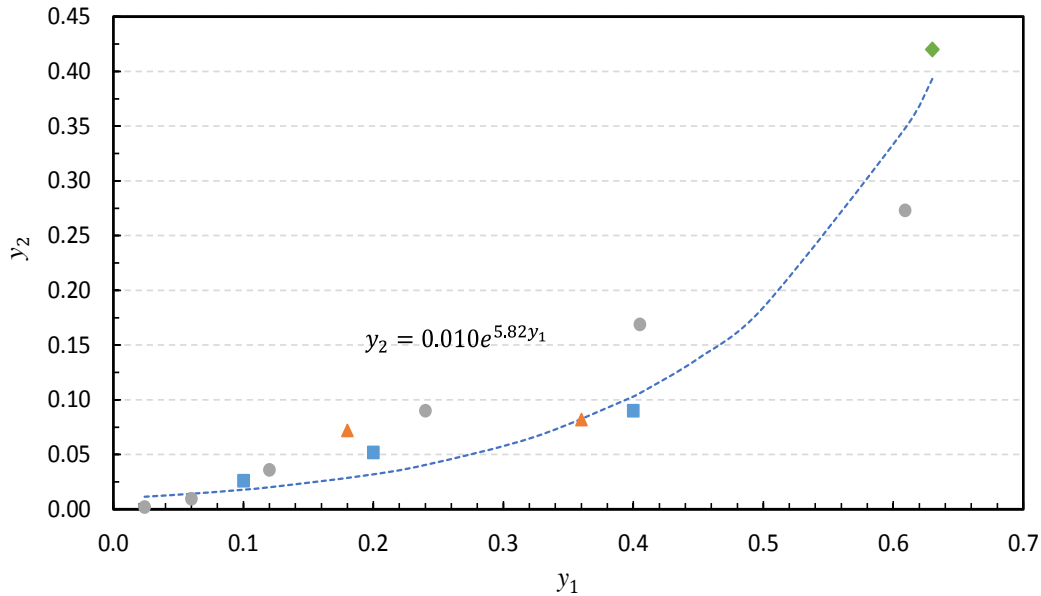
Figure 5-13. The fraction of contamination in the ionomer at steady state (y_2) for 2,6-DAT. The symbols correspond to the experimental conditions, given in Table 5.1 and the dotted line is the empirical fit to these parameter values (Equation 5-18).

Equations 5-12 through 5-18 show that for any concentration, infusion time and cathode catalyst loading, model parameters are obtainable and can be used to quantify the voltage loss and recovery of the fuel cell. Although the model parameters are assumed to be independent of current, the voltage loss and recovery are a function of current via Equation 5-5. Hence, the equation given here can be used to estimate the voltage loss as a function of current. It is cautioned through that the predicted parameters may change at high currents when large quantities of water are generated on the cathode side, influencing both contamination and recovery, and also a change in current density/cell voltage can also induce oxidation or reduction reactions.

5.5 Summary

The performance loss and recovery of a fuel cell due to BOP contaminants was identified via a combination of experimental data and a mathematical model. The impact

of parameters such concentration, infusion time, and catalyst loading of different compounds was studied. The model was designed to capture the effect of contamination adsorption onto the catalyst, and kinetic and ohmic losses caused by ion exchange with the ionomer. It was determined that the degree of contamination increased with an increase in both concentration and infusion time. The recovery tests revealed that cell performance was partially recoverable for 2,6-DAT, and for the other three compounds it was fully recoverable. This shows that the compounds with ion exchange properties have more of an effect on the non-reversible performance degradation. The parameters obtained by fitting the model to the data shows that the parameters are functions of the ratio of contaminant concentration to cathode catalyst loading during the contamination. The parameters during the recovery are functions of the fraction of contamination in the ionomer at the end of infusion (i.e. y_1 at $t = t_1$). Model parameters can be used to predict the various potential losses caused by contaminants during both fuel cell contamination and recovery operations.

REFERENCES

1. B. L. Garcia-Diaz, L. Olson, M. Martinez-Rodriguez, R. Fuentes, H. Colon-Mercado, *Journal of the South Carolina Academy of Science*, 14, 11 (2016).

2. S. M. Flueckiger, Z. Yang and S. V. Garimella, *Heat Transfer Engineering*, 34, 787 (2013).

3. R. Zidan, B. Hardy, C. Corgnale, J. Teprovich, B.Peters *Metal Hydride based Thermal Energy Storage Systems for Concentrating Solar Power Systems Theodore Motyka*, ASME 2014 8th International Conference on Energy Sustainability, Savannah River National Laboratory, 999-2W, Aiken, , Boston, MA (2014).

4. RENEWABLE ENERGY TECHNOLOGIES: COST ANALYSIS SERIES, *International Renewable Energy Agency (IRENA)* (June 2012).

5. http://www.innovation-america.org/how-boost-efficiency-solar-plants.

6. N. Lorenzin and A. Abanades, *International Journal of Hydrogen Energy*, XX, 1 (2016).

7. P. Kumar and M. Sharma, *International Journal of Engineering Research & Technology* (IJERT), 3, 1 (2014).

8. Heat transfer fluids: key to CSP success, in, CSP Today Editor (2013).

9. K. Vignarooban, X. H. Xu, A. Arvay, K. Hsu and A. M. Kannan, *Applied Energy*, 146, 383 (2015).

10. A. P. Fraas, *Heat Exchanger Design*, p. 551, John Wiley & Sons, Canada (1989).

11. http://energy.gov/sites/prod/files/2014/01/f7/csp_natl_lab_rd_fact_sheet.pdf (2016).

12. S. Kuravi, J. Trahan, D. Y. Goswami, M. M. Rahman and E. K. Stefanakos, *Progress in Energy and Combustion Science*, 39, 285 (2013).

13. F. Y. Ouyang, C. H. Chang, B. C. You, T. K. Yeh and J. J. Kai, *Journal of Nuclear Materials*, 437, 201 (2013).

14. 14. B. Tavakoli and R. Roshandel, Renewable Energy, 36, 3319 (2011).

15. http://physics.nist.gov/MajResFac/NIF/pemFuelCells.html, in (2016).

16. C. E. Tyner, J. Paul Sutherland, William R. Gould, *J. Solar Two: A Molten Salt Power Tower Demonstration*, (2000).

17. C.J. Li, Peiwen Li, Kai Wang, *Edgar Emir Molina AIMS Energy*, 2, 133 (2014).

18. U. Herrmann and D. W. Kearney, Journal of Solar Energy Engineering-Transactions of the Asme, 124, 145 (2002)

19. J. W. Raade and D. Padowitz, *Journal of Solar Energy Engineering-Transactions of the ASME*, 133 (2011).

20. J. C. Gomez, N. Calvet, A. K. Starace and G. C. Glatzmaier, *Journal of Solar Energy Engineering-Transactions of the ASME*, 135 (2013).

21. C. W. Forsberg, P. F. Peterson and H. H. Zhao, *Journal of Solar Energy Engineering-Transactions of the ASME*, 129, 141 (2007).

22. S. Piyush, Matt Ebner, Manohar Sohal, Phil SharpeMark Anderson, Kumar Sridharan, James Ambrosek, Luke Olson, Paul Brooks, *Molten Salts for High Temperature Reactors: University of Wisconsin Molten Salt Corrosion and Flow Loop Experiments – Issues Identified and Path Forward*, INL/EXT-10-18090, Idaho National Laboratory (2010).

23. D. F. Williams, Assessment of Candidate Molten Salt Coolants for the NGNP/NHI Heat-Transfer Loop, ORNL/TM-2006/69, OAK RIDGE NATIONAL LABORATORY (2006).

24. H. G. Frederic Lantelme, *Molten Salts Chemistry: From Lab to Applications*, Elsivier Inc, MA USA (2013).

25. J. Stringer, Mater Performance, 7, 1 (2004).

26. L. C. Olson, J. W. Ambrosek, K. Sridharan, M. H. Anderson and T. R. Allen, *Journal of Fluorine Chemistry*, 130, 67 (2009).

27. V.M. Azhazha, A. S. Bakai, S.D. Lavrinenko, Y.P. Bobrov, P.N. V'yugov, K.V. Kovtun, M.M. Pylypenko, V.I. Savchenko, A.D. Solopikhin, S.P. Stetsenko, D.G. Malykhin, *Problems of Atomic Science and Technology*, 40 (2005).

28. D. E. Clark, R. E. Mizia, M. V. Glazoff, P. Sabharwall, M. G. McKellar, Diffusion welding of alloys for molten salt service – status Report, in, INL/EXT-12-24589 Editor, U.S. Department of Energy, Idaho National Laboratory (2012).

29. J. R. Davis, ASME Specialty Handbook, *Stainless steels, ASM International* (1999).

30. A. Nishikata, H. Numata and T. Tsuru, *Materials Science and Engineering a-Structural Materials Properties Microstructure and Processing*, 146, 15 (1991).

31. I. N. Ozeryanaya, *Metal Science and Heat Treatment*, 27, 184 (1985).

32. S. Fabre, C. Cabet, L. Cassayre, P. Chamelot, S. Delepech, J. Finne, L. Massot and D. Noel, *Journal of Nuclear Materials*, 441, 583 (2013).

33. M. Kondo, T. Nagasaka, V. Tsisar, A. Sagara, T. Muroga, T. Watanabe, T. Oshima, Y. Yokoyama, H. Miyamoto, E. Nakamura and N. Fujii, *Fusion Engineering and Design*, 85, 1430 (2010).

34. L. C. Olson, *Materials Corrosion in Molten LiF-NaF-KF Eutectic Salt*, Nuclear Engineering, University of Wisconsin-Madison (2009).

35. X. Chen, X. G. Li, C. W. Du and Y. F. Cheng, *Corrosion Science*, 51, 2242 (2009).

36. B. Saleem, F. Ahmed, M. A. Rafiq, M. Ajmal and L. Ali, *Engineering Failure Analysis*, 46, 157 (2014).

37. P. R. Roberge, *Corrosion Engineering*, McGraw-Hill Companies (2008).

38. R. Montoya, O. Rendon and J. Genesca, *Materials and Corrosion-Werkstoffe Und Korrosion*, 56, 404 (2005).

39. L. K. Matson, E. F. Stephan, P. D. Miller, W. K. Boyd and R. P. Milford, *Corrosion*, 22, 194 (1966).

40. B. L. Garcia-Diaz, L. Olson, M. Martinez-Rodriguez, R. Fuentes, H. Colon-Mercado, *Journal of the South Carolina Academy of Science*, 14, 11 (2016).

41. S. S. Pathak, S. K. Mendon, M. D. Blanton and J. W. Rawlins, *Metals*, 2, 353 (2012).

42. D. Williams, L. Toth and K. Clarno, *Assessment of Candidate Molten Salt Coolants for the Advanced High-Temperature Reactor (AHTR)*, p. 1, Oak Ridge National Laboratory, Oak Ridge, Tennessee (2006).

43. A. Garcia-Cruz, M. Lee, N. Zine, M. Sigaud, J. Bausells and A. Errachid, *Sensors and Actuators B-Chemical*, 221, 940 (2015).

44. Y. F. Yin and R. G. Faulkner, *Corrosion Science*, 49, 2177 (2007).

45. T. Thorvaldsson and G. L. Dunlop, *Journal of Materials Science*, 18, 793 (1983).

46. A. Anderko, N. Sridhar and G. Tormoen, *Corrosion Engineering Science and Technology*, 45, 204 (2010).

47. M. S. Sohal, M. A. Ebner, P. Sabharwall and P. Sharpe*, Engineering Database of Liquid Salt Thermophysical and Thermochemical Properties*, INL/EXT-10-18297 (March 2010).

48. D. F. Williams, L. M. Toth and K. T. Clarno, *Assessment of candidate molten salt coolant for the advanced high temperature reactor*, ORNL/TM-2006/12 Editor (March 2006).

49. L. Olson, R. Fuentes, M. Martinez-Rodriguez, B. Garcia-Diaz and J. Gray, *American Nuclear Society, Reno, Nevada* (June 15–19, 2014).

50. P. R. Roberge, *Corrosion Engineering [Principles and Practice]*,

McGraw-Hill Companies, New York (2008).

51. L. C. Olson, R. E. Fuentes, M. J. Martinez-Rodriguez, J. W. Ambrosek, K. Sridharan, M. H. Anderson, B. L. Garcia-Diaz, J. Gray and T. R. Allen, *Journal of Solar Energy Engineering-Transactions of the ASME*, 137 (2015).

52. L. Olson, K. Sridharan, M. Anderson and T. Allen, *Materials at High Temperatures*, 27, 145 (2010).

53. Y. L. Wang, H. J. Liu and C. L. Zeng, *Journal of Fluorine Chemistry*, 165, 1 (2014).

54. Y. L. Wang, H. J. Liu, G. J. Yu, J. Hou and C. L. Zeng, *Journal of Fluorine Chemistry*, 178, 14 (2015).

55. S. I. Choi, S. F. Xie, M. H. Shao, J. H. Odell, N. Lu, H. C. Peng, L. Protsailo, S. Guerrero, J. H. Park, X. H. Xia, J. G. Wang, M. J. Kim and Y. N. Xia, *Nano Letters*, 13, 3420 (2013).

56. D. Ludwig, L. Olson, K. Sridharan, M. Anderson and T. Allen, *Corrosion Engineering Science and Technology*, 46, 360 (2011).

57. H.S. Cho, J. W. Van Zee, S. Shimpalee, B. A. Tavakoli, J. W. Weidner, B. L. Garcia-Diaz, M.J. Martinez-Rodriguez, L.Olson and J. Gray, *Corrosion*,72, 742 (2016).

58. J. W. A. Misra, Fluoride Salts and Container Materials for Thermal Energy Storage Applications in the Temperature Range 973 to 1400 K, in Jama-*Journal of the American Medical Association*, p. 16, National Aeronautics and Space Administration, Lewis Research Center, Cleveland, Ohio, National Aeronautics and Space Administration, Lewis Research Center, Cleveland, Ohio (1987).

59. M. S. Venkatraman, I. S. Cole and B. Emmanuel, *Electrochimica Acta*, 56, 7171 (2011).

60. A. J. Bard, L. R. Faulkner, *Electrochemical methods fundamentals to applications*, p. 96, John Wiley &Sons, Inc., New York (1980).

61. J. Newman, K. E. Thomas-Alyea, *Electrochemical Systems*, p. 377, John Wiley& Sons, New Jersey (2004).

62. M. Ebner and V. Wood, *Journal of the Electrochemical Society*, 162, A3064 (2015).

63. J. C.M. Li, *Microstructure and Properties of Materials*, World scientific, New Jersey (2000).

64. D. W. Chung, M. Ebner, D. R. Ely, V. Wood and R. E. Garcia, *Modelling and Simulation in Materials Science and Engineering*, 21 (2013).

65. J. Newman, K. E. Thomas-Alyea, *Electrochemical Systems*, p. 4, John Wiley& Sons, New Jersey (2004).

66. J. Hu, P.C. Sui, N. Djilali, and S. Kumar, *ECS Transaction*, 16, 1313 (2008).

67. F. Lantelme and H. Groult, *Molten Salts Chemistry: From Lab to Applications*, Xvii (2013).

68. J. Stekli, L. Irwin and R. Pitchumani, *Journal of Thermal Science and Engineering Applications*, 5 (2013).

69. G. T. Parthiban, T. Parthiban, R. Ravi, V. Saraswathy, N. Palaniswamy and V. Sivan, *Corrosion Science*, 50, 3329 (2008).

70. B. A. Tavakoli Mehrabadi, J. W. Wiedner, Brenda Garcia-Diaz, and L. O. Michael Martinez-Rodriguez, and Sirivatch Shimpalee, *Journal of the Electrochemical Society*, 163, C830 (2016).

71. B. A. Tavakoli Mehrabadi, J. W. Weidner, B. Garcia-Diaz and a. L. O. M. Martinez-Rodriguez, *ECS Transactions*, 72, 151 (2016).

72. R. Mohtadi, W. K. Lee and J. W. Van Zee, *J Power Sources*, 138, 216 (2004).

73. D. J. Yang, J. X. Ma, L. Xu, M. Z. Wu and H. J. Wang, *Electrochim Acta*, 51, 4039 (2006).

74. J. M. Moore, P. L. Adcock, J. B. Lakeman and G. O. Mepsted, *J Power Sources*, 85, 254 (2000).

75. Z. Shi, D. T. Song, H. Li, K. Fatih, Y. H. Tang, J. L. Zhang, Z. W. Wang, S. H. Wu, Z. S. Liu, H. J. Wang and J. J. Zhang, *Journal of Power Sources*, 186, 435 (2009).

76. Y. Zhai, G. Bender, K. Bethune and R. Rocheleau, *J Power Sources*, 247, 40 (2014).

77. Y. Zhai, G. Bender, S. Dorn and R. Rocheleau, *Journal of the Electrochemical Society*, 157, B20 (2010).

78. Y. Zhai and J. St-Pierre, *J Power Sources*, 279, 165 (2015).

79. X. Cheng, Z. Shi, N. Glass, L. Zhang, J. J. Zhang, D. T. Song, Z. S. Liu, H. J. Wang and J. Shen, *Journal of Power Sources*, 165, 739 (2007).

80. G. Bender, M. Angelo, K. Bethune and R. Rocheleau, *Journal of Power Sources*, 228, 159 (2013).

81. A. A. Shah and F. C. Walsh, *Journal of Power Sources*, 185, 287 (2008).

82. R. Halseid, P. J. S. Vie and R. Tunold, *Journal of Power Sources*, 154, 343 (2006).

83. X. Y. Zhang, U. Pasaogullari and T. Molter, *International Journal of Hydrogen Energy*, 34, 9188 (2009).

84. X. Z. Yuan, H. Li, Y. Yu, M. Jiang, W. M. Qian, S. S. Zhang, H. J. Wang, S. Wessel and T. T. H. Cheng, *International Journal of Hydrogen Energy*, 37, 12464 (2012).

85. J. St-Pierre, N. Jia and R. Rahmani, *Journal of the Electrochemical Society*, 155, B315 (2008).

86. F. N. Jing, M. Hou, W. Y. Shi, J. Fu, H. M. Yu, P. W. Ming and B. L. Yi, *Journal of Power Sources*, 166, 172 (2007).

87. Y. Zhai, K. Bethune, G. Bender and R. Rocheleau, *Journal of the Electrochemical Society*, 159, B524 (2012).

88. Y. Garsany, O. A. Baturina and K. E. Swider-Lyons, *Journal of the Electrochemical Society*, 154, B670 (2007).

89. H. Li, J. L. Zhang, K. Fatih, Z. W. Wang, Y. H. Tang, Z. Shi, S. H. Wu, D. T. Song, J. J. Zhang, N. Y. Jia, S. Wessel, R. Abouatallah and N. Joos, *Journal of Power Sources*, 185, 272 (2008).

90. J. St-Pierre, *Journal of the Electrochemical Society*, 156, B291 (2009).

91. J. St-Pierre, *Journal of Power Sources*, 195, 6379 (2010).

92. J. St-Pierre, *International Journal of Hydrogen Energy*, 36, 5527 (2011).

93. J. St-Pierre, *Journal of Power Sources*, 196, 6274 (2011).

94. R. Mohtadi, W. K. Lee, S. Cowan, J. W. Van Zee and M. Murthy, *Electrochemical and Solid State Letters*, 6, A272 (2003).

95. X. Y. Zhang, M. F. Serincan, U. Pasaogullari and T. Molter, *Proton Exchange Membrane Fuel Cells* 9, 25, 1565 (2009).

96. B. L. Kienitz, H. Baskaran and T. A. Zawodzinski, *Electrochimica Acta*, 54, 1671 (2009).

97. A. Z. Weber and C. Delacourt, *Fuel Cells*, 8, 459 (2008).

98. H. L. Wang, J. Christ, C. S. Macomber, K. O'Neill, K. C. Neyerlin, K. A. O'Leary, R. Reid, B. Lakshmanan, M. Das, M. Ohashi, J. W. Van Zee and H. N. Dinh, *Abstracts of Papers of the American Chemical Society*, 243 (2012).

99. H. S. Cho, M. Das, M. S. Opu, M. Ohashi and J. W. Van Zee, *Journal of the Electrochemical Society*, 162, F1056 (2015).

100. H.S. Cho, M. Jung, J. Navarro, M. Ohashi and J.W. Van Zee, *ECS Transaction*, 33, 1487 (2010).

101. J. M. Christ, K. C. Neyerlin, R. Richards and H. N. Dinh, *Journal of the Electrochemical Society*, 161, F1360 (2014).

102. P. T. Yu, E. A. Bonn and B. Lakshmanan, *Polymer Electrolyte Fuel Cells 13 (Pefc 13)*, 58, 665 (2013).

103. H. L. Wang, C. Macomber, J. Christ, G. Bender, B. Pivovar and H. N. Dinh, *Electrocatalysis*, 5, 62 (2014).

104. J. M. Christ, K. C. Neyerlin, H. L. Wang, R. Richards and H. N. Dinh, *Journal of the Electrochemical Society*, 161, F1481 (2014).

105. M. Opu, G. Bender, C. S. Macomber, J. W. Van Zee and H. N. Dinh, *Journal of the Electrochemical Society*, 162, F1011 (2015).

106. H. S. Cho and J. W. Van Zee, *Journal of the Electrochemical Society*, 161, F1375 (2014).

107. C. S. Macomber, H. L. Wang, K. O'Neill, S. Coombs, G. Bender, B. Pivovar and H. N. Dinh, *Polymer Electrolyte Fuel Cells 10*, Pts 1 and 2, 33, 1637 (2010).

108. T. Okada, Y. Ayato, H. Satou, M. Yuasa and I. Sekine, *Journal of Physical Chemistry B*, 105, 6980 (2001).

109. T. Okada, H. Satou and M. Yuasa, *Langmui*r, 19, 2325 (2003).

110. J. J. Ge, J. St-Pierre and Y. F. Zhai, *Electrochimica Acta*, 134, 272 (2014).

111. J. J. Ge, J. St-Pierre and Y. F. Zhai, *Electrochimica Acta*, 138, 437 (2014).

112. J. J. Ge, J. St-Pierre and Y. F. Zhai, *International Journal of Hydrogen Energy*, 39, 18351 (2014).

113. J. J. Ge, J. St-Pierre and Y. F. Zhai, *Electrochimica Acta*, 133, 65 (2014).

114. H. Li, Z. Shi, J. W. Van Zee and J. Zhang, *Proton Exchange Membrane Fuel Cells Contamination and Mitigation Strategies*, Taylor and Francis Group, New York (2010).

115. D.B. Sepa, M.V. Vojnovic and A. Damjanovic, *Electrochemica Acta*, 26, 781 (1981).

116. K. Hongsirikarn, X. H. Mo, Z. M. Liu and J. G. Goodwin, *Journal of Power Sources*, 195, 5493 (2010).

117. K. Hongsirikarn, X. H. Mo and J. G. Goodwin, *Journal of Power Sources*, 195, 3416 (2010).

118. Y. F. Zhai, O. Baturina, D. Rarnaker, E. Farquhar, J. St-Pierre and K. Swider-Lyons, *Journal of Physical Chemistry C*, 119, 20328 (2015).

119. J. St-Pierre, Y. F. Zhai and M. S. Angelo, *Journal of the Electrochemical Society*, 161, F280 (2014).

120. H. S. Cho, M. Das, H. L. Wang, H. N. Dinh and J. W. Van Zee, *Journal of the Electrochemical Society*, 162, F427 (2015).

121. R. Borup, J. Meyers, B. Pivovar, Y. S. Kim, R. Mukundan, N. Garland, D. Myers, M. Wilson, F. Garzon, D. Wood, P. Zelenay, K. More, K. Stroh, T. Zawodzinski, J. Boncella, J. E. McGrath, M. Inaba, K. Miyatake, M. Hori, K. Ota, Z. Ogumi, S. Miyata, A. Nishikata, Z. Siroma, Y. Uchimoto, K. Yasuda, K. I. Kimijima and N. Iwashita, *Chemical Reviews*, 107, 3904 (2007).

122. F. A. Uribe, S. Gottesfeld and T. A. Zawodzinski, *Journal of the Electrochemical Society*, 149, A293 (2002).

123. B. L. Garcia-Diaz, *Fundamental Corrosion Studies in High-Temperature Molten Salt Systems for Next Generation Concentrated Solar Power Systems, Q1, Q2, Q3 & Q4 FY2015 Research Performance Progress Reports*, Savannah River National Laboratory (2015).

124. B. L. Garcia-Diaz, L.C. Olson, M. Martinez-Rodriguez, R.E. and J. R. G. Fuentes, *Electrochemical Study of Corrosion in High Temperature Molten Salts*, paper no. 741, in 2014 ECS and SMEQ Joint International Meeting, Pennington, NJ (2014).

125. E. A. Loria, *Journal of Metals*, 34, 16 (1982).

126. Y. M. Pan, D. S. Dunn, G. A. Cragnolino and N. Sridhar, *Metallurgical and Materials Transactions a-Physical Metallurgy and Materials Science*, 31, 1163 (2000).

127. J. H. Park, J. K. Kim, B. H. Lee, S. S. Kim and K. Y. Kim, *Scripta Materialia*, 68, 237 (2013).

128. B. S. Kumar, B. S. Prasad, V. Kain and J. Reddy, *Corrosion Science*, 70, 55 (2013).

129. CD-adapco, pro-STAR COMMANDS (VERSION 3.26), p. 1 (2005).

APPENDIX A. EXPERIMENTAL SETUP

A.1 Thermosiphon Experiments

The geometry that are used in this thesis is according to the thermosiphon apparatus designed at SRNL for studying the transports and corrosion phenomenon inside high temperature molten salt systems. This thermosiphon unit mainly consists of Nickel crucible (housing), Nickel crucible insert for holding the samples, Stainless steel thermal mass to product temperature gradient for the system, and 4 coupons, which are located at the top and bottom of the thermosiphon. Figure A.1 shows the detail component of the thermosiphon. Figure A.1 (b) shows a sketch of the corrosion cells used for the molten salt immersion experiments [123].

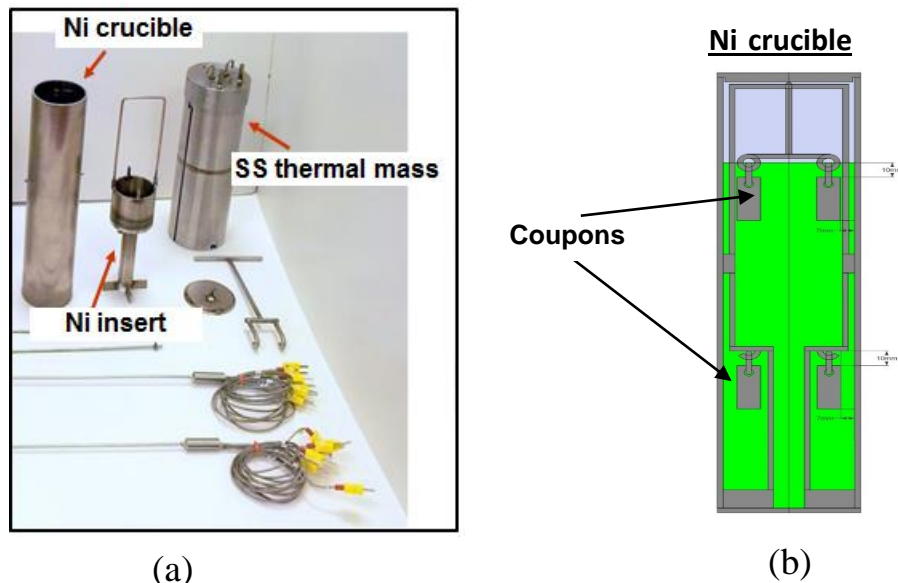(a)   (b)

Figure A.1 (a) Major components of thermosiphon, (b) a sketch of the corrosion cells [123].

The set of six-thermocouple probe was placed at near wall of the Ni vessel and in the center of Ni Crucible insert. Therefore there are twelve thermocouples measured in the experiment. For heating the thermosiphon, a three zone PID controlled tube furnace are used. Screw jack are used to raise or lower the thermosiphon vessel into or out of furnace, large thermal mass on top that was water cooled.

(a)

Two temperature probes will be used for initial characterization, but will be removed for actual corrosion tests

An O-ring sealed endcap with water cooling is used to maintain Argon atmosphere inside quartz tube

If needed, water or gas cooling can be applied directly to the inner cooling sleeve. Passive air cooling is preferred.

Thermosiphon assembly sits inside quartz tube

1,200°C max, 3,100 W, 3 zone tube furnace

Screw jack can be moved up and down to better position thermosiphon in furnace

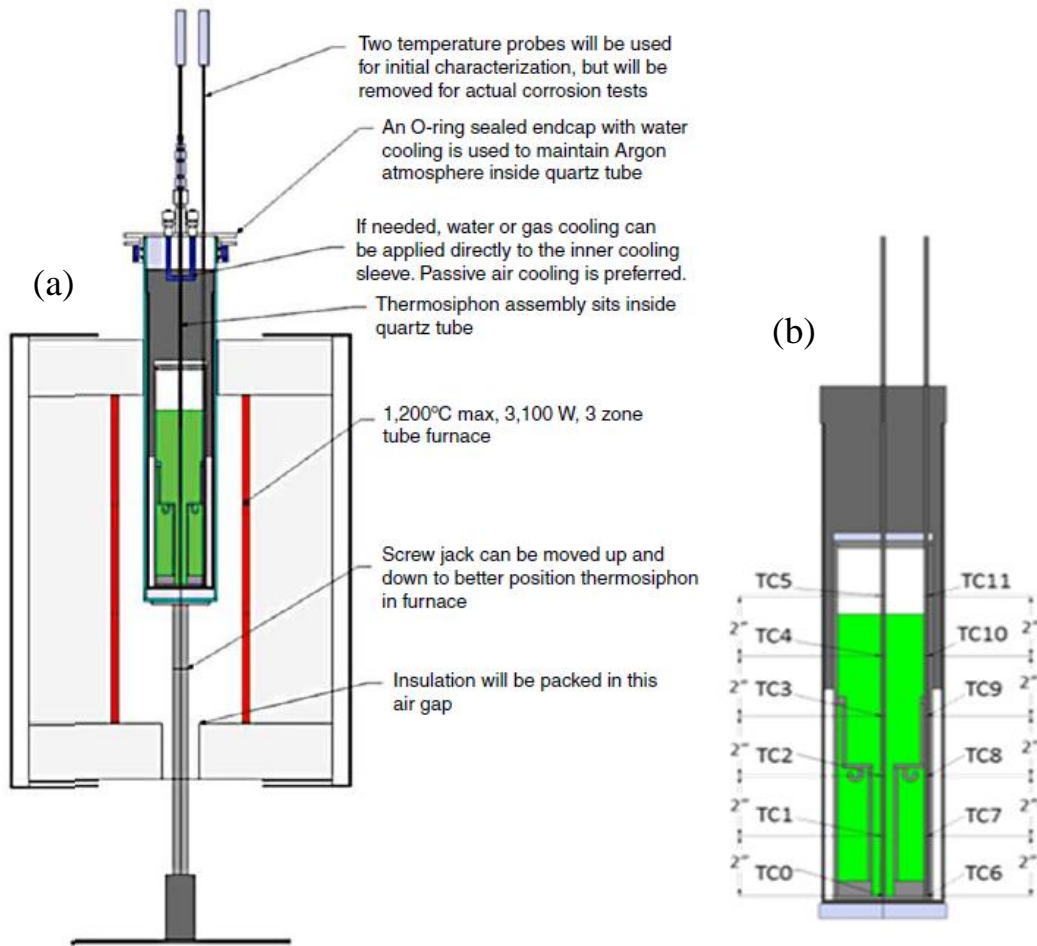Insulation will be packed in this air gap

(b)

Figure A.2 Schematic of a thermosiphon equipped in a furnace [123].

Samples for the thermosiphon were cut from sheet procured from the metal vendor (Haynes International for the N06230) that was delivered in a 16 gauge sheet (~1.5 mm

thick) nominally 30.48 cm × 30.48 cm, ASTM grain size of 5. These samples were cut to the size of 1.19 cm × 2.61 cm × 0.15 cm, and were polished to a 1-µm finish with diamond paste slurry. The samples were cleaned and degreased using deionized water followed by ethanol and dried under compressed air, after which they were stored in a vacuum desiccator until they were used. The nominal physical dimensions of the samples were measured using standard calipers, and the masses were measured using a Sartorius laboratory analytical balance. The samples were hung in the thermosiphon reactor at the locations indicated in Figures A.2 (b), and the temperature measurements of the salt in various positions of the reactor are shown in Figure A.2 (b). The molten salt mixture was added sequentially to the reactor so that it could be melted down into a continuous electrolyte media from the discrete pieces that were added to the reactor. When the entire salt media was added to the reactor, the reactor was brought to the final temperature and the experiment was begun. At the end of the exposure period, the reactor heating was turned off and the contents were allowed to cool to room temperature. Afterward, the samples were broken out of the condensed salt media and cleaned for analysis. A sample of the salt was saved for analysis as well. The primary post-experimental measurements were the mass loss and change in physical dimensions using the analytical balance and calipers measurements, respectively. These measurements were used to calculate the corrosion rate as described in Equations (A-1) through (A-3). Selected samples were also subjected to SEM and EDS analysis.

$$i_{corr} = \frac{W_L}{A_a t} \frac{nF}{MW_{Alloy}} \qquad \text{A-1}$$

121

The average molecular weight is the weighted average of the oxidized species.

$$MW_{Alloy} = \sum_j x_j MW_j$$

A-2

Corrosion rate in terms of corrosion current density is expressed as:

$$Corrosion\ rate\ [\frac{g}{cm^2.s}] = \frac{W_L}{A_a t} = \frac{MW_{Alloy}}{nF} i_{corr}$$

A-3

As an example Table A.1 shows the dimension and mass of the coupons for three different alloys (i.e., Haynes 230, Haynes NS-163 and Incoloy 800H) at high temperature thermosiphon for 100 hours test. Figure A.3 and A.4 show the SEM analysis of Haynes 230 before and after 100 hours corrosion tests and Table A.2 and A.3 show EDS analysis of Haynes 230 before and after 100 hours corrosion tests respectively [123].

Table A.1. The dimension and mass of the coupons for three different alloys (i.e., Haynes 230, Haynes NS-163 and Incoloy 800H) at high temperature thermosiphon for 100 hours test.

Description	Sample ID	Before					After				
		Dimensions [59]			area (mm²)	mass (g)	Dimensions [59]			area (mm²)	mass (g)
		L	W	T			L	W	T		
800H	H5	29.51	12.09	1.22	8.05	3.28	29.51	11.98	1.20	7.97	3.04
	H6	29.67	12.08	1.18	8.05	3.18	29.64	11.99	1.27	8.07	2.92
	H7	29.87	12.1	1.19	8.13	3.28	29.78	11.98	1.27	8.10	3.20
	H8	29.51	12.06	1.24	8.05	3.32	29.51	12.03	1.26	8.05	3.25
NS-163	NS5	29.98	12.11	1.28	8.25	3.61	30.02	12.03	1.28	8.21	3.50
	NS6	30	12.05	1.31	8.25	3.62	30.07	11.98	1.27	8.18	3.49
	NS7	30.01	12.01	1.31	8.22	3.60	30.03	12.02	1.33	8.25	3.57
	NS8	30.09	12.06	1.28	8.25	3.62	30.09	12.08	1.36	8.34	3.59
Haynes 230	S5	30.06	12.04	1.52	8.46	4.72	29.97	12.00	1.51	8.40	4.69
	S6	30	11.97	1.5	8.38	4.71	29.99	12.02	1.52	8.43	4.68
	S7	30.09	11.98	1.49	8.40	4.74	30.05	12.00	1.55	8.46	4.73
	S8	30.08	12.14	1.49	8.50	4.72	30.01	12.03	1.54	8.46	4.70

Table A.2 EDS analysis of Haynes 230 before corrosion testing.

Element	Weight%	Atomic%
Al	0.26	0.60
Si	0.13	0.29
Cr	22.67	27.55
Mn	0.55	0.63
Fe	1.19	1.34
Co	0.45	0.48
Ni	58.74	63.22
Mo	1.23	0.81
W	14.79	5.08
Totals	100.00	

Table A.3. EDS analysis of Haynes 230 after 100 hours corrosion testing.

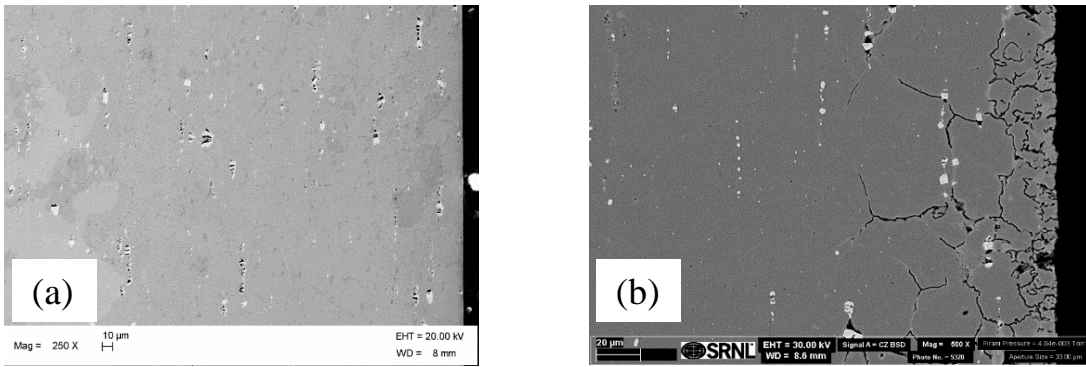| Element	Weight%	Atomic%
Al	1.31	3.00
Cr	2.14	2.54
Fe	1.04	1.15
Ni	85.55	89.97
W	9.95	3.34
Totals	100.00	

Figure A.3 (a) SEM analysis of Haynes 230 before corrosion testing, and (b) after 100 hours corrosion testing [123].

The sample showed significant erosion at the grain boundaries. The regions that were not eroded have a high Ni content. These areas also have Cr contents around 6-8% that are significantly lower than the 27% in the alloy before the corrosion testing. The selective depletion of Cr in the alloy has been cited in other studies as the principle mechanism of corrosion in alloys with molten salts. A cross-sectional SEM of the corroded sample was used to visualize the corrosion beneath the sample surface along with an EDS line scan to see the change in composition from the bulk of the material into the corroded region at the sample surface Figure A.4 (a) shows the subsurface microstructure of the corroded sample. The corrosion appears to occur first at grain boundaries in the alloy and appears to penetrate the deepest along these grain boundaries. At the surface the corrosion appears to have corroded a large portion of the material even from the bulk of the material. Figure A.4 (b) shows the concentration of the elements along the EDS line scan [123].

The area with significant corrosion showed a decrease in the Cr concentration and a corresponding increase in the Ni concentration. At the surface of the sample, the concentration of Ni was above 80% and appeared to approach being 100% Ni. To better

124

illustrate the erosion of Cr from the sample surface, EDS maps of Ni and Cr were made and overlaid in different colors to illustrate the selective depletion of Cr [123].
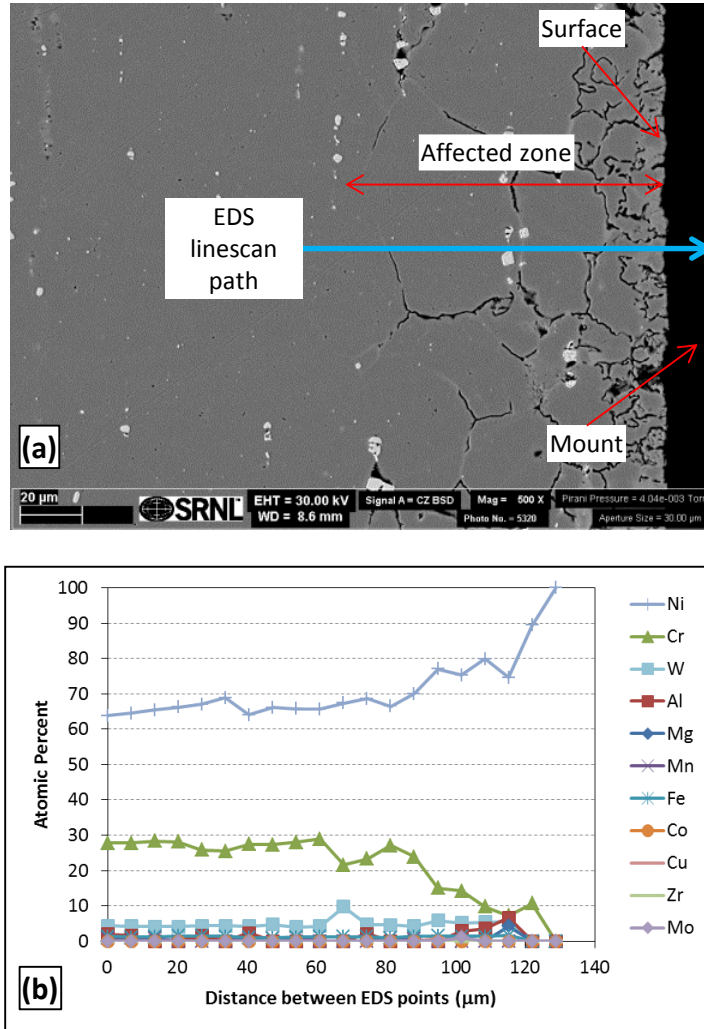

Figure A.4 (a) SEM cross-section image of Haynes 230 after 100 hours in KCl-MgCl$_2$ at 850°C and (b) results of EDS linescan (the last 2 - 4 EDS points of the linescans may be of the mounting material) [123].

A.2 Temperature Conditions

A thermosiphon was designed to test the exposure of metal coupons to both the isothermal and the non-isothermal conditions. There are three isothermal cases where the temperatures were kept constant in the system at 750, 850, and 950 °C and due to the

constant temperature, there is no fluid flow in the system. There are also two non-isothermal conditions where there are temperature gradients inside the thermosiphon (i.e., non-isothermal conditions with temperature gradient of 600-850 °C and 800-950 °C around the coupons) which the fluid flow circulates by natural convection due to changes in the molten salt's properties between the top and bottom of the thermosiphon. Figure A.4 shows a sketch of the thermosiphon used for corrosion measurements. The thermosiphon has four coupons placed in both the bottom and the top that were called the hot and cold zones respectively for the non-isothermal conditions. These regions are shown in Figure A.4. For the non-isothermal conditions, hot and cold zones were attained by inserting the bottom of the thermosiphon into a furnace, with the top either in an insulated region or partially out of the furnace. Table A.4 shows the different operational conditions for the experimental measurements.

Table A.4. Different operational conditions for the experimental measurements.

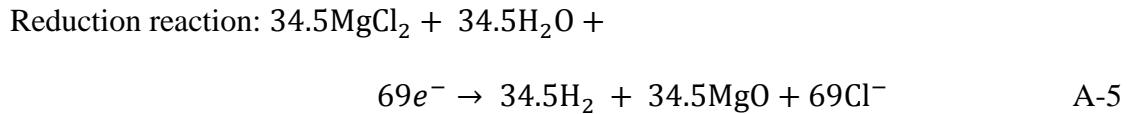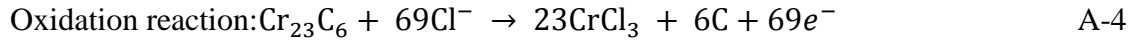| Temperature (°C)		Average temperature (°C)
750		750
850		850
950		950
650-800	(Cold zone)	738
	(Hot zone)	760
800-950	(Cold zone)	908
	(Hot zone)	926

A.3 Corrosion Reactions

For corrosion modeling, a diffusion-limited corrosion mechanism that was identified in previous electrochemical analyses coupled with SEM/EDS studies of the Ni alloy (Haynes 230) [124] is incorporated into the model. The SEM/EDS images in Figure A.4 show the
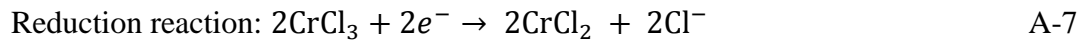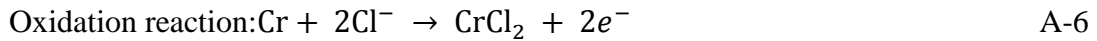
effect of immersing Haynes 230 in KCl-MgCl$_2$ for 100 h at 850°C. These image showed Cr depletion at the surface and along grain boundaries, and other studies have also reported the chromium selective oxidation along grain boundaries [125-128]. The corrosion model developed in this study includes the Cr oxidation reactions at the surface and along with grain boundaries.

The following initiation reactions and the reduction reaction of the propagation are assumed and used in the model:
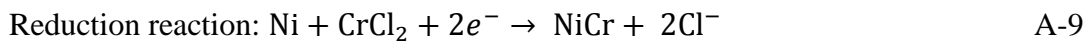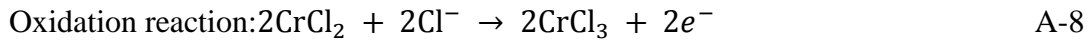
Initial reactions:

$$\text{Oxidation reaction:} Cr_{23}C_6 + 69Cl^- \rightarrow 23CrCl_3 + 6C + 69e^- \qquad \text{A-4}$$

$$\text{Reduction reaction: } 34.5MgCl_2 + 34.5H_2O +$$

$$69e^- \rightarrow 34.5H_2 + 34.5MgO + 69Cl^- \qquad \text{A-5}$$

Propagation (alloy and salts)

$$\text{Oxidation reaction:} Cr + 2Cl^- \rightarrow CrCl_2 + 2e^- \qquad \text{A-6}$$

$$\text{Reduction reaction: } 2CrCl_3 + 2e^- \rightarrow 2CrCl_2 + 2Cl^- \qquad \text{A-7}$$

Disproportionation (Crucible)

$$\text{Oxidation reaction:} 2CrCl_2 + 2Cl^- \rightarrow 2CrCl_3 + 2e^- \qquad \text{A-8}$$

$$\text{Reduction reaction: } Ni + CrCl_2 + 2e^- \rightarrow NiCr + 2Cl^- \qquad \text{A-9}$$

Note that the Cr (22.08 wt%) oxidation reaction was chosen mainly for the model prediction resulting from the lower Mn (0.52 wt%) composition of the Haynes 230 (i.e., Table A.3)

APPENDIX B. MODEL PARAMETERS

B.1 Introduction

Some of the parameters in the model were adjusted to fit the experimental data. This appendix shows the calculation of the kinetic parameters as a function of temperature.

For the redox reaction as:

$$O + ne^- \leftrightharpoons R \qquad \text{B-1}$$

the macroscopic relationship between the current density and the surface overpotential and the composition adjacent to the electrode can be written as Equation B-2.

$$i = f(\eta_s, c_i) \qquad \text{B-2}$$

The current-overpotential equation can be used for this relationship as is shown in Equation A-3:

$$i = i_0 \left[\frac{C_O(0,t)}{C_O^*} \exp\left(\frac{-\alpha nF}{RT}(\eta) \right) - \frac{C_R(0,t)}{C_R^*} \exp\left(\frac{(1-\alpha)nF}{RT}(\eta) \right) \right] \qquad \text{B-3}$$

where C_O^* and C_R^* are the bulk concentrations, and i_0 is the exchange current density can be represent as:

$$i_0 = nFkC_O^{*\,(1-\alpha)}C_R^{*\,\alpha} \qquad \text{B-4}$$

k is the rate constant would expected to show an Arrhenius dependence on temperature.

$$k = k_0(T_{ref})\exp\left[\frac{E_a}{R}\left(\frac{1}{T_{ref}} - \frac{1}{T}\right)\right] \qquad \text{B-5}$$

For an electrode reaction, equilibrium is characterized by the Nernst equation, which links the electrode potential to the bulk concentrations of participants.

$$E^{eq} = E^0 + \frac{RT}{nF}\ln\frac{C_O^*}{C_R^*} \qquad \text{B-6}$$

$$\eta = E^{eq} - E \qquad \text{B-7}$$

Approximate forms of the $i - \eta$ equation

No mass transfer effect.

If the solution is well stirred or currents are kept so low that the surface concentrations do not differ appreciably from the bulk values.

$$i = i_0\left[\exp\left(\frac{-\alpha nF}{RT}(\eta)\right) - \exp\left(\frac{(1-\alpha)nF}{RT}(\eta)\right)\right] \qquad \text{B-8}$$

Tafel behavior at large η

For large values of η, one of the bracketed terms became negligible.

$$\eta = \frac{RT}{\alpha nF}\ln i_0 - \frac{RT}{\alpha nF}\ln i \qquad \text{B-9}$$
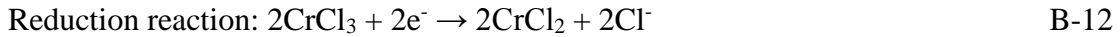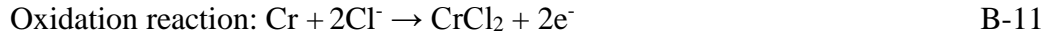
Very facile kinetics

The case in which the electrode kinetics require no driving force at all. The case corresponds to a very large exchange current.

$$E = E^0 + \frac{RT}{nF} \ln \frac{C_O(0, t)}{C_R(0, t)} \tag{B-10}$$

No kinetic parameters are present because the kinetics are so facile that no experimental manifestations can be seen. In effect, the potential and the surface concentrations are always kept in equilibrium with each other by the fast charge transfer processes.

B.2 Calculation of Model Parameters

The oxidation and reduction reactions can be written as B-11 and B-12 respectively, as described by detail in chapter 3.

Oxidation reaction: $Cr + 2Cl^- \rightarrow CrCl_2 + 2e^-$ ⠀⠀⠀⠀⠀⠀⠀⠀⠀⠀⠀⠀ B-11

Reduction reaction: $2CrCl_3 + 2e^- \rightarrow 2CrCl_2 + 2Cl^-$ ⠀⠀⠀⠀⠀⠀ B-12

There were some assumption to calculate the kinetic parameters, are described below:

- Tafel equation is included to explain the polarization near the surface of the alloy.

- The small value of $\frac{\varepsilon^{1.5}}{\delta}$ were used (i.e., $\sim 0.08 \, m^{-1}$) that caused the mass transfer effect at the surface of the coupons were negligible and for the thermosiphon with isothermal conditions, we had the case similar to the case with no mass transfer effect.

As a result, Tafel equations were written as:

$$i_a = i_{0,a} \exp \left[\frac{(1 - \alpha_a) n_a F}{RT} (E_a^{eq} - E_a) \right] \tag{B-13}$$

$$i_c = i_{0,c} \exp\left[\frac{\alpha_c n_c F}{RT}(E_c - E_c^{eq})\right]$$

<div align="right">B-14</div>

The free corrosion condition requires the anodic and cathodic currents to be equal and opposite. The convention that anodic current densities are positive and cathodic current densities are negative has been applied.

$$-i_c = i_a = i_{corr}$$

<div align="right">B-15</div>

The corrosion potential at the metal surface, E, can be found from the current (charge) balance equation at the alloy surface:

$$E_c = E_a = E_{corr}$$

<div align="right">B-16</div>

By the experimental results for three different isothermal conditions of 750, 850 and 950 °C, i_{corr}, E_{corr}, are known. The equilibrium potential were found by equations B-17 and A-18 for given bulk concentrations of Cr^{2+} and Cr^{3+} (i.e., 300 and 1500 ppm respectively).

$$E_a^{eq} = E_a^0 - \frac{RT}{n_a F} \ln(C_{Cr^{2+}})$$

<div align="right">B-17</div>

$$E_c^{eq} = E_c^0 - \frac{RT}{n_c F} \ln(\frac{C_{Cr^{3+}}}{C_{Cr^{2+}}})$$

<div align="right">B-18</div>

Then the exchange current densities could be found by solving equations B-13 and B-14 at different temperatures for $\alpha_a = \alpha_c = 0.5$ [60]. Table B.1 shows the experimental results for i_{corr}, and E_{corr}, in addition to the calculated standard potentials and equilibrium potentials at different temperatures. The exchange current densities results are then shown in Table B.2.

<div align="center">131</div>

Table B.1. Experimental parameters.

T(°C)	i_{corr}(Experiment) (A m^{-2})	E_{corr}(Experiment) (V)	$E^0{}_a$(V)	$E^0{}_c$(V)	$E^{eq}{}_a$(V)	$E^{eq}{}_c$(V)
750	0.34	2.12	2.08	2.85	2.09	2.91
850	0.45	2.26	2.04	2.89	2.06	2.95
950	0.68	2.39	1.99	2.93	2.02	3.00

Table B.2. Calculated exchange current densities.

T(°C)	$i_{0,a}$ (A cm^{-2})	$i_{0,c}$ (A cm^{-2})
750	2.88E-05	4.96E-07
850	2.34E-04	1.59E-06
950	1.47E-03	4.80E-06

Exchange current densities calculated using Equations B-13 and B-14 were plotted against the reciprocal of temperature, as shown in Figure B.1 and B.2. The curves fitted to the data in Figures B.1and B.2 were created with Excel's Trend Line fitting feature and are representative of the Arrhenius relation for reaction kinetics. The resulting expressions allow the calculation of the activation energy of oxidation and reduction reactions.
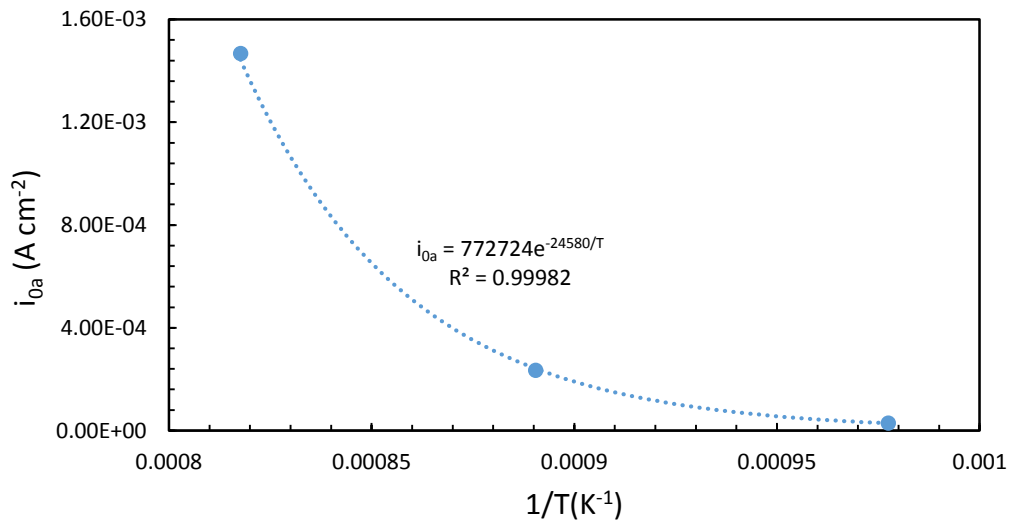

$i_{0a} = 772724e^{-24580/T}$
$R^2 = 0.99982$

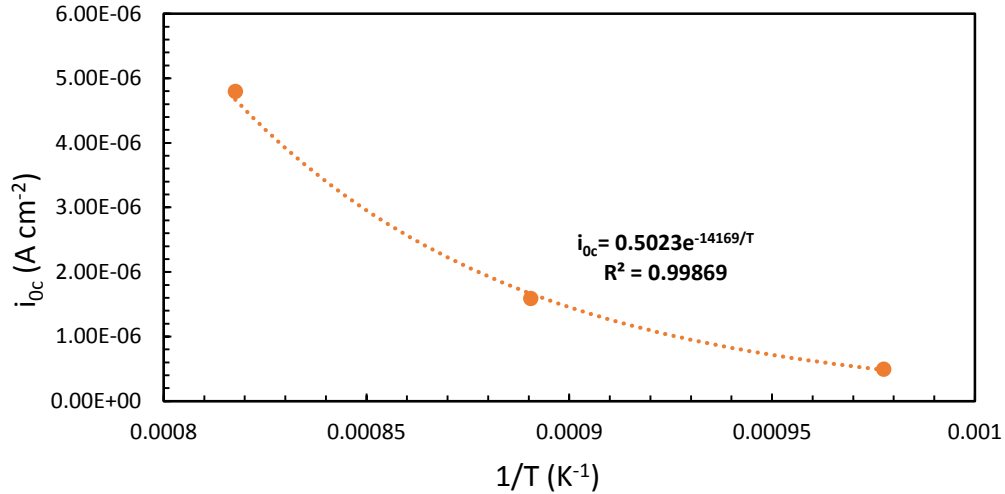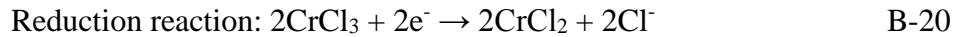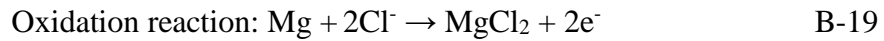Figure. B.1. Anodic exchange current density as a function of temperature.

Figure. B.2. Cathodic exchange current density as a function of temperature.

B.3 Calculation of Parameters for the Mg Reaction:

As mentioned in chapter 4, adding Mg to the salt caused two more reactions:

$$\text{Oxidation reaction: } Mg + 2Cl^- \rightarrow MgCl_2 + 2e^- \qquad \text{B-19}$$

$$\text{Reduction reaction: } 2CrCl_3 + 2e^- \rightarrow 2CrCl_2 + 2Cl^- \qquad \text{B-20}$$

By using the exchange current densities of oxidation, reduction reactions of B-19 and B-20 from previous part and by knowing the experimental data of corrosion potential and corrosion rate under cathodic protection at 850 °C, for Haynes 230, the exchange current density of Mg reaction were calculated.

Assuming the activation energy of Mg reaction is as same as the activation energy of oxidation reaction (B-12), we are able to calculate the pre-exponential factor for Mg reaction. The exchange current density of Mg reaction as a function of temperature is shown in Figure B.3.
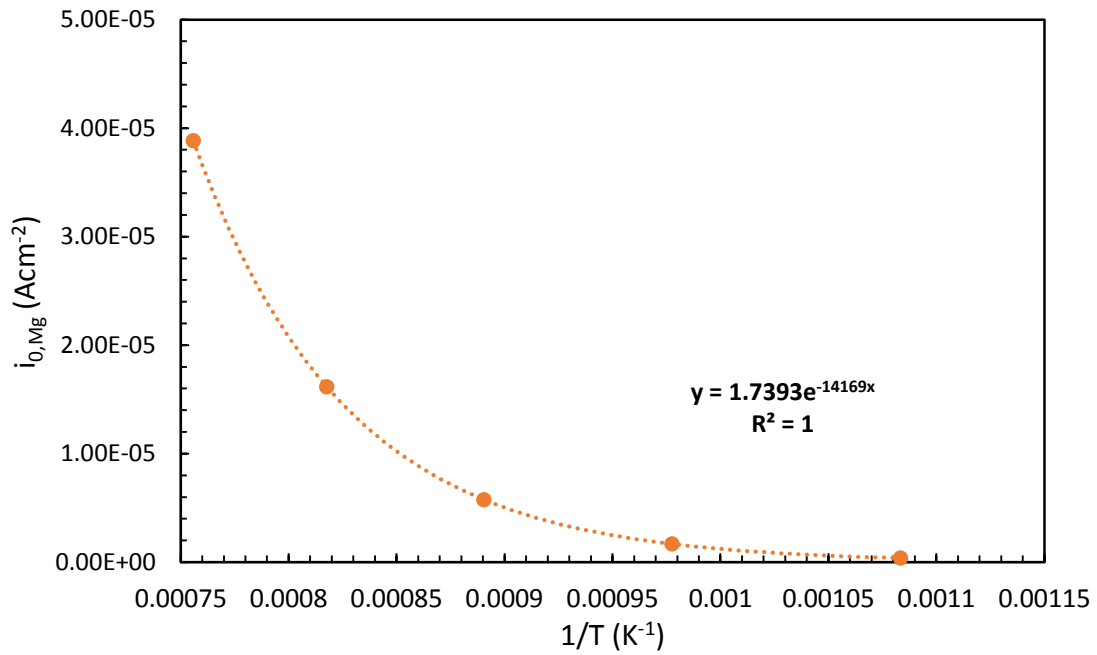
Figure. B.3. Mg exchange current density for Haynes 230 as a function of temperature.

APPENDIX C. NUMERICAL TECHNIQUES

C.1 Solution Procedure

A commercial computational fluid dynamics (CFD) code, STAR-CD, was used as the backbone for the implementation of the model. The STAR-CD system consists of two components (see Figure C.1): the analysis module STAR and the pre- and post-processing module pro-STAR. External links also exist to enable user programming of certain features and to communicate with other computer-aided engineering (CAE) systems for the purposes of, for example, importing grids or performing other kinds of analysis.
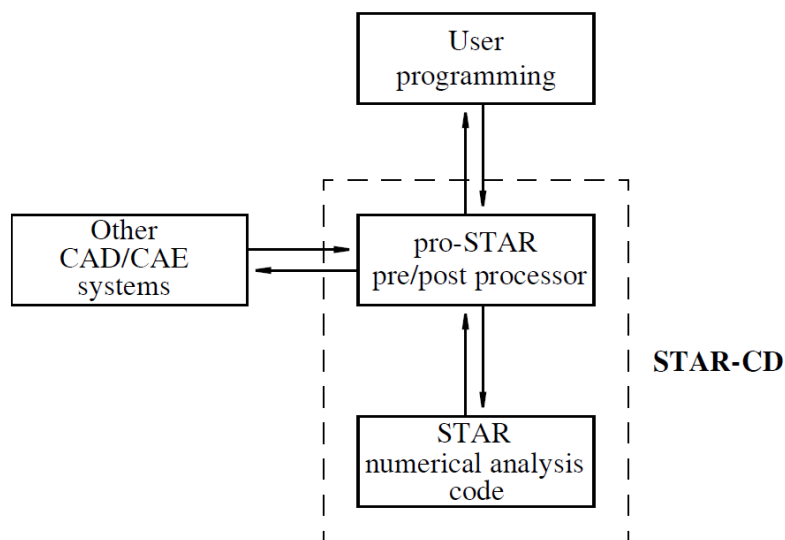

Figure C.1. Overall STAR-CD system structure [129].

The codes solves for the standard thermo-fluid transport equations, and user defined subroutines were developed for the parts of the model specific to the corrosion reactions. The differential equations governing the conservation of mass, momentum, energy, etc. within fluid and solid systems, presented in Table C.1 discretized by the finite volume (FV) method. The equations then can be solved by an iterative SIMPLE algorithm.

The momentum, heat, mass and species conservation equations show in Table C.1. Equation C-5 shows there are some source and sink terms, S_i, which the exact form of these terms depend on the corrosion current (i.e., Equation C-6). User input of such source/sink terms is called for and can be provided via user coding.

Table C.1. Governing equations

Governing equations	Mathematical expressions	
Conservation of Mass	$\dfrac{\partial \rho}{\partial t} + \dfrac{\partial (\rho u)}{\partial x} + \dfrac{\partial (\rho v)}{\partial y} + \dfrac{\partial (\rho w)}{\partial z} = 0$	C-1
Conservation of Momentum	$\dfrac{\partial \rho u}{\partial t} + u\dfrac{\partial (\rho u)}{\partial x} + v\dfrac{\partial (\rho u)}{\partial y} + w\dfrac{\partial (\rho u)}{\partial z}$ $= -\dfrac{\partial P}{\partial x} + \dfrac{\partial}{\partial x}\left(\mu\dfrac{\partial u}{\partial x}\right) + \dfrac{\partial}{\partial y}\left(\mu\dfrac{\partial u}{\partial y}\right) + \dfrac{\partial}{\partial z}\left(\mu\dfrac{\partial u}{\partial z}\right) + S_{Px}$ $\dfrac{\partial \rho v}{\partial t} + u\dfrac{\partial (\rho v)}{\partial x} + v\dfrac{\partial (\rho v)}{\partial y} + w\dfrac{\partial (\rho v)}{\partial z}$ $= -\dfrac{\partial P}{\partial y} + \dfrac{\partial}{\partial x}\left(\mu\dfrac{\partial v}{\partial x}\right) + \dfrac{\partial}{\partial y}\left(\mu\dfrac{\partial v}{\partial y}\right) + \dfrac{\partial}{\partial z}\left(\mu\dfrac{\partial v}{\partial z}\right) + S_{Py}$ $\dfrac{\partial \rho w}{\partial t} + u\dfrac{\partial (\rho w)}{\partial x} + v\dfrac{\partial (\rho w)}{\partial y} + w\dfrac{\partial (\rho w)}{\partial z}$ $= -\dfrac{\partial P}{\partial z} + \dfrac{\partial}{\partial x}\left(\mu\dfrac{\partial w}{\partial x}\right) + \dfrac{\partial}{\partial y}\left(\mu\dfrac{\partial w}{\partial y}\right) + \dfrac{\partial}{\partial z}\left(\mu\dfrac{\partial w}{\partial z}\right)$ $+ S_{Pz}$	C-2
Conservation of Energy	$\dfrac{\partial \rho h}{\partial t} + \dfrac{\partial}{\partial x_j}(\rho h u_j + F_{h,j}) = \dfrac{\partial P}{\partial t} + u_j\dfrac{\partial P}{\partial x_j} + \tau_{ij}\dfrac{\partial u_i}{\partial x_j} + S_h$	C-3
Conduction heat transfer	$\dfrac{\partial (\rho e)}{\partial t} + \dfrac{\partial}{\partial x_j}\left(k_{ji}\dfrac{\partial T}{\partial x_j}\right) + S_e$	C-4
Species transport	$\dfrac{\partial (\rho m_i)}{\partial t} + u\dfrac{\partial (\rho m_i)}{\partial x} + v\dfrac{\partial (\rho m_i)}{\partial y} + w\dfrac{\partial (\rho m_i)}{\partial z}$ $= \dfrac{\partial (J_{x,i})}{\partial x} + \dfrac{\partial (J_{y,i})}{\partial y} + \dfrac{\partial (J_{z,i})}{\partial z} + S_i$	C-5
Species source/sink term at the coupon surface. (i_j is the current density of the jth reaction)	$S_i = -\displaystyle\sum_{j=1}^{r}\dfrac{s_{i,j} i_j}{n_j F}$	C-6

The algorithm developed in this model is unique in the way of predicting cell corrosion current density. The solution begins by guessing a corrosion rate (CR) to use for calculating the species concentrations at the surface of the coupons. Then follows by computing the equilibrium potentials for the anodic and cathodic reactions. Once the equilibrium potentials are obtained, the local current densities are solved based on the Butler-Volmer equation. Convergence criteria are then performed on each variable and the procedure is repeated until convergence. The algorithm of the false position method has been used to find the corrosion rates at the surface of the coupons. The algorithm flowchart is shown in Figure C.2.
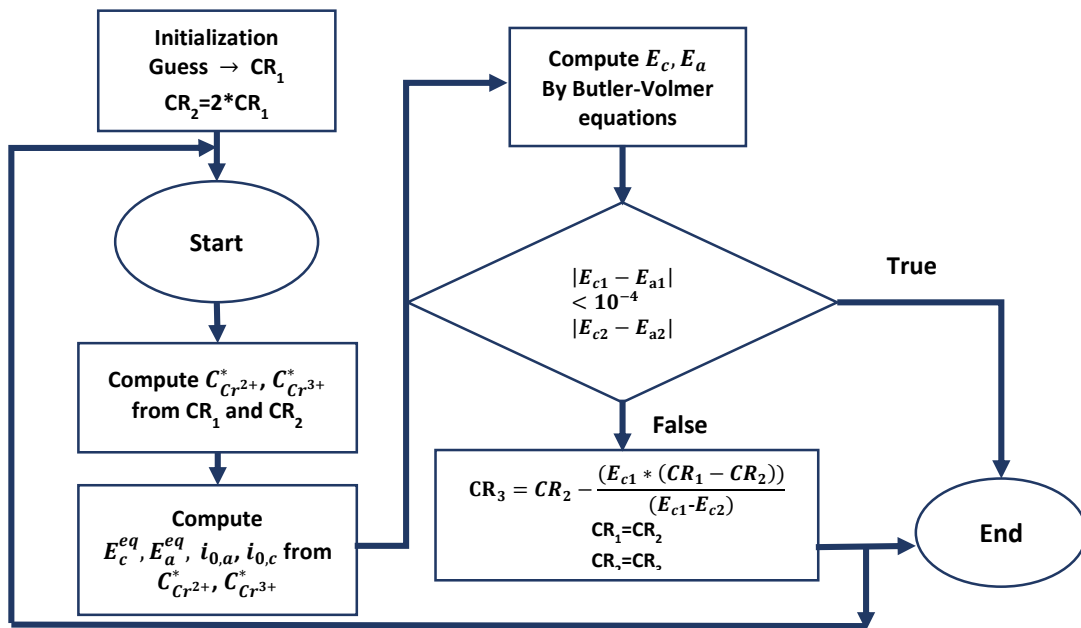

Figure C.2. Algorithm flowchart.